UCLouvain

epl

École polytechnique de Louvain

Design and realization of a magnetic suspension for a high performance flywheel energy storage system

Authors: **Sébastien Bosschaert, François Boulanger**
Supervisor: **Bruno Dehez**
Readers: **Prof. Bruno Dehez, Prof. Emmanuel De Jaeger, Guillaume Colinet**
Academic year 2022–2023
Master [120] in Electro-mechanical Engineering

ABSTRACT

This master's thesis aims at developing an analytical model of a particular topology of active magnetic bearing (AMB). This topology, called slotless homopolar hybrid AMB (SHH-AMB), presents the advantage of mitigating the iron losses. This makes it an interesting candidate for a flywheel energy storage system (FESS) application, that stores energy under a kinetic form.

After a description of the layout and a proof of concept, the global parameters of the SHH-AMB topology are identified as the axial position stiffness k_z, the radial position stiffness k_ϵ, the tilt angle stiffness k_Ψ and the current stiffness k_i. These stiffnesses model the electrodynamic and detent forces acting upon the rotor of the bearing.

From these considerations, a semi-analytical magnetic model is developed based on a Fourier approach also known as the subdomain method, which solves the Maxwell's equations in every subdomain. This model allows to precisely compute the distribution of magnetic flux density when the rotor of the AMB is radially centered. The model is also extended to take a radial eccentricity of the rotor into account thanks to a modulation function. The values of the global parameters are retrieved thanks to these distributions. A comparison with a finite element model (FEM) demonstrates the validity of the model. A mechanical model is also developed to assess the performances of a given bearing by computing the self-discharging time as well as the maximum speed of the rotor.

Based on the magnetic and mechanical model, an optimization routine is set up with a view to the building of a prototype. The objectives being to have a lightweight device with the highest self-discharging time, this optimization uses the geometrical and electromagnetic parameters of the bearing as variables. Constraints are added to ensure the feasibility of the device. These are of different natures: geometry, magnetic saturation in the ferromagnetic materials, axial stability and lift-off criteria, and maximum rotating speed. The output of the optimization consists in a Pareto fronts from which a device is selected based on an analysis of the parameters of the machines.

A design of a prototype built on the basis of the optimization is proposed. The objective of the prototype is to validate the magnetic model by comparing the actual global parameters of the prototype with those predicted by the model. However, difficulties to lift off the rotor have been encountered, making the experimental evaluation of some of the characteristics of the bearing impossible. As it does not require the levitation of the rotor, the value of the axial stiffness is experimentally evaluated and corresponds to the one predicted by the model.

ACKNOWLEDGMENTS

As this part symbolizes for us the last written section of this master's thesis, we would like to thank all those who have helped us in the realization of this project.

First of all, we wish to acknowledge the support and guidance provided by our supervisor, Prof. Bruno Dehez, who accompanied us on this journey. Throughout the numerous meetings that he has granted us, he has always provided us with pertinent remarks and advice that drove us forward. We would also thank him for the opportunity that he gaves us to write a conference paper.

We would also like to deeply thank Guillaume Colinet, who followed us this whole year and who actively helped us in the realization of the magnetic model and of the control part of the prototype and was always available to answer our questions.

We are also grateful to Thierry Daras for the time and the energy spent debugging the prototype and for is availibility to provide us with elecronic materials.

We would also show our gratitude to the members of the CREDEM platform, especially Dr. Benoît Herman for the help in the mechanical design of the prototype, Simon de Jaeger for the 3D-printing of our parts and for the useful advices, and Vincent Musette, who was always incline to rectify quickly and accurately the manufactured parts of our prototype. Thank you to Dr. Virginie Kluysken for the help in the realizazation of the aerodynamic model. We are also indebted to Christophe de Gréef and Dr. Joachim Van Verdeghem for the advice in the realization of the windings of the prototype and for the time spent trying to make the prototype work. Finally, thank you to Prof. Emmanuel de Jaeger, who agreed to be a member of the jury.

CONTENTS

LIST OF SYMBOLS

α	Ratio of the dimensions of the bearing used as optimization variables	$(-)$
Γ	Modulation function	$(-)$
Δ_ϵ	Distance between the geometrical center and the mass center of the rotor	(m)
Δ_{Ψ_i}	Tilt angle of the rotor along axis i	(rad)
Δ_i	Deviation of the rotor position from the centered one with respect to axis i	(m)
Δ_k	Axial distance separating the main coordiante frame and the one of region k	(m)
$\Delta_{z,eq}$	Equilibrium axial position of the rotor	(m)
ϵ	Radial eccentricity of the rotor with respect to the stator center	(m)
ϵ_s, ϵ_c	Correlation function	$(-)$
ζ_s, ζ_c	Correlation function	$(-)$
η	Fill factor of the windings	$(-)$
$\Theta_{W,e}$	Outer opening angle of the windings	(rad)
$\Theta_{W,i}$	Inner opening angle of the windings	(rad)
κ_s, κ_c	Correlation function	$(-)$
μ_0	Magnetic permeability of the vacuum	(H/m)
μ_{air}	Dynamic viscosity of the air	(Ns/m^2)
μ_k	Relative magnetic permeability of region k	$(-)$
$\mu_{r,PM}$	Relative magnetic permeability of the permanent magnets	$(-)$
ν	Poisson coefficient of the steel of the rotor	$(-)$
ν_{air}	Kinematic viscosity of the air	(m^2/s)
τ_k	Period of region k	(m)
τ_{wall}	Mechanical shear stress originating from a flow on a wall	(N/m^2)
ρ	Density of the steel of the rotor	(kg/m^3)
ρ_{Cu}	Electrical resistivity of the copper	(Ωm)
ρ_{air}	Density of the air	(kg/m^3)
$\mathfrak{T}$	Maxwell stress tensor	(N/m^2)
σ	Mechanical stress	(N/m^2)
σ_{VM}	Von Mises equivalent stress	(N/m^2)
σ_y	Yield stress of the steel of the rotor	$()$
ϕ, Φ	Magnetic flux	(Wb)
Ψ	Tilt angle of the rotor	(rad)
ω_k	Pulsation of region k	(rad/m)
Ω	Rotational speed of the rotor	(rad/s)
Ω_0	Operating speed of the rotor	$()$
Ω_{max}	Maximal rotational speed of the rotor	(rad/s)
$\vec{A}$	Magnetic potential vector	(Tm)
$\vec{B}$	Magnetic flux density vector	(T)
B_i	Component along axis i of the magnetic flux density vector	$()$
B_{rem}	Remanent flux density	(T)
c_f	Skin friction coefficients	$(-)$
E_k	Kinetic energy of rotation of the rotor	(J)
E_0	Initial energy stored in the flywheel	(J)
F_i	Radial detent force acting on the rotor along direction i	(N)
$F_{i,i}$	Radial electrodynamic force acting on the rotor along direction i	(N)
$F_{i,mag}$	Resulting electromagnetic force acting on the rotor along the i axis	(N)
g	Gravitational constant	(m/s^2)
G	Balance grade of the rotor	$(radm/s)$
$\vec{H}$	Magnetic strength vector	(A/m)
H_i	Component along axis i of the magnetic strength vector	(A/m)
i_b	Bias current	(A)
i_c	Control current with no specific direction	(A)

i_i	Control current of axis i	(A)
I_i	Moment of inertia of the rotor with respect to axis i	(kgm^2)
$I_\nu(x)$	Modified Bessel function of the first kind of order ν	$(-)$
$\vec{J}$	Current density vector	(A/m^2)
k_ϵ	Radial position stiffness	(N/m)
k_Ψ	Tilt angle stiffness	(Nm/rad)
$k_{\Psi,z}$	Axial forces contribution to the tilt stiffness	(Nm/rad)
$k_{\Psi,r}$	Radial forces contribution to the tilt stiffness	(Nm/rad)
k_i	Current stiffness	(N/A)
k_s	Safety coefficient	$(-)$
k_z	Axial position stiffness	(N/m)
K_D	Derivative gain of the PID controller	$(-)$
K_I	Integral gain of the PID controller	$(-)$
K_P	Proportional gain of the PID controller	$(-)$
$K_\nu(x)$	Modified Bessel function of the second kind of order ν	$(-)$
$L_{B,R}$	Axial distance bewteen the two rotor iron teeth	(m)
L_{ext}	Half of the distance separating two occurrances of the subdomain model	(m)
$L_{I,R}$	Axial length of the rotor iron teeth	(m)
$L_{I,S}$	Axial length of the stator iron teeth	(m)
L_{PM}	Axial length of the permanent magnet ring	(m)
$L_{W,e}$	Outer length of the end windings	(m)
$L_{W,i}$	Inner length of the end windings	(m)
m_{rotor}	Mass of the rotor	(kg)
$\vec{M}_0$	Magnetization vector	(A/m)
M_i	Component along axis i of the magnetization vector	$()$
n	Number of harmonics	$(-)$
N_W	Number of turns in the coils constituing the windings	$(-)$
P_{ag}	Air gap permeance	(Wb/A)
P_{Aero}	Aerodynamic losses occuring on the rotor	(W)
P_{Joule}	Joule losses occuring in the windings of the bearing	(W)
PM_{FF}	Permanent magnet fill factor	$(-)$
R	Electrical resistance of one phase of winding	(Ω)
R_0	Scaling radius	(m)
R_{ag}	Air gap reluctance	(A/Wb)
R_e	Reynold number	$(-)$
R_{MST}	Radius of the cylinder used for the Maxwell's stress tensor	(m)
$R_{PM,i}$	Inner radius of the permanent magnet ring	(m)
$R_{R,d}$	Radius of the inner hole in the rotor	(m)
$R_{R,e}$	Outer radius of the rotor	(m)
$R_{R,i}$	Inner radius of the rotor	(m)
$R_{S,e}$	Outer radius of the stator	(m)
$R_{S,i}$	Inner radius of the stator	(m)
$R_{W,i}$	Inner radius of the windings	(m)
S_W	Cross-sectional area of one coil of the bearing	(m^2)
S_c	Cross-sectional area of the conductors of the windings	(m^2)
$T_{\Psi_i,mag}$	Resulting electromagnetic torque acting on the rotor along axis i	(Nm)
W_{cmag}	Co-magnetic energy	(J)
(r,θ,z)	Cylindrical coordinate frame attached to the center of the stator	$((m,rad,m))$
(r,z_k)	Local cylindrical coordinate frame attached to region k	$((m,m))$
(x,y,z)	Cartesian coordinate frame	$((m,m,m))$

INTRODUCTION

In the last decades, the use of renewable energy sources has grown significantly, causing a need for energy storage systems. These sources being driven by the natural variations, such as the wind, the water flows or the temperature, the power production is not always in phase with the demand. To be able to take advantage of renewables engineers resources have been invested toward the development of energy storage technologies. Among those systems, the flywheel energy storage systems (FESSs) store energy by converting it into a kinetic form and back to an electrical according to the power demand. The main advantages of FESSs are their long lifespan, and low environmental impact. They can also withstand a lot of charge/discharge cycles and can operate continuously. However, FESSs offer a poor storage duration compared to other energy storage systems due to their high self-discharging rates.

The high self-discharging rate of FESS is due to several types of losses, intrinsic to its constitutive elements, occurring even if the system is in standby. The traditional topology of flywheel consists in a high inertia body, the rotor, fixed on a shaft, guided by a rolling bearing and actuated in rotation by an electromechanical converter. The efficiency of this kind of flywheel is limited by several main losses. Among these losses, are found the aerodynamic friction at the rotor surface and inside the converter air gap. These losses are generally mitigated by working in a vacuum chamber. Another source of loss is the friction inside the rolling bearing, that is mitigated by replacing the classical roller bearings by active magnetic bearings (AMBs). AMB allows for a contactless guidance of the rotor, which removes the mechanical wear and the dry friction. The use of AMB introduces two other sources of losses: the Joule and iron losses, induced by the current flowing through the windings of the bearing and the varying magnetic flux density within the ferromagnetic parts, respectively.

To improve the efficiency of AMB, Joule and iron losses are mitigated by employing different types of AMB. Some of them tend to be more suitable for FESS. Hybrid-AMB (H-AMB) is a particular topology of AMB that uses permanent magnets instead of windings supplied in DC to generate the polarizing magnetic flux density, which allows getting rid of a part of the Joule losses. The paper [1] explains how such a bearing can be obtained by modifying a classical radial AMB. The remaining significant losses occurring in the H-AMB topology are iron losses due to the varying magnetic flux density inside the rotor in rotation. The classical heteropolar AMB cause a switching of polarity of the polarizing magnetic flux density in the rotor depending on its angular position. These iron losses are mitigated by using a homopolar hybrid-AMB (HH-AMB) as explained in [2]. This particular topology provides a magnetic field with a constant polarity in each iron tooth of the rotor. Small fluctuations in the magnetic field density inside the rotor remain and still give rise to iron losses. These fluctuations come from the slots in which the windings are inserted. Removing these latter would make the ferromagnetic parts axisymmetrical and so would be the polarizing magnetic field that would not vary within the rotor, even in rotation. Such a configuration is met in slotless homopolar hybrid-AMB (SHH-AMB) that theoretically removes the iron losses by employing air gap windings, as explained in [3].

In this thesis, a specific topology of SHH-AMB with an additional axial stabilization of the rotor is considered similarly as in [4]. This stabilization is obtained thanks to additional iron teeth on the rotor that maintain it in a centered position by applying a detent force opposed to its axial displacement. The first objective of this work is to develop a local magnetic model of such a topology to characterize it globally, similarly to what is achieved in [5]. This bearing is designed such as it can be used as a FESS. A model, characterizing the performances of this system, is developed to employ it in an optimization routine that determines the best dimensions to give to the prototype that is finally built.

This document is divided into six chapters. In chapter 1, the state-of-the-art of FESS and AMB is reviewed. The chapter 2 provides a description of the layout and the working principle of the topology. The magnetic model of the bearing is developed and validated in chapter 3. The chapter 4 consists in the modeling of the flywheel with a view to an optimization, performed in chapter 5. The results of this optimization step are finally exploited in the building of a prototype and its characterization, explained in chapter 6.

CHAPTER 1

STATE OF THE ART

This chapter presents a review of the literature about the historical and technological aspect of flywheel energy storage systems and active magnetic bearings that are frequently employed in these systems. The Flywheels are presented in section 1.1 and the magnetic in 1.2.

1.1 Flywheel Energy Storage Systems

Flywheel Energy Storage Systems (FESS) stores energy in its kinetic form thanks to a rotating wheel, known as a rotor, consisting of a heavy mass rotating at high speed. The energy is exchanged from kinetic to electrical and vice versa by braking or accelerating the rotor. The origin of the word "flywheel" goes back to the industrial revolution, when flywheels were used in factories to accumulate energy, and in steam engine boats and trains [6]. In the last decades, FESS gained significant attention as a potential solution to store the energy for a long period to deal with the mismatch between the consumption and the production. They also present a flexible architecture that can be adapted to optimize the performances to the context it is used.

1.1.1 FESS among other energy storage systems

Fig. 1.1 illustrates the five main categories of energy storage systems in which the different technologies are classified. The mechanical storage, which includes FESS but also pumped hydroelectric energy storage system and compressed air storage system, stores energy in a mechanical form. Energy is stored electrochemically in classical batteries such as Lithium-ion. Electrical storage is another solution and uses either capacitors, super-capacitors or superconducting magnets. The energy is stored chemically using hydrogen, synthetic natural gas, thermochemical reversible reactions and biofuels in some systems. The energy can also be stored in a thermal form using different technologies: sensible heat storage, latent heat storage, absorption and adsorption storage.

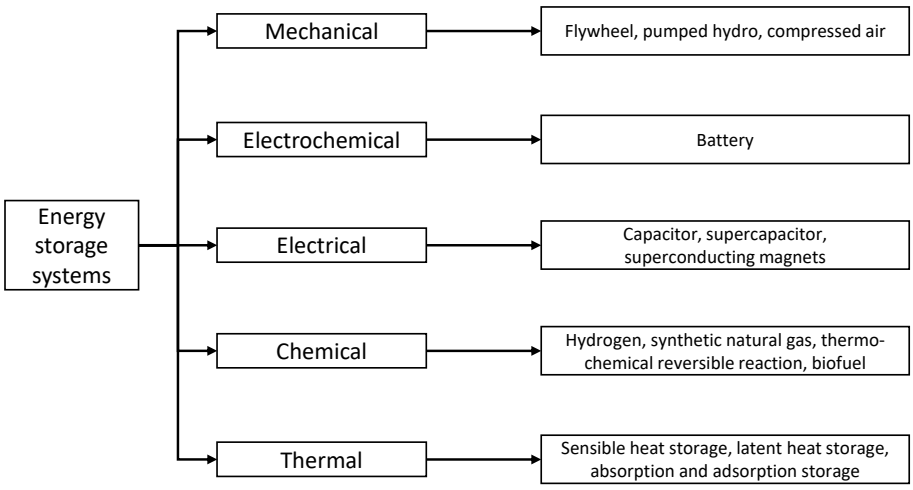

Figure 1.1: Energy storage systems [7, 8, 9].

1.1.2 Main advantages of FESS

The technologies previously mentioned come with advantages and drawbacks which make them more appropriate for some applications than others. The performances of each technology are assessed with different characteristics, the main ones being the power density, power quality (response time and voltage stability), the efficiency, the lifespan, and the cycle life [8][10]. Other metrics are important to take into account when searching for an energy storage system, such as: the cost, the environmental impact, the power rating and the storage duration. Among the technologies of energy storage, FESS distinguishes from others thanks to several characteristics.

As studied in [8], FESS typically provide a lifespan between 15 and 20 years depending on the topology. This lifespan comes with a low need for maintenance [11]. As a comparison point, typical chemical Lithium-ion batteries perform between 2 and 20 years [8]. The technology with the longest lifespan studied in [8] is the Nickel Iron battery, with 100 years.

The cycle life of FESS reaches up to 100000 cycles, which is globally higher than other systems in [8]. Only electrical energy storage systems like superconducting magnets and super-capacitors with 100000 and 1000000 cycles, respectively can compete. Unlike electrochemical batteries, the cycle life of FESS is also independent of the depth of discharge of the cycles.

FESS also distinguish from others regarding the power density with performances up to 2000 kW/m^3 [8]. Only electrical storage technologies can realize better performances with 4000 kW/m^3 for the superconducting magnets and 4500 kW/m^3 for the super-capacitors. For typical Lithium-ion batteries, the power density reaches 800 kW/m^3.

Efficiency is obviously an important characteristic of energy storage systems. Flywheels offer an efficiency ranging from 70% to 96%, with an average of about 89% which makes it the most efficient mechanical energy storage system [8]. These figures can be compared to Lithium-ion batteries performances, which reach efficiencies between 70% and 100% with an average of 90% [8].

Regarding the power quality, FESS allows response times of less than 4 ms, which is by far better than other mechanical energy storage systems and in the range of electrochemical technologies [12]. This feature of FESS makes it an appropriate system to enhance power quality problems such as voltage sag, over/under voltage, supply interruptions, transients, and frequency deviation.

In terms of environmental impact, FESS induces relatively low manufacturing impacts, not significant operational impact and relatively low disposal impact [13, 9]. FESS do not require the management and the disposal of any chemical substance required in chemical and electrochemical systems [14], but only raw materials for the manufacturing, which are metals or composites. These raw materials can be partially recycled at disposal.

These advantages come with three main drawbacks [15, 8, 7]. FESS usually comes up with an energy density lower than 430 kWh/m^3, which is relatively poor compared to other technologies like certain chemical batteries that can perform two to three times better [8]. High self-discharge rate due to standby losses is also an important drawback of flywheel systems, preventing them to be used in long-term applications. The potential failure modes that are also dangerous. As FESS employs mechanical parts rotating at high speed, if a failure occurs (due to wear, problem in the controller, power electronics, failure in the bearings), the mechanical energy of the rotor is released suddenly and leads to significant damage.

1.1.3 Applications of flywheel energy storage systems

In the last decades, FESS have emerged as a promising alternative to electrochemical batteries to store energy in a wide range of applications [16]. Depending on the domain of application, the requirements in terms of power capacity and discharge time change, but the technology remains the same [10].

One of the most discussed applications nowadays concerns the renewable energy integration, i.e., the use of FESS to store the energy produced by renewable energy sources, typically solar and wind energy. FESS can be a solution to the mismatch between the production and the consumption of the energy that these renewable sources introduce with their intermittent nature. By making use of their fast response time, FESS can also improve the power quality that is output by the renewables via an appropriate control strategy[16]. They are also used to increase the energy penetration in power grids [17].

At a residential level, FESS can be used for domestic electrical installations. It can help power suppliers to store the excess of energy produced by renewable energy sources, as previously discussed [11]. FESS can also provide an on-demand releasing capability, enabling power suppliers to deliver electricity during peak hours or periods of high demand [18]. By harnessing the stored kinetic energy, these systems can quickly release power, helping to stabilize the grid and ensure a reliable supply of electricity. It can also be used for power peak shaving by smoothing out fluctuations in power demand by supplementing the grid during times of peak usage [18]. This allows to reduce the strain on the grid and lower the electricity costs for the consumers. Additionally, a FESS in a home can serve as an effective power backup solution in case of power outage or disruption, allowing essential appliances and devices to continue operating [18]. This feature can be interesting for regions with unreliable power infrastructures, as it allows an uninterruptible power supply.

In aerospace, FESS are used to compensate for the period when low earth orbit devices can not produce electricity from solar energy. Indeed, as stated before, the overproduction can be stored to power onboard systems when the devices lie in an eclipse period [19]. FESS are preferred in this context than electrochemical batteries [11] since FESS are less heavy for equivalent capacity, which reduces production costs as the total weight is a major concern in aerospace. Moreover, they offer a longer lifecycle that can go up to 100000 cycles as explained before, which is higher than the best Lithium-ion batteries that can only reach 10000 cycles [20].

In the automotive field, FESS are used to smartly reused the energy doomed to be lost. The main goal being to recover energy to reduce fuel consumption, the FESS design depends on the kind of vehicle. For public transport buses or garbage trucks that start and stop frequently, energy can be recovered from braking and can be used either to power on board systems or to power when starting [21]. The same approach of regenerative braking energy is used for railway vehicles to improve their efficiency, to reduce the peak power, but also allowing the vehicles to travel through areas without overhead line provision or without power supply [22]. Regarding cars and their environmental impact, development has been put on the hybridization [21]. Some systems have been experimented in motorsport, like the Kinetic Energy Recovery System (KERS), first introduced in Formula 1 in 2009 [23]. KERS is used to convert the kinetic energy that is normally lost into heat during braking, and can then provide an extra boost of power to the car when accelerating or overtaking. However, the use of FESS in motorsport has different specifications than for road cars. Indeed, since the driving is totally different on the road, the motorsport systems are not adapted to every car. That is why car companies, like Jaguar and Volvo, have been investigating the use of flywheel systems for their road cars in the last years [21]. They managed to save around 20% of fuel using such systems.

Among the other applications, FESS can be found in charging stations to ensure the supply of electric vehicles when power cannot be extracted from the grid [24]. FESS can also be used for frequency regulations to compensate for the fact that the grid load is not constant [10]. There are other fields of applications such as the marine, the defense, and the industries for which FESS can be used.

1.1.4 Constitutive elements

A FESS is composed of five main elements that ensure its functioning: the rotor, the motor/generator, the guiding elements, the power electronics and the enclosure. These components are represented in fig. 1.2. Indeed, the FESS manufacturers propose different topologies as shown in table 1.1, but they are all made of these five components.

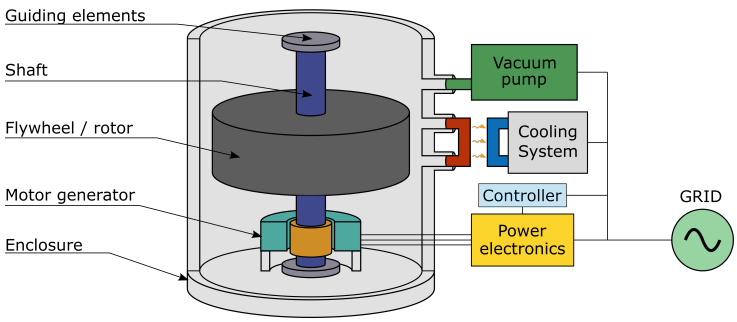

Figure 1.2: Constitutive elements of FESS.

Table 1.1: Different manufacturers of FESS and their topology [25].

Manufacturer	Piller Power Bridge Temporal Power Rosseta T2 Vycon Gyrotricity Amber Kinetics	Active Power	Beacon Power Gen 4 Kinetic Traction Systems Stornetic Power Thru
Topology	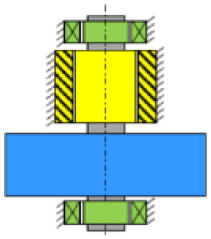	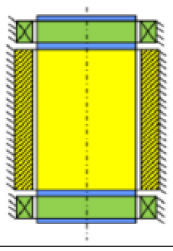	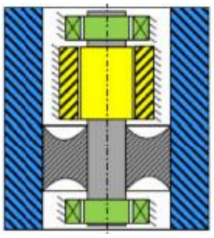

The rotor

The rotor, also called the flywheel, is the rotating part of the system that stores the energy. More specifically, it consists of a high inertia body that accumulates kinetic energy with its rotation. It is mounted on a shaft and supported by guiding elements to minimize the friction and allow a smooth rotation. The critical aspect of this element is its geometry and the material in which it is made [6, 26]. Both these parameters impact the moment of inertia I which determines the kinetic energy E that can be stored at a given rotational speed Ω [6]:

$$E_k = \frac{1}{2} I_z \Omega^2 \tag{1.1}$$

Regarding the geometry, it is generally a hollow cylinder of mass m_{rotor} whose height h, inner radius a and outer radius b influences the moment of inertia as follows [6]:

$$I_z = \frac{1}{2} m_{rotor}(b^2 - a^2) = \frac{1}{2}\pi\rho h(b^4 - a^4) \tag{1.2}$$

where the mass m depends on the mass density ρ the height, the outer and the inner radii.

The material also determines the maximum speed the rotor can reach before failure [6, 26]. The material is subject to mechanical stress appearing with the rotation and the centrifugal effect. Characteristics such as the density, the yield stress, the Poisson coefficient and the Young's modulus are key elements in the design of the rotor [27, 28]. The mechanical design of the rotor is explained in chapter 4.

The required speed, available space and budget imposed by the application allow determining the geometry, the dimensions, and the material of the rotor as well as the bearing type and the electrical machine [11]. Two categories of FESS are distinguished regarding the operational speed. If this latter is below 10000 rpm, the flywheel operates at "low speed" and at "high speed" otherwise [11, 18]. These categories influence the technology employed in the system.

Speed limit being related to the choice of material, several materials with different stress limitations are considered. In general, composite-based rotors offer superior performance in terms of speed, rotational stress tolerance and energy density compared to their steel-based counterparts [29, 26]. That is why, composite materials with lower mass densities are used for high-speed FESS while isotropic materials are commonly used for low-speed ones. Some common materials used for rotors are detailed in table 1.2.

The motor-generator

The motor component of a FESS enables a bidirectional conversion process between electrical and mechanical energy. When excess electrical energy is available in the system, the converter acts as a motor and converts electrical energy into mechanical energy by accelerating the rotation rotor. Conversely, a demand for electrical power is fulfilled by slowing down the rotor with the converter, which is used as a generator.

Table 1.2: Materials used for rotors in FESS [30].

Material	**Density [g/cm^3]**	**Maximum tensile strength (azimuthal for composites) [MPa]**	**Cost [€/kg]**
Aluminum (isotropic)	2.7	500	2.8 (Al-6061-T6)
Steel (isotropic)	7.8	800	0.56 (AISI 4340)
E-Glass epoxy (composite)	2	1000	4.43
High strength graphite (composite)	1.6	1500	18.62

Because of the typically high speeds associated with flywheels, the use of brushes is avoided, which means that neither DC machines nor wound rotor synchronous machines are employed [21]. The selection of an energy conversion system for a FESS depends on various factors such as power requirements, rotational speed, efficiency, control, cost, and the specific application context. Several types of technologies are used [10, 11]:

- Permanent magnet synchronous machine (PMSM): it is a popular choice as it offers high power density and high efficiency. This kind of machine is expensive, implies idling losses, uses permanent magnets that are prone to demagnetization and has a narrow optimum range of temperature. Similar machines to PMSM are also used in FESS such as the brushless direct current machine (BLDC) and the axial flux permanent magnet (AFPM) [29].
- Induction machine (IM): it provides less power density and less efficiency than PMSM, but it is still widely used for FESS since it is simple, reliable, and relatively inexpensive.
- Switched reluctance machine (SRM) and Synchronous reluctance machine (SyRM): it is simple, reliable, more efficient than IM at high speeds and not subject to demagnetization since it is free of permanent magnet. The drawbacks are the maturity of the technology and controllability.
- Synchronous homopolar machine (SHM): it induces low idle losses and its robust structure allows for high speed and high efficiency FESS [31].
- Bearingless machine (BM): this kind of machine is of interest for FESS since it can both act as a motor-generator and as a magnetic bearing for guiding. The difficulty of implementation of this rather expensive machine lies in the complexity and the controllability.
- Magnetic gear (MG): this technology can be the direct link between the flywheel and the external load. It is simple, robust and does not require power electronics. However, MG provides less power density than others and that the technology is not mature.

The power electronics

The power electronics unit manages the conversion and the control of electrical energy between the FESS, the load, and the grid by allowing a bidirectional power flow. Its components and circuits are used to enable efficient energy transfers, ensure stable operations and provide control capabilities. There exist several layouts of power electronics converter, but the most common is the AC-DC-AC, also known as back-to-back [11]. This layout consists of two voltage source controllers that switch between rectifier and inverter to allow charge and discharge modes [10]. Their current capacity determines the power rating of the FESS. Other layouts of power electronics are possible, such as AC-AC, AC-AC matrix (without system capacitor), DC-AC and DC-DC since some applications may require a DC link to provide an uninterruptible power supply [11].

The guiding elements

These guiding elements support the rotor and allow it to rotate smoothly with minimum losses. Three types of bearings can be used depending on the specific requirements of the FESS design: mechanical, magnetic and hybrid.

- Mechanical bearings such as ball bearings or roller bearings are a cheap alternative but induce wear, mechanical friction losses due to the contact with the rotor and need to be lubricated [30].
- Magnetic bearings (see section 1.2) offer advantages like no mechanical friction, high speed capability, and the ability to operate contactless but are complex [10].

- Hybrid bearings are either composed of a mechanical and a magnetic bearing or of two topologies of magnetic bearing (passive and active, developed in section 1.2). They imply fewer losses than mechanical bearings alone and lower cost than magnetic bearings, but are also complex [10].

The containment

The containment refers to the protective housing or casing that surrounds the flywheel and associated components in a FESS. This component has to ensure both the efficiency and the security. Indeed, to reduce the aerodynamic losses from the rotational motion of the flywheel, the pressure in the enclosure can be decreased to reach a partial vacuum with a vacuum pump [30]. It is also possible to fill the enclosure with a gas having a lower density than air, like Helium, to improve the performances of the FESS [30]. In terms of safety, the containment must keep the hazardous parts when the rotor fails [11]. The containment can also help to reduce vibrations and noise and can incorporate cooling mechanisms for thermal management.

1.2 Magnetic bearings

The appearance of magnetic bearing has opened the way to new FESS topologies allowing the flywheel rotor to levitate and spin at high speeds without physical contact with the housing. Compared to standard bearings, it requires less maintenance and no lubrication [32]. The increased use of magnetic bearings in flywheel was driven by developments in power electronics, materials technology, magnetic bearing technologies and electrical machines [16]. Advancements in power electronics have enabled the use of high-frequency switching to control the magnetic bearings, resulting in improved stability and reliability of the system [6, 33]. The use of advanced materials, such as high-temperature superconductors, also contributed to the development of more efficient and compact magnetic bearings [34]. The magnetic bearing employed in this thesis is a particular topology, allowing to reduce drastically the iron losses occurring within the ferromagnetic materials. This section explains how this topology is obtained starting from the classical AMB. The SHH-AMB does not present slots in which the windings could be inserted and uses air gap windings instead. The manufacturing method employed to implement such windings are presented in this section. Finally, the control strategies adopted for hybrid active magnetic bearings are presented.

1.2.1 Topologies of AMB

This section explains how and why the SHH-AMB topology is obtained from the classical AMB by describing each intermediate topologies and by explaining their advantages and problems.

Active Magnetic Bearings (AMB)

Active magnetic bearings, allow a stable magnetic levitation of its rotor by applying forces resulting from the interaction of the magnetic flux density with windings and ferromagnetic parts. Unlike passive magnetic bearings, AMB require a controller, implying the measure of the position of the rotor and external sources of current. Fig. 1.3, inspired by [35], represents a classical active magnetic bearing. Such bearings require a bias magnetic field that is generally generated by applying a DC bias current i_b in the windings, added to the control currents, i_c. In that way, no permanent magnets are used in the bearing, which helps lower the cost and the complexity of manufacturing. The bias current gives rise to Joule losses through the windings electrical resistance given by Ri_b^2 which tends to reduce the efficiency of such bearings.

Hybrid - Active Magnetic Bearings (H-AMB)

In hybrid-active magnetic bearings [1], the bias magnetic field is generated by permanent magnets which removes the Joule losses associated with the bias current. A H-AMB is illustrated in fig. 1.4. The permanent magnets (PM) are placed in the stator which simplifies the manufacturing of such bearings and improves the robustness, as the PM are the most fragile part of the bearing.

Although the losses occurring within the bearing are reduced with the use of PM, the iron losses, appearing with the rotation of the rotor, remain significant because of the heteropolar nature of the bias magnetic field. As illustrated in fig. 1.5, the magnetic field switches its polarity at each pole, which gives rise to a varying magnetic field within the rotor and to important iron losses if high speeds are reached.

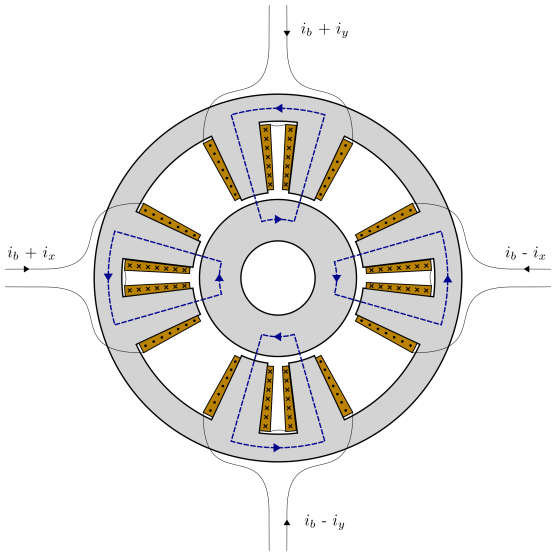

Figure 1.3: 8-pole radial active magnetic bearing.

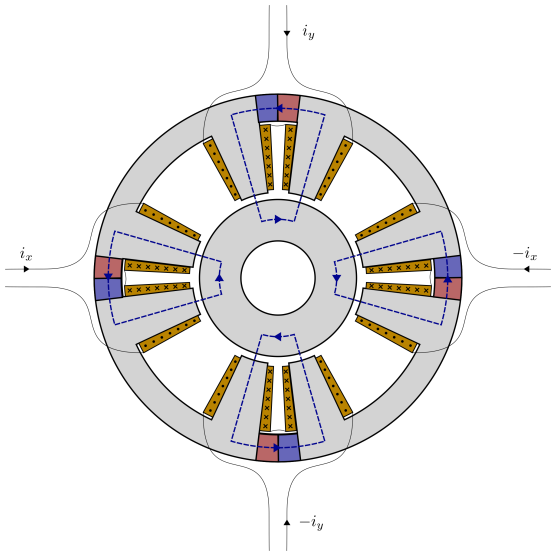

Figure 1.4: 8-pole radial hybrid active magnetic bearing.

Homopolar Hybrid - Active Magnetic Bearings (HH-AMB)

Homopolar hybrid-active magnetic bearings remove the switch of polarity by imposing only one pole in the rotor [2]. As magnetic monopole are not achievable, the pole is duplicated and placed next to the first pole with the opposite polarity. The two poles are linked by an axial circulation of the magnetic flux density in the rotor and in the stator (fig. 1.6).

HH-AMB drastically removes the iron losses occurring within the rotor, even at high speed, as the polarity of the bias magnetic field does not switch with the position of the rotor (fig. 1.7). The iron losses are not completely removed because of the presence of the slots in which the windings are placed which results in asymmetry in the magnetic flux density, whose amplitude still varies with the position of the rotor. This bearing tends to occupy more space axially than classical radial bearings because of the duplication of the pole and the presence of permanent magnets between the poles.

Slotless Homopolar Hybrid - Active Magnetic Bearings (SHH-AMB)

Slotless homopolar hybrid-active magnetic bearings combine the advantages of the HH-AMB and removes the remaining iron losses, due to the varying amplitude of the bias magnetic field, by employing air gap windings instead of slots [3] (fig. 1.8 and 1.9).

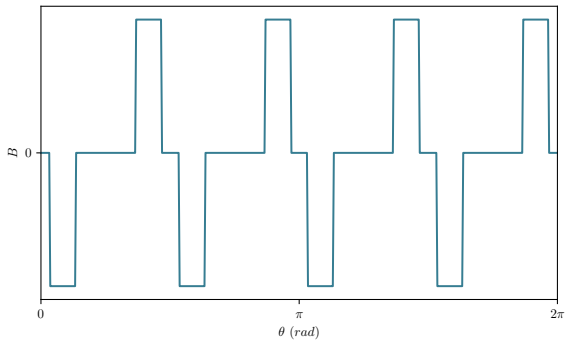

Figure 1.5: Illustration of the air gap radial magnetic field in a radial hybrid 8-pole active magnetic bearing as a function of the azimuthal position θ. The polarity of the magnetic flux density switches at each pole.

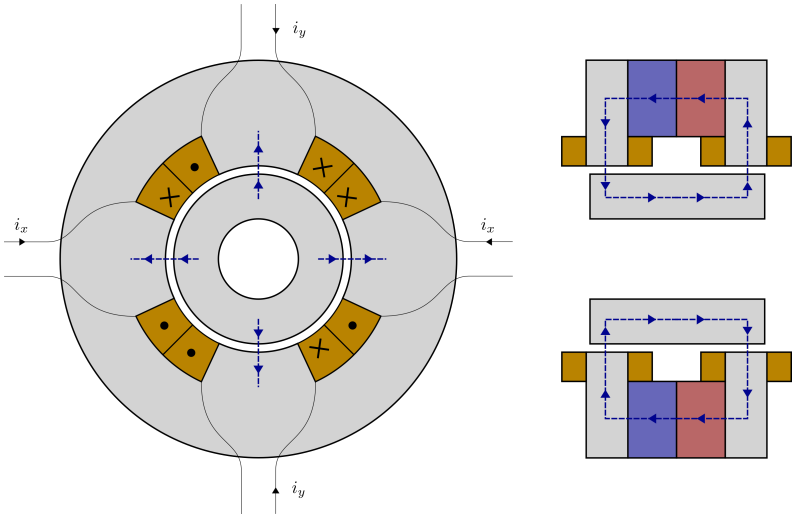

Figure 1.6: Homopolar hybrid-active magnetic bearing. The circulation of the bias magnetic field is axial between the two poles.

The length of the air gap being increased to insert the windings, the currents required to control the rotor are generally higher for such topologies. The remaining iron losses occurring in the SHH-AMB come from the displacements of the rotor but are kept small as this latter is controlled in a centered position.

Axial detent force

The axial detent force in hybrid homopolar magnetic bearings is obtained by adding iron teeth to the rotor such that the circulation of the bias magnetic flux is better if the rotor is axially centered. Such a mechanism is employed in many electromagnetic system to provide a reliable axial force without complexifying the system. An example of a similar mechanism is explained and characterized in [36].

1.2.2 Air gap windings

As the slots in which the windings are placed in common magnetic bearings are removed in the SHH-AMB, this topology employs air gap windings. Such windings must be kept as thin as possible to ensure a sufficiently high magnetic flux density in the air gap. They tend thus to be a manufacturing challenge for their creation as well as their implementation within the bearing. This section reviews the manufacturing process and technologies of the windings employed in slotless machines (motors or bearings) and discuss their cost and feasibility.

Self-supporting windings

Self-supporting windings are made of insulated copper wires that are wounded to form a hollow cylinder (fig. 1.10). An adhesive material is employed to maintain the shape of the winding. The shape given to the turns can be adapted to optimize the performances of the winding by minimizing the length of

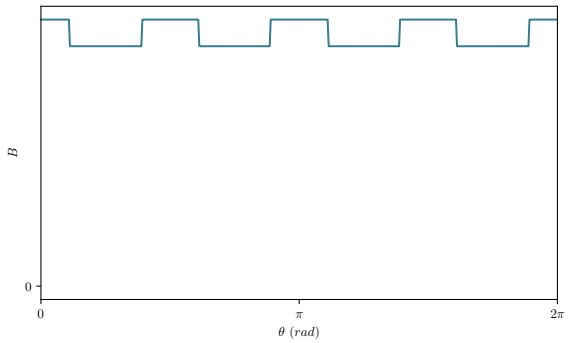

Figure 1.7: Illustration of the air gap radial magnetic field in a HH-AMB as a function of the azimuthal position θ. The polarity of the magnetic flux density is always in the same direction but the amplitude of the magnetic flux density is lower at each slot.

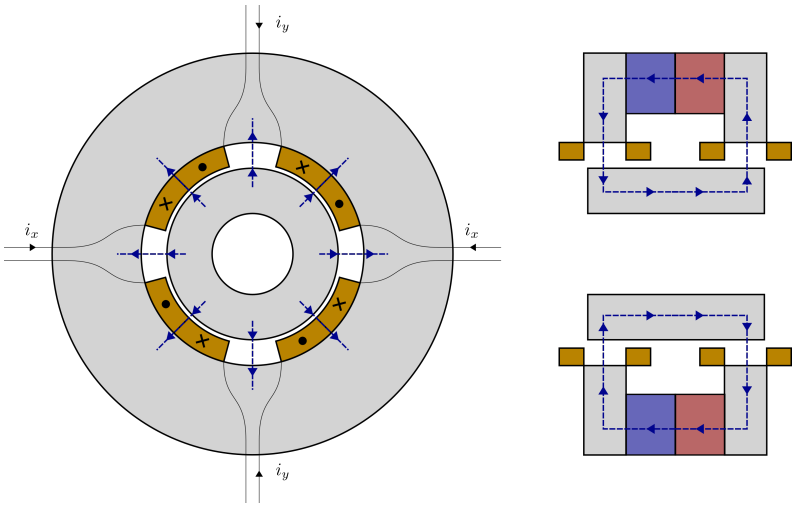

Figure 1.8: Slotless homopolar hybrid-active magnetic bearing.

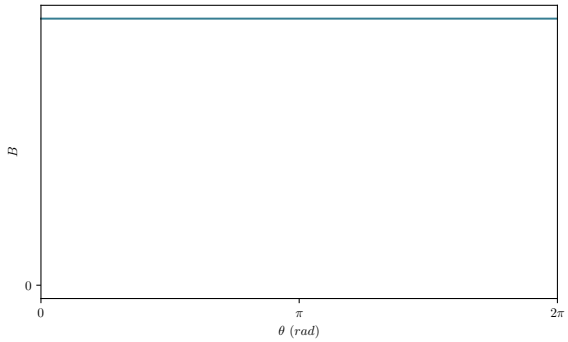

Figure 1.9: Illustration of the air gap radial magnetic field in a SHH-AMB as a function of the azimuthal position θ. The magnetic flux density is axisymmetrical.

the end windings. This kind of winding is widely spread in slotless BLDC motors developed by motor manufacturing companies such as *Maxon*. A rectangular cross-section of the wire can be employed to improve the fill factor of the windings, but the constant shape of this cross-section limits the performances of the winding [37]. This manufacturing technology is cheap and adapted to mass production.

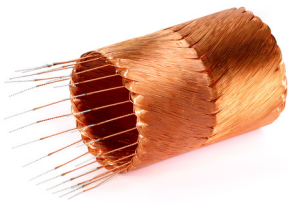

Figure 1.10: Self-supporting winding [38].

Flex-PCB windings

The flex-PCB technology prints the windings of the machine on a flat flexible PCB that is wrapped to form a cylinder that can be inserted within the air gap of the machine (fig. 1.11). In [39], this technology is employed to optimize the windings of a BLDC motor, making use of the ability to change the wire cross-section and to adapt the shape of the turns freely. This manufacturing technology is easy to implement and is adapted for mass production but rather costly for prototyping.

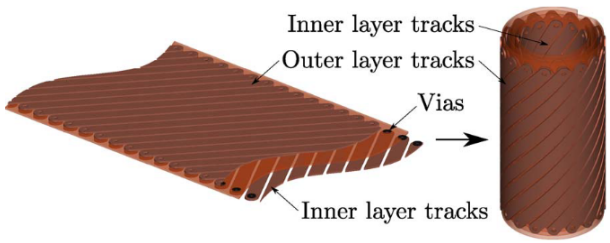

Figure 1.11: Flex-PCB winding. [39].

Laser-cuting

The laser-cutting technology cuts the conductors of the windings into thin copper plate that is foiled to form the hollow cylinder that is placed in the air gap [37] (fig. 1.12). Similarly to Flex-PCB, this technology gives a degree of freedom over the cross-section of the conductors, and allows for complex shapes of the turns. It however suffers from the constant thickness of the copper plate that does not allow to change the height of the conductors. This manufacturing technology is rather cheap and appropriate for prototyping.

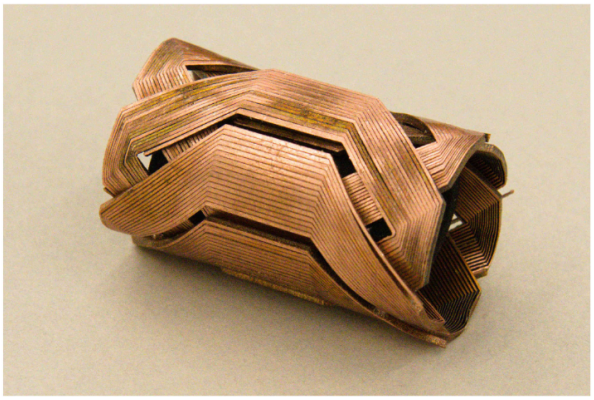

Figure 1.12: Laser-cut winding. [37].

1.2.3 Modeling of AMB

This section gives an overview of the different numerical methods that are employed to develop mathematical models of active magnetic bearings that characterize them locally and globally. The different methods are presented and their pros and cons are listed.

Finite - element analysis (FEA)

The finite element analysis is a local model that discretizes a given geometry in a finite number of elements to form a mesh. Equations modelling the physics are then solved over the mesh to provide an approached solution to the equations. The smaller the size of the elements, the more accurate is the provided solution. The size of elements is adapted to employ small elements where a good accuracy is required and bigger elements where the accuracy is not a concern limit the complexity of the problem and the computation time of the model. For magnetic bearings, the FEA solves the Maxwell's equations to provide the magnetic flux density distribution in the bearing, from which the global characteristics are extracted by integration. Fig. 1.13 shows the FEA applied to a 2-pole homopolar radial magnetic bearing detailed in [2]. This modeling method generally presents high computation time to reach good accuracy but allows for modelling any complex geometry. FEA is also easy to implement if commercial software programs are employed, such as *COMSOL*. FEA is often employed to model machines or to validate other models that are quicker, such as subdomain models, magnetic equivalent circuit or analytical models.

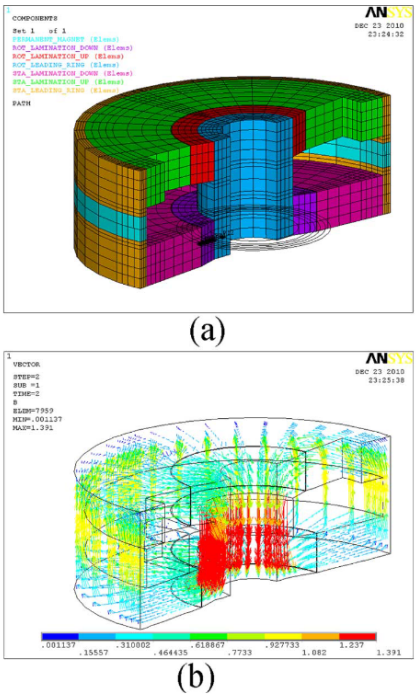

Figure 1.13: FEA of a radial homopolar magnetic bearing [2]. The mesh is shown in (a) and the magnetic flux density is shown in (b).

Subdomain models

Subdomain models or Fourier based models provide a semi-analytical expression of the magnetic flux density within the bearing by solving analytically the magnetic potential vector equation [5]. The solution is semi-analytical because it is given as a Fourier series with a limited number of harmonics. This model provides much lower computation time than FEA for similar accuracy and is thus employed in optimization procedures that require numerous evaluation of the model with different parameters. This method is more challenging to implement and is only feasible for machines presenting a symmetry in one of the 3 dimensions. The SHH-AMB is thus particularly appropriate for the subdomain model, thanks to the axisymmetry of the magnetic flux density distribution. The evaluation of the global characteristics are obtained by integrating analytically the flux density distribution.

Magnetic equivalent circuit

This method models the machine by an equivalent magnetic circuit (MEC) modeling the different parts of the machine and the magnetic permeance that links them to evaluate the magnetic flux that flows in the different regions of the bearing [3], fig. 1.14. More complex geometry can be characterized by a MEC than with the subdomain method, and the computation time is low but, the solution does not provide the magnetic flux density distribution in the air gap but only the magnetic flux from which can be deduced the magnetic flux densities if a uniform distribution is assumed. The global values of the bearing are obtained by integration of the estimated magnetic flux density distribution.

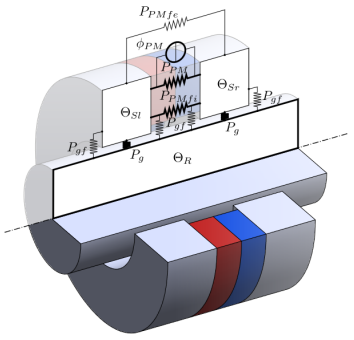

Figure 1.14: Magnetic equivalent circuit method applied to a SHH-AMB [3].

1.2.4 Control strategy

The main concept of active magnetic bearings is that an external controller is required to ensure the stability of the bearing, which is not stable in open loop due to the destabilizing radial detent force acting on the rotor. This section explains why the bearing is not intrinsically stable, how the controller stabilizes the AMB and presents the stability criteria. Control strategies allowing to account for non-idealities of the machine are also explained.

Open loop stability

The open loop dynamic of the system is characterized considering a one degree of freedom - model of the bearing, in which the rotor is only able to move in one radial direction. The position of the rotor along that direction with respect to the center is noted Δ_x. The radial destabilizing force F_x is modeled through a positive radial position stiffness k_ϵ such that: $F_x = k_\epsilon \Delta_x$. The force generated by the windings$F_{i,x}$ is modeled through a current stiffness k_i such that $F_i = k_i i_x$. The equation of the motion applied to the rotor is given by:

$$m_{rotor}\ddot{\Delta_x} = k_i i_x + k_\epsilon x \tag{1.3}$$

The transfer function in the Laplace domain between the input i_x and the output Δ_x is thus given by:

$$H(s) = \frac{\Delta_X(s)}{I_x(s)} = \frac{k_i}{m_{rotor}s^2 - k_\epsilon} \tag{1.4}$$

where the characteristic polynomial of the system is given by: $m_{rotor}s^2 - k_\epsilon$, and have two real poles, being $\sqrt{k_\epsilon/m_{rotor}}$ and $-\sqrt{k_\epsilon/m_{rotor}}$. By inspection of the poles, the system is instable in open loop as one of the poles has a positive real value, which explains the necessity to add a controller.

Position control

Fig. 1.15, inspired from [40] represents a block diagram of the controller dedicated to one axis of actuation of the bearing. In this figure, x_{ref} represents the reference position of the rotor, generally set at zero so that the rotor remains centered. $H_d(s)$ is the previous transfer function to which an additional disturbance force F_d is provided. It is often assumed that the degrees of freedom of the rotor are decoupled, which explains why the controller only considers one of the two degrees of freedom. The coefficients of the PID controller are typically designed to ensure a good disturbance step response rather than a good reference position step response as this latter is not subject to be different from zero over the time.

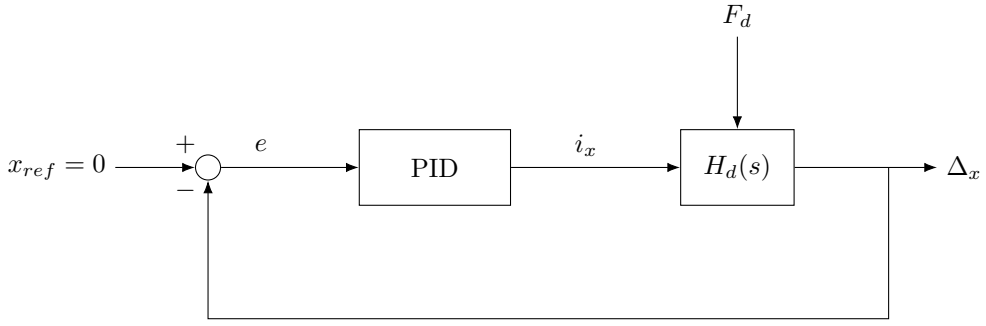

Figure 1.15: Block diagram of the PID controller used in hybrid-active magnetic bearings.

The controller requires a proportional gain sufficiently high so that the destabilizing radial detent force is compensated by this proportional action. If k_ϵ is the position stiffness of the bearing, k_i its current stiffness and k_p is the proportional gain of the controller, the following condition is required to ensure the stability [40]:

$$K_P k_i - k_\epsilon > 0 \tag{1.5}$$

If such a controller is implemented, has two poles located on the imaginary axis and is stable mathematically speaking but not in practice, as it behaves like a harmonic oscillator. The stability of the system is ensured by adding a damping action to the controller that brings back the poles on the left half of the complex plane [40]. The integral term of the controller is not required for the stability of the system but is useful to cancel static errors occurring if constant disturbances are applied.

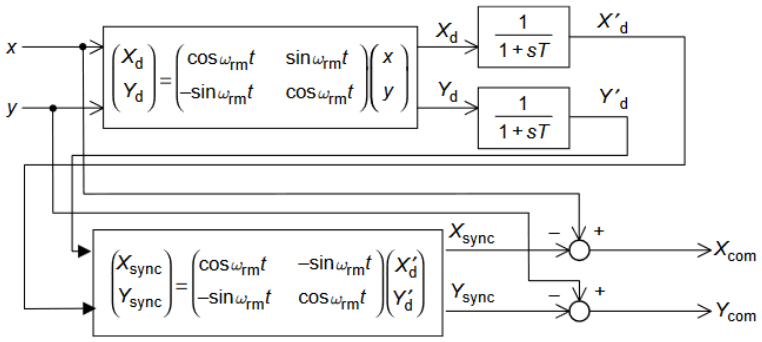

Figure 1.16: Synchronous disturbance elimination: Block diagram. [40]

Unbalanced rotor

Rotating parts, in mechanics, are never perfectly balanced. Their center of mass is always not exactly at the center geometrical center of the part. If the rotor operates at high speed, it is preferable to let it rotate around its center of mass. As the position of the geometrical center is measured, this results in a oscillating position of the rotor at a frequency corresponding to the rotation speed. It is required that the controller ignore this component of the error so that it does not cancel it, which would result in a rotor rotating around its geometrical center. A methodology allowing to get rid of this problem, called the synchronous disturbance elimination, is explained in [40] and illustrated in fig. 1.16. In this method, the position signals x and y are post-processed to remove their undesired component. A transformation of the position of the rotor in a coordinate frame attached to this latter is first performed. In this frame of coordinate, the component related to the balancing non-idealities of the rotor is a DC component that is isolated using a low pass filter giving rise to X'_d and Y'_d, representing the position of the eccentricity of the rotor. These new signals are then expressed in the initial frame of coordinate and subtracted to the measured position of the rotor, giving rise to X_{com} and Y_{com}, that are the signal provided to the controller.

CHAPTER 2

LAYOUT AND PROOF OF CONCEPT

This chapter presents the detailed layout of the SHH-AMB employed in the FESS device as well as the parameters that describe its geometry and its configurations. The general working principle of the bearing is explained and the main global characteristics such as its stiffnesses are identified and defined.

2.1 Detailed layout of the SHH-AMB

A schematic 3D view of the SHH-AMB and its rotor saliencies is presented in fig. 2.1. The stator is made of two ferromagnetic rings between which a permanent magnet ring with axial polarization is inserted. The rotor is made of one hollow piece of ferromagnetic material that has two saliencies, similarly to the stator. The rotor is inserted inside the stator such that the iron saliencies face each other and give rise to an air gap in which two sets of four coils, one set per axis of actuation, are inserted 90° apart. In fig. 2.1, the yellow and green sets of windings actuate respectively the x and y-axis of the bearing. The coils are connected to each other in series and anti-serie, such that the current flows in the direction shown in the figure.

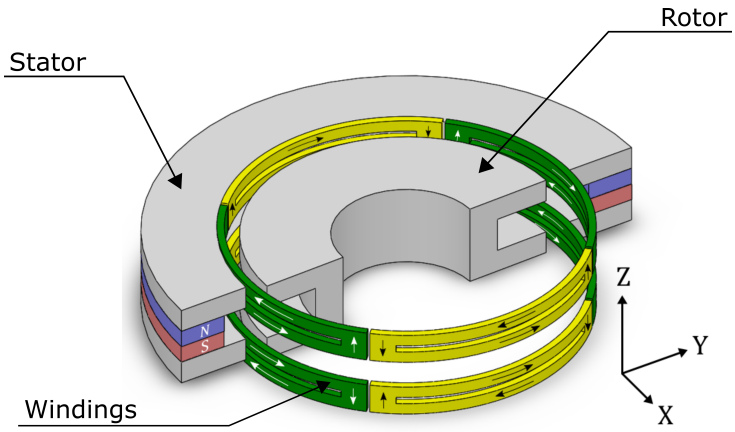

Figure 2.1: 3D cross-sectional view of the SHH-AMB with rotor saliencies.

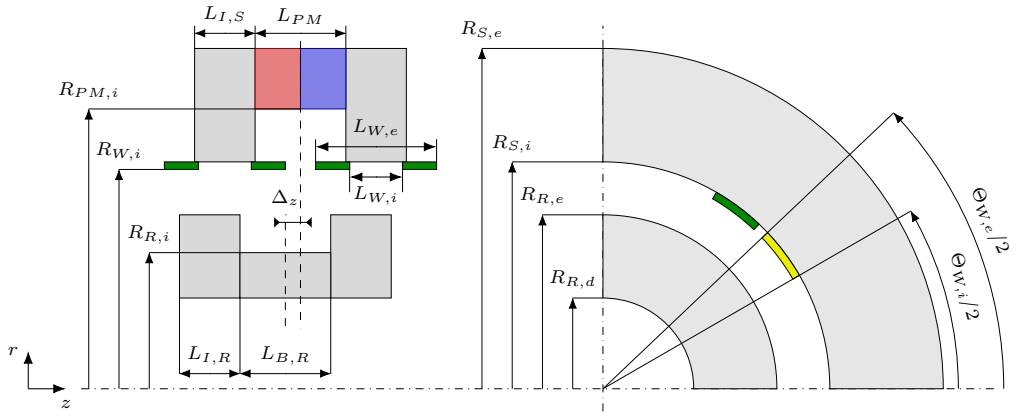

Figure 2.2: Cross-sectional view of the SHH-AMB with rotor saliencies and symbols used to describe its dimensions.

Fig. 2.2 shows a 2D cross-sectional representation of the bearing as well as a detailed definition of each symbol used to describe the bearing's geometry. The stator and rotor iron teeth as well as the width of the space that separates them axially is thus left to be possibly different for the stator and the rotor. The parameter Δ_z describes the axial difference of position between the stator and the rotor center, and is defined as positive if the rotor is above the stator. The parameters describing the end winding leave their configuration is as general as possible and can be made inset or overlapping depending on the value of these parameters. The possible configurations of the end windings are well as their effect on the SHH-AMB are presented in [41]. Each coil of the bearing is made of N_W spires.

2.2 Proof of concept

This section explains the intuitive working principle of the SHH-AMB and its axial stabilization and identify the main global characteristics of the bearing.

2.2.1 General working principle

A key concept of magnetic bearings is the stability of each of the five degrees of freedom of the rotor that need to be guided by the bearing (the axial rotation is left free and is actuated by the electromechanical converter of the FESS). The stability of a degree of freedom around its equilibrium point is assessed by introducing a small displacement along the concerned degree of freedom. The degree of freedom is stable if the resulting force or torque is opposed to this displacement, and unstable otherwise. The five degrees of freedom concerned are the translations in the x, y and z-directions as well as the rotation around the x and y-axes. Some of these are naturally stable thanks to the detent forces and torques acting on the rotor due to the bias magnetic flux density. Others need to be stabilized through an electromagnetic force or torque generated by the currents flowing through the windings. From Earnshaw's theorem, it is not possible to have all the degrees of freedom naturally stable. It is therefore first required to identify the stable and unstable degrees of freedom of the SHH-AMB.

The bias magnetic flux density flowing through the iron teeth, generated by the permanent magnets in the SHH-AMB is illustrated in fig. 2.3. Not considering the windings, the forces acting on the rotor are detent forces.

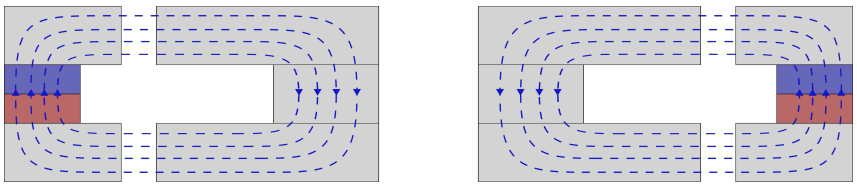

Figure 2.3: Scheme of the bias magnetic flux density lines generated by the permanent magnets.

The axial degree of freedom is first considered. Fig. 2.4 shows the magnetic flux density flowing through the SHH-AMB whose rotor is moved downward. The air gap permeance is lowered because of the unmatching iron teeth, resulting in a decreased magnetic flux. As the detent force acts in a direction that maximizes the magnetic flux, the rotor is pulled upward. The axial degree of freedom is thus naturally stable thanks to the detent forces.

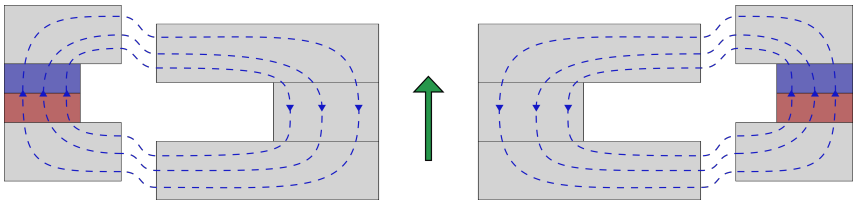

Figure 2.4: Scheme of the bias magnetic flux density lines for an axial displacement of the rotor, the resulting force is stabilizing.

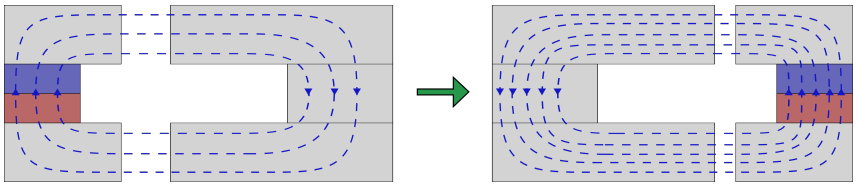

Figure 2.5: Scheme of the bias magnetic flux density lines for a radial displacement of the rotor, the resulting force is destabilizing.

The x and y-translations, are assimilated as a single radial displacement thanks to the homopolar nature of the SHH-AMB. Fig. 2.5 shows the bias magnetic flux resulting from a radial displacement of the rotor. The permeance of the air gap being higher where the air gap is shorter, the magnetic flux density is higher in these regions of the air gap. The resulting detent force is thus aligned with the displacement and tends to pull the rotor is the same way as the motion. This degree of freedom is therefore unstable by nature and is required to be stabilized.

The role of the windings introduced in the air gap formed by the iron teeth is to stabilize the radial degree of freedom. The magnetic flux density of the SHH-AMB when current flows in one of the windings of one axis of actuation is shown in fig. 2.6. The windings add a possibility to apply a force on the rotor through the current that flows through them and can be used to counteract the radial detent force and stabilize the radial degree of freedom.

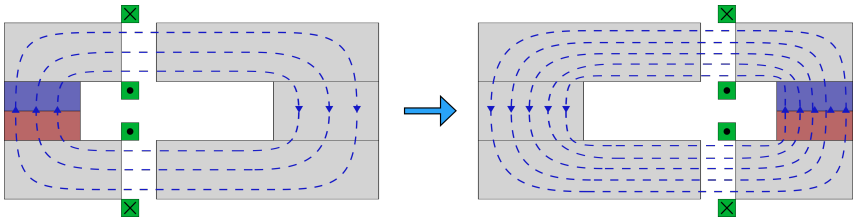

Figure 2.6: Scheme of the bias magnetic flux density lines and the resulting force if current flows in the windings of one of the axis of actuation.

The resulting forces applied to the rotor undergoing a tilt motion (rotation around the x and y-axis) has two origins. The iron teeth of the rotor tend to have an axial motion with respect to the stator teeth, which results in local axial forces that are unbalanced and creates a stabilizing torque that tends to bring the rotor back to its initial position. On the other hand, the length of the air gap is also impacted by the tilt motion that tends to make one of the iron teeth of the rotor closer to the corresponding iron tooth of the stator ones, while the other teeth are brought further away. This configuration gives rise to unbalanced local radial forces that result in torque that tends to destabilize the tilt degree of freedom. The total torque, being the sum of the two effects, is either stabilizing or destabilizing depending on the magnitude of the two effects. The stability of the tilt degree of freedom depends therefore on the geometry of the bearing. Intuitively, bearings showing a bigger radius and shorter height are more stable than high and narrow ones.

2.2.2 Modeling of the magnetic forces and torques

The same concept of small displacement around an equilibrium point is kept for the modeling of the detent forces acting on the rotor. The forces are evaluated by multiplying the small displacements by a constant to perform a linear approximation of the force around the equilibrium point. These value of the slope of these linear approximations are called the *stiffnesses* as they have the same units (N/m or Nm/rad). Regarding the forces generated by the currents flowing through the windings, the same linearization is performed with a concept of *current stiffness* that has (N/A) as units. The electromagnetic forces and torques acting on the rotor are consequently modeled by the following equations.

$$F_{z,mag} = \Delta_z k_z \quad (2.1) \qquad \begin{cases} F_{x,mag} = \Delta_x k_\epsilon - i_x k_i \\ F_{y,mag} = \Delta_y k_\epsilon - i_y k_i \end{cases} \quad (2.2) \qquad \begin{cases} T_{\Psi_x,mag} = \Delta_{\Psi_x} k_\Psi \\ T_{\Psi_y,mag} = \Delta_{\Psi_y} k_\Psi \end{cases} \quad (2.3)$$

where $F_{i,mag}$ is the magnetic force applied to the rotor along the i-axis, Δ_i is the displacement of the

rotor along the i-axis, k_z is the axial stiffness, k_ϵ is the radial stiffness, $T_{\Psi_i,mag}$ is the magnetic torque applied to the rotor along the i-axis, Δ_{Ψ_i} is the tilt angle of the rotor around the i-axis, k_Ψ is the tilt stiffness, i_i is the current flowing through the winding controlling the i-axis and finally, k_i is the current stiffness.

The currents i_x and i_y need to be computed appropriately regarding the position of the rotor in order to stabilize the x and y degrees of freedom. An approximation is made regarding the radial displacements where x and y motion are considered decoupled from each other, which is true only for small displacements. The radial and current stiffnesses are not guaranteed to remain constant during the use of the bearing, as they vary with the axial position of the rotor Δ_z that is defined by the axial equilibrium point. The current and radial stiffnesses must thus be evaluated for a given Δ_z.

CHAPTER 3

MAGNETIC MODEL OF THE BEARING

This chapter presents the model allowing to predict the electromagnetic characteristics of the bearing. As it is meant to be employed in an optimization routine, this model is required to run quickly and to give accurate results. To ensure these performances, a semi-analytical model based on a Fourier approach has been selected. Despite its complex implementation, this approach provides quickly an accurate distribution of the magnetic flux density within the bearing, from which can be extracted the desired global characteristics with the same accuracy. The implementation of this model being challenging, this latter is validated through a finite element analysis (FEA) by taking advantage of its easier implementation. This chapter presents the local computation of the magnetic flux density for a centered rotor. The eccentricity is then introduced and the extraction of the global characteristics as well as their validation are presented. The assessment of the behavior of the model and of the bearing is finally analyzed.

3.1 Magnetic flux density distribution without eccentricity

The implementation of the semi-analytical model is fully detailed in this section. The division in subdomains, required for the Fourier approach, is first presented. The general expression of the magnetic flux density distribution arising from the constitutive equation is then established. The boundary conditions as well as the system of equations solved to obtain the distribution are established and, finally, the results regarding the distributions are presented and compared to the results obtained with the FEA. The procedure to develop this model is widely inspired from [42].

3.1.1 Division in subdomains and boundary conditions

First, a decision must be taken with regard to the coordinate system. Since the SHH-AMB is perfectly axisymmetrical, the magnetic field distributions should not vary along the azimuthal position. The subdomain model will therefore be a 2D model representing a cross-section of the bearing, leaving the r and z-axis as the remaining frame of coordinates. Secondly, a periodization along the z-direction is required to employ the subdomain method. The bearing showing no periodicity along this direction, it is necessary to replicate it. As this artificial replication is a potential source of inaccuracy, the distance between the replications, $2L_{ext}$ must be kept large. The polarization of the permanent magnets of these replications might still either always be in the same way or always be opposed to each other. These two configurations are named respectively constant and alternated. The constant polarization has been chosen and implemented in this work in accordance to what is suggested in [42].

Fig. 3.1 represents the division in subdomains of the SHH-AMB under study. A local coordinate system is assigned to each of these subdomains to simplify the expression of the magnetic flux distributions. The transformation linking the local coordinate system of a region k (r, z_k) with the main one, (r, z), is given by: $z_k = z - \Delta_k$. To each subdomain, a period τ_k is assigned. According to [42], τ_k is defined as the width of the subdomain for those bounded by ferromagnetic materials (e.g., region I or II) and as half of the width of the subdomain otherwise (e.g., region III or VII). This choice ensures the compliance of a part of the boundary conditions introduced in section 3.1.3. The expressions of the τ_k's and Δ_k's are given in 3.1 and 3.2 for each of the seven subdomains.

Table 3.1: Expression of τ_k for each region of the model.

Region	τ_k
I	$2L_{ext} + 2L_{I,S} + L_{PM} - L_{B,R} - 2L_{I,R}$
II	$L_{B,R}$
III	$L_{ext} + L_{I,S} + L_{PM}/2$
IV	$2L_{ext}$
V	L_{PM}
VI	L_{PM}
VII	$L_{ext} + L_{I,S} + L_{PM}/2$

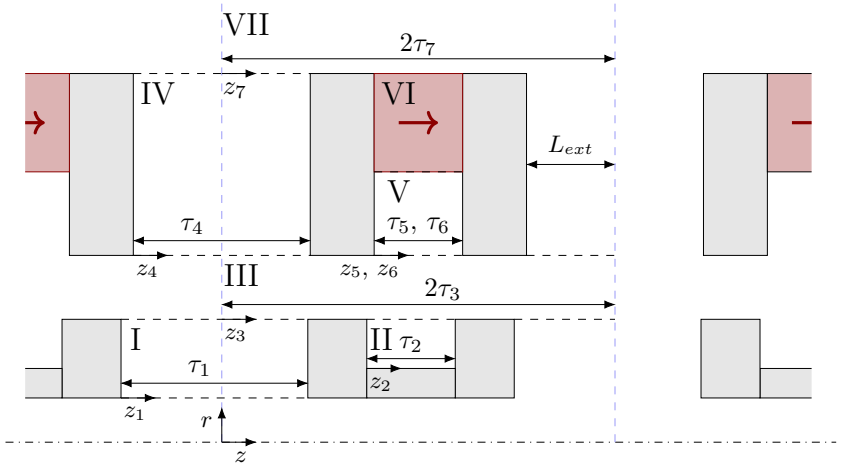

Figure 3.1: Definition of the subdomains, their width as well as their local coordinates system. Grey and red rectangles are respectively ferromagnetic materials and permanent magnets.

The assumptions performed in the implementation of the model are the following:

- **Infinite magnetic permeability:** The magnetic permeability of the ferromagnetic materials is assumed to be infinite.
- **Copper magnetic permeability:** The magnetic permeability of the copper is assumed to be equal to the magnetic permeability of the air.
- **Windings magnetic flux density:** The magnetic flux density engendered by the current flowing through the windings is assumed negligible compared to the magnetic flux density generated by the permanent magnets.
- **Magnetic saturation:** The magnetic saturation in the ferromagnetic materials is not taken into account.
- **Air in the hollow of the rotor:** The magnetic flux density in the hole of the rotor is not modeled, assuming that it does not affect the behavior of the bearing.

Table 3.2: Expression of the Δ_k for each region of the model.

Region	Δ_k
I	$-L_{ext} - L_{I,S} - L_{PM}/2 + \Delta_z + L_{B,R}/2 + L_{I,R}$
II	$L_{ext} + L_{I,S} + L_{PM}/2 + \Delta_z - L_{B,R}/2$
III	0
IV	$-L_{ext}$
V	$L_{ext} + L_{I,S}$
VI	$L_{ext} + L_{I,S}$
VII	0

3.1.2 General expression of the magnetic flux density

According to [43], the general equation governing the distribution of the magnetic flux density B in the magnetic bearing is:

$$\nabla^2 \vec{A} - \mu\sigma \frac{\partial \vec{A}}{\partial t} + \mu\sigma(\vec{v} \times (\nabla \times \vec{A})) = -\mu \vec{J_{ext}} - \mu \nabla \times \vec{M_0} \tag{3.1}$$

where $\vec{A}$ is the magnetic potential vector such that $\nabla \times \vec{A} = \vec{B}$, μ is the magnetic permeability of the medium, σ is the electrical conductivity of the medium, $\vec{v}$ is the speed vector, $\vec{J_{ext}}$ is the imposed current density, $\vec{M_0}$ is the magnetization of the medium and $\vec{B}$ is the magnetic flux density. The problem being static and the magnetic flux density generated by the windings not taken into account, the time-dependent terms of the equation as well the one related to the current density are removed from the equation leading to:

$$\nabla^2 \vec{A} = -\mu \nabla \times \vec{M_0} \tag{3.2}$$

The axisymmetry of the bearing cancelling the azimuthal component of the magnetic field, the magnetic potential vector only has one component in this direction such that: $\vec{A} = A_\theta \, \hat{e_\theta}$. Regarding the magnetization, section 3.1.1 showed that this latter was only axial such that $\vec{M_0} = M_z \, \hat{e_z}$ and constant over the whole region in which it is not null. Working in the cylindrical coordinate system and considering these simplifications, eq. 3.2 becomes:

$$\frac{1}{r}\frac{\partial}{\partial r}\left(r\frac{\partial A_\theta}{\partial r}\right) + \frac{\partial^2 A_\theta}{\partial z^2} - \frac{1}{r^2}A_\theta = \mu_0 \frac{\partial M_z}{\partial r} \tag{3.3}$$

This equation is solved with the variable separation method to obtain the general expressions, as performed in [42]. The resulting general expression of the magnetic flux density of a region k is presented hereafter:

$$\vec{B_k} = B_{r,k}(r, z_k)\vec{e_r} + B_{z,k}(r, z_k)\vec{e_z} \tag{3.4}$$

where:

$$\begin{aligned} B_{r,k}(r, z_k) &= \sum_{n=1}^{\infty} [B_{r,s,k,n}(r) \sin(n\omega_k z_k) + B_{r,c,k,n}(r) \cos(n\omega_k z_k)] \\ B_{z,k}(r, z_k) &= \sum_{n=1}^{\infty} [B_{z,s,k,n}(r) \sin(n\omega_k z_k) + B_{z,c,k,n}(r) \cos(n\omega_k z_k)] + B_{z,k,0} \end{aligned} \tag{3.5}$$

$$\omega_k = \frac{\pi}{\tau_k} \tag{3.6}$$

$$\begin{aligned} B_{r,s,k,n}(r) &= a_{n,k} I_1(n\omega_k r) + b_{n,k} K_1(n\omega_k r) \\ B_{r,c,k,n}(r) &= -c_{n,k} I_1(n\omega_k r) - d_{n,k} K_1(n\omega_k r) \\ B_{z,c,k,n}(r) &= a_{n,k} I_0(n\omega_k r) - b_{n,k} K_0(n\omega_k r) \\ B_{z,s,k,n}(r) &= c_{n,k} I_0(n\omega_k r) - d_{n,k} K_0(n\omega_k r) \\ B_{z,k,0} &= B_{k,0} \end{aligned} \tag{3.7}$$

where I_ν and K_ν are the modified Bessel functions of the first and second kind of order ν and $a_{n,k}$, $b_{n,k}$, $c_{n,k}$, $d_{n,k}$ and $B_{k,0}$ are the unknown coefficients determined by the boundary conditions imposed in each of the regions.

3.1.3 Boundary conditions

Section 3.1.2 solves the magnetic potential equation in each region independently of each other. These solutions need to be connected to each other through the boundary conditions, or to the outside of the model through the limit conditions that appear in the model. The continuity between the domains is imposed by a continuous boundary condition imposing that the normal and tangential components of, respectively, the magnetic flux density B and the magnetic strength H are continuous at the interface between those subdomains. For the subdomains that are in contact with the outside environment, two limit conditions are applied depending on the outside medium. For subdomains interfacing with a ferromagnetic material (gray rectangles in fig. 3.1), the tangential component of the magnetic strength is cancelled at this interface because of the infinite permeability of the ferromagnetic material. This boundary condition is named a Neumann condition. The second limit condition is such that no magnetic flux is allowed to flow through a boundary such that the normal component of the magnetic flux density is cancelled. This condition is known as a Dirichlet condition and is employed at the inner hollow part of the rotor (at $r = R_{R,d}$). The last boundary condition refers to the periodicity of the model and imposes the periodicity of the magnetic flux density in subdomains that cover the whole period of the model.

Radial boundary conditions

Among the aforementioned conditions, the radial ones (parallel to the r-axis) are satisfied by the nature of the general expression of the magnetic flux density. Eq. 3.5 shows that the expression of the magnetic flux density of a region k is a combination of sine and cosine series, for which the coefficients are functions of r. The periodicity required by the periodic boundary conditions is thus satisfied by the definition of the period τ_k of these trigonometric functions (section 3.1.1). Regarding the regions that are bounded by radial boundaries of ferromagnetic materials, the graph of the sine and cosine functions are presented in fig. 3.2 according to the definition of their periods in section 3.1.1. It is observed that, unlike the cosine functions, the sine functions are always null at the two boundaries of the region (at $z_k = 0$ and τ_k). The Neumann's condition requiring a null radial magnetic flux density at these boundaries, the coefficients of the cosine terms in the Fourier series are imposed at zero, and the c and d coefficients of these regions are thus null. The axial component of the magnetic flux density B_z is consequently only composed of cosine terms, by inspection of the analytical expressions in eq. 3.7.

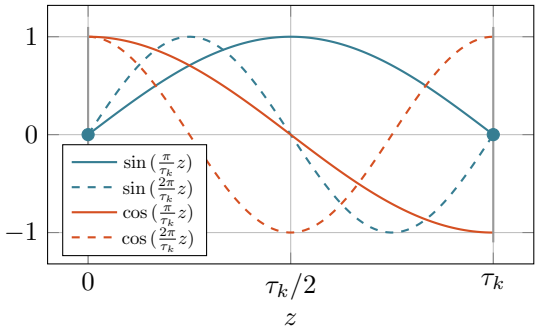

Figure 3.2: Sine and cosine functions over a τ_k width (first and second harmonics) in a regions bounded by ferromagnetic materials. The sine functions are always equal to zero at the limit of the region k.

Number of unknowns

The number of equations that need to be established being equal to the number of unknowns, it is helpful to know what is the exact number of unknowns in the model. For the sake of clarity, it is considered, unless mentioned, that the number of harmonics employed is the same for every subdomain and noted as n. The solution of domains bounded by periodic conditions are composed of one constant unknown term $B_{k,0}$ as well as four unknown a, b, c, and d per harmonic. Such regions lead thus to $4n+1$ unknowns. Because two coefficients of the other regions have been taken away to ensure the compliance to a part of the Neumann conditions, these regions lead to $2n + 1$ unknowns. The model being made of two domains with periodic boundary conditions and five domains bounded by Neumann boundary conditions, the model leads to $18n+7$ unknowns that are determined by the boundary conditions applied to the axial (parallel to the z-axis) boundaries of the domains.

Full Neumann limit condition

This condition concerns the domains that have at least one of their two axial boundaries made of a ferromagnetic material. It appears that only the region II and its inner boundary at a radius $R_{R,i}$ fits the requirements. The Neumann condition is written mathematically as:

$$B_{z,2}(R_{R,i}, z) = 0 \tag{3.8}$$

Leading to three sub-conditions:

$$\begin{aligned} B_{z,s,2}(R_{R,i}) &= 0 \\ B_{z,c,2}(R_{R,i}) &= 0 \\ B_{z,2,0} &= 0 \end{aligned} \tag{3.9}$$

Since the first equation of these three sub-conditions is already satisfied (section 3.1.3), only the two last are kept, leading to the n+1 useful equations:

$$\begin{aligned} a_{p,2} I_0(p\omega_2 R_{R,i}) - b_{p,2K} K_0(p\omega_2 R_{R,i}) &= 0 \\ B_{2,0} &= 0 \end{aligned} \tag{3.10}$$

with $p \in (1, n)$

Full continuous boundary condition

This condition relates to the continuity of the magnetic field along an interface between two regions covering the same axial length. Regarding the studied bearing, only the axial boundary between region V and VI at $R_{PM,i}$ matches the requirements. Mathematically, and knowing that for any region $\vec{H} = 1/\mu\ (\vec{B} - \mu_0 \vec{M})$, the continuity is written as:

$$\begin{aligned} B_{r,5}(R_{PM,i}, z) &= B_{r,6}(R_{PM,i}, z) \\ \mu_6 B_{z,5}(R_{PM,i}, z) &= \mu_5 (B_{z,6}(R_{PM,i}) - \mu_0 M_{z,6}) \end{aligned} \tag{3.11}$$

The development in Fourier series of this equation and considering regions of equal width, eq. 3.11 leads to the following sub-conditions:

$$\begin{aligned} B_{r,s,6,p}(R_{PM,i}) &= B_{r,s,5,p}(R_{PM,i}) \\ B_{r,c,6,p}(R_{PM,i}) &= B_{r,c,5,p}(R_{PM,i}) \\ \frac{\mu_5}{\mu_6} B_{z,s,6,p}(R_{PM,i}) &= B_{z,s,5,p}(R_{PM,i}) \\ \frac{\mu_5}{\mu_6} B_{z,c,6,p}(R_{PM,i}) &= B_{z,c,5,p}(R_{PM,i}) \\ \frac{\mu_5}{\mu_6} \Big(B_{z,0,6}(R_{PM,i}) - \mu_0 M_{0,6} \Big) &= B_{z,0,5}(R_{PM,i}) \end{aligned} \tag{3.12}$$

The second and third equations being redundant, only the first, fourth, and fifth sub-conditions are kept leading to the $2n + 1$ equations on the unknown coefficients:

$$\begin{aligned} a_{n,6} I_1(p\omega_6 R_{PM,i}) + b_{p,6} K_1(p\omega_6 R_{PM,i}) &= a_{p,5} I_1(p\omega_5 R_{PM,i}) + b_{p,5} K_1(p\omega_5 R_{PM,i}) \\ \frac{\mu_5}{\mu_6} \Big(a_{p,6} I_0(p\omega_6 R_{PM,i}) - b_{p,6} K_0(p\omega_6 R_{PM,i}) \Big) &= a_{p,5} I_0(p\omega_5 R_{PM,i}) - b_{p,5} K_0(p\omega_5 R_{PM,i}) \\ \frac{\mu_5}{\mu_6} \Big(B_{0,6} - \mu_0 M_{0,6} \Big) &= B_{0,5} \end{aligned} \tag{3.13}$$

with $p \in (1, n)$

Combination of Neumann and continuous boundary conditions

This condition concerns the boundaries that are either in contact with multiple regions and ferromagnetic materials, or whose axial width is not the same as the one of the single region which it is in contact with. This condition is required at three boundaries, the two axial boundaries of region III at $R_{R,e}$ and $R_{S,i}$ as well as in region VII at $R_{S,e}$.

Region III, $r = R_{R,e}$:

The continuity of the radial magnetic flux density is first imposed between region III and I which gives rise to the following equation:

$$\sum_{p=1}^{n}\Big(B_{r,s,1,p}(R_{R,e})\sin\left(p\omega_1 z_1\right)\Big) = \sum_{q=1}^{n}\Big(B_{r,s,3,q}(R_{R,e})\sin\left(q\omega_3 z_3\right) + B_{r,c,3,n}(R_{R,e})\cos\left(n\omega_3 z_3\right)\Big) \qquad z \in [\Delta_1, \Delta_1 + \tau_1] \tag{3.14}$$

As regions III and I do not have the same width, as suggested in [42], the terms of the equation with a sine function of pulsation $n\omega_1$ are correlated over a period of region I. As a result, the sum over the harmonics of region I disappears, which gives rise to the n sub-conditions:

$$B_{r,s,1,p}(R_{R,e}) = \sum_{q=1}^{n}\Big(B_{r,s,3,q}(R_{R,e})\epsilon_{s,1,3}(p,q) + B_{r,c,3,q}(R_{R,e})\epsilon_{c,1,3}(p,q)\Big) \tag{3.15}$$

where the ϵ functions are the correlation functions resulting from this operation and are defined as:

$$\begin{aligned}\epsilon_{s,j,k}(p,q) &= \frac{2}{\tau_j}\int_{\Delta_j}^{\Delta_j+\tau_j}\sin\left(q\omega_k z_k\right)\sin\left(p\omega_j z_j\right)dz \\ \epsilon_{c,j,k}(p,q) &= \frac{2}{\tau_j}\int_{\Delta_j}^{\Delta_j+\tau_j}\cos\left(q\omega_k z_k\right)\sin\left(p\omega_j z_j\right)dz\end{aligned} \tag{3.16}$$

By applying the same procedure for the continuity at the interface of regions II and III, the following n equations are obtained:

$$B_{r,s,2,p}(R_{R,e}) = \sum_{q=1}^{n}\Big(B_{r,s,3,q}(R_{R,e})\epsilon_{s,2,3}(p,q) + B_{r,c,3,q}(R_{R,e})\epsilon_{c,2,3}(p,q)\Big) \tag{3.17}$$

Regarding the magnetic strength, the condition requires the axial component of the magnetic strength of region III to be either equal to the one of region I, to the one of region II or to zero, depending on the z-position. Mathematically, this condition is written as:

$$H_{z,3}(R_{R,e}) = \begin{cases} H_{z,1}(R_{R,e}) + H_{z,2}(R_{R,e}) & z_3 \in (\Delta_1, \Delta_1+\tau_1) \text{ or } z_3 \in (\Delta_2, \Delta_2+\tau_2) \\ 0 & \text{Otherwise}\end{cases} \tag{3.18}$$

The same idea of correlation is applied to get rid of the summation over the harmonics. However, the correlation is performed with a sine and a cosine function to obtain all the equations required. The resulting $2n$ sub-conditions are written as:

$$\begin{aligned} B_{z,s,3,n} &= \frac{\mu_3}{\mu_1}\Big(\sum_{m=1}^{n}B_{z,c,1,m}\kappa_{c,1,3}(m,n) + B_{z,0,1}\kappa_{0,1,3}(n)\Big) \\ &\quad + \frac{\mu_3}{\mu_2}\Big(\sum_{m=1}^{n}B_{z,c,2,m}\kappa_{c,2,3}(m,n) + B_{z,0,2}\kappa_{0,2,3}(n)\Big) \\ B_{z,c,3,n} &= \frac{\mu_3}{\mu_1}\Big(\sum_{m=1}^{n}B_{z,c,1,m}\zeta_{c,1,3}(m,n) + B_{z,0,1}\zeta_{0,1,3}(n)\Big) \\ &\quad + \frac{\mu_3}{\mu_2}\Big(\sum_{n=1}^{n}B_{z,c,2,n}\zeta_{c,2,3}(m,n) + B_{z,0,2}\zeta_{0,2,3}(n)\Big)\end{aligned} \tag{3.19}$$

all the terms of this equation being evaluated at $r = R_{R,e}$. The corresponding correlation functions ζ and κ are defined hereafter:

$$\begin{aligned}
\kappa_{c,j,k}(m,n) &= \frac{1}{\tau_k}\int_{\Delta_j}^{\Delta_j+\tau_j} \cos\left(m\omega_j z_j\right)\sin\left(n\omega_k z_k\right)dz \\
\kappa_{0,j,k}(n) &= \frac{1}{\tau_k}\int_{\Delta_j}^{\Delta_j+\tau_j} \sin\left(n\omega_k z_k\right)dz \\
\zeta_{c,j,k}(m,n) &= \frac{1}{\tau_k}\int_{\Delta_j}^{\Delta_j+\tau_j} \cos\left(m\omega_j z_j\right)\cos\left(n\omega_k z_k\right)dz \\
\zeta_{0,j,k}(n) &= \frac{1}{\tau_k}\int_{\Delta_j}^{\Delta_j+\tau_j} \cos\left(n\omega_k z_k\right)dz
\end{aligned} \tag{3.20}$$

Region III, $r = R_{S,i}$:

By analogy and by replacing the regions I and II by IV and V respectively, the condition imposed at $R_{S,i}$ gives rise to the following $4n$ equations:

$$\begin{aligned}
B_{r,s,4,m} &= \sum_{n=1}^{n}\Big(B_{r,s,3,n}\epsilon_{s,4,3}(m,n) + B_{r,c,3,n}\epsilon_{c,4,3}(m,n)\Big) \\
B_{r,s,5,m} &= \sum_{n=1}^{n}\Big(B_{r,s,3,n}\epsilon_{s,5,3}(m,n) + B_{r,c,3,n}\epsilon_{c,5,3}(m,n)\Big) \\
B_{z,s,3,n} &= \frac{\mu_3}{\mu_4}\Big(\sum_{m=1}^{n} B_{z,c,4,m}\kappa_{c,4,3}(m,n) + B_{z,0,4}\kappa_{0,4,3}(n)\Big) \\
&\quad + \frac{\mu_3}{\mu_5}\Big(\sum_{m=1}^{n} B_{z,c,5,m}\kappa_{c,5,3}(m,n) + B_{z,0,5}\kappa_{0,5,3}(n)\Big) \\
B_{z,c,3,n} &= \frac{\mu_3}{\mu_4}\Big(\sum_{m=1}^{n} B_{z,c,4,m}\zeta_{c,4,3}(m,n) + B_{z,0,4}\zeta_{0,4,3}(n)\Big) \\
&\quad + \frac{\mu_3}{\mu_5}\Big(\sum_{m=1}^{n} B_{z,c,5,m}\zeta_{c,5,3}(m,n) + B_{z,0,5}\zeta_{0,5,3}(n)\Big)
\end{aligned} \tag{3.21}$$

all the terms of these equations being evaluated at $r = R_{S,i}$.

Region VII, $r = R_{S,e}$:

Regarding the edge of region VII at $R_{S,e}$, the same analogy is performed by replacing regions III and V by VII and VI respectively. However, the magnetic strength of region VI is slightly modified due to the presence of a magnetization in this region. These conditions lead to the $4n$ equations:

$$\begin{aligned}
B_{r,s,4,m} &= \sum_{n=1}^{n}\Big(B_{r,s,7,n}\epsilon_{s,4,7}(m,n) + B_{r,c,7,n}\epsilon_{c,4,7}(m,n)\Big) \\
B_{r,s,6,m} &= \sum_{n=1}^{n}\Big(B_{r,s,7,n}\epsilon_{s,6,7}(m,n) + B_{r,c,7,n}\epsilon_{c,6,7}(m,n)\Big) \\
B_{z,s,7,n} &= \frac{\mu_7}{\mu_4}\Big(\sum_{m=1}^{n} B_{z,c,4,m}\kappa_{c,4,7}(m,n) + B_{z,0,4}\kappa_{0,4,7}(n)\Big) \\
&\quad + \frac{\mu_7}{\mu_6}\Big(\sum_{m=1}^{n} B_{z,c,6,m}\kappa_{c,6,7}(m,n) + (B_{z,0,6} - \mu_0 M_{0,6})\kappa_{0,6,7}(n)\Big) \\
B_{z,c,7,n} &= \frac{\mu_7}{\mu_4}\Big(\sum_{m=1}^{n} B_{z,c,4,m}\zeta_{c,4,7}(m,n) + B_{z,0,4}\zeta_{0,4,7}(n)\Big) \\
&\quad + \frac{\mu_7}{\mu_6}\Big(\sum_{m=1}^{n} B_{z,c,6,m}\zeta_{c,6,7}(m,n) + (B_{z,0,6} - \mu_0 M_{0,6})\zeta_{0,2,7}(n)\Big)
\end{aligned} \tag{3.22}$$

Air to infinity

This condition concerns the regions VII that is defined until an infinite-radius. As the presence of the magnetic bearing should not give rise to infinite magnetic flux density, it is imposed that the expression of the magnetic flux density of region VII converges to a finite number as r tends to infinity. Mathematically, this condition is written:

$$\begin{aligned} \lim_{r\to\infty} B_r(r,z) &\in \mathbb{R} \\ \lim_{r\to\infty} B_z(r,z) &\in \mathbb{R} \end{aligned} \tag{3.23}$$

The coefficient of the Fourier series forming the expression of the magnetic flux density of region VII are made of the contribution of two modified Bessel functions of the first and second kind. The graphs of these functions of order 0 and 1 are illustrated in fig. 3.3 and show that the modified Bessel function of the first kind ($I_\nu(x)$) tends to infinity for an infinite argument. The coefficients multiplying this function in region VII (i.e: $a_{n,7}$ and $c_{n,7}$) are thus imposed to zero to keep a finite solution. Regarding the continuous component of the axial magnetic flux density $B_{7,0}$, it is also set to be equal to zero in order to ensure the magnetic flux conservation through the closed surface that is the hollow disk of infinite radius located between two repetitions of the bearing. This condition therefore leads to $2n+1$ equations.

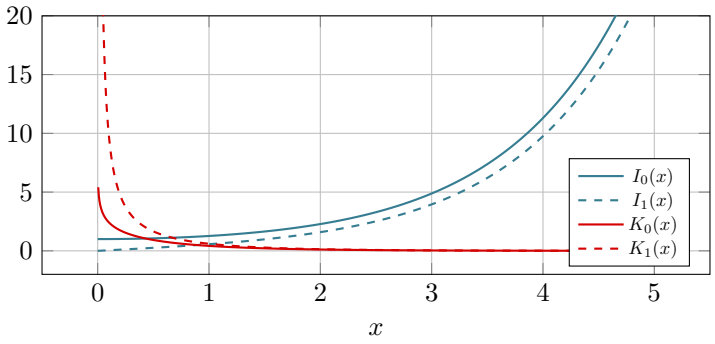

Figure 3.3: Modified Bessel functions of the first and second kind of order 0 and 1. The first kind ($I_\nu(x)$) tends to infinity with x.

Dirichlet boundary condition

This condition concerns the inner boundary of region I ($R_{R,d}$) where the normal component of the magnetic flux density is cancelled, leading to the n equations:

$$B_{r,s,1,n}(R_{R,d}) = a_{n,1} I_1(n\omega_1 R_{R,d}) + b_{n,1} K_1(n\omega_1 R_{R,d}) = 0 \tag{3.24}$$

Ampere's law

Applying Ampere's law around specific closed curves establishes additional equations determining the continuous components of the axial magnetic flux densities. The specific curves in question are rectangles spreading over the whole period of the model at each radius where a combination of a Neumann and a continuous condition is applied, as illustrated in fig. 3.4 for one of the three possible curves. The length of the vertical path of the curves dx tends then to zero to cancel the contribution of the radial components. As the curve goes through a whole period of the repetition, the sine, and cosine terms of the Fourier series are canceled in the integration leaving only the continuous components. The three final obtained equations are presented hereafter:

$R_{R,e}$:

$$\begin{aligned} \int_{\Delta_1}^{\Delta_1+\tau_1} \frac{B_{z,1}}{\mu_1} dz + \int_{\Delta_2}^{\Delta_2+\tau_2} \frac{B_{z,2}}{\mu_2} dz + 0 - \int_{\Delta_3}^{\Delta_3+2\tau_3} \frac{B_{z,3}}{\mu_3} dz + 0 = 0 \\ \iff \frac{B_{01}}{\mu_1}\tau_1 = \frac{B_{03}}{\mu_3} 2\tau_3 \end{aligned} \tag{3.25}$$

$R_{S,i}$:

$$\begin{aligned} \int_{\Delta_4}^{\Delta_4+\tau_4} \frac{B_{z,4}}{\mu_4} dz + \int_{\Delta_5}^{\Delta_5+\tau_5} \frac{B_{z,5}}{\mu_5} dz + 0 - \int_{\Delta_3}^{\Delta_3+\tau_3} \frac{B_{z,3}}{\mu_3} dz + 0 = 0 \\ \iff \frac{B_{04}}{\mu_4}\tau_4 + \frac{B_{05}}{\mu_5}\tau_5 = \frac{B_{03}}{\mu_3} 2\tau_3 \end{aligned} \tag{3.26}$$

$R_{S,e}$:

$$\begin{aligned}\int_{\Delta_4}^{\Delta_4+\tau_4}\frac{B_{z,4}}{\mu_4}dz+\int_{\Delta_6}^{\Delta_6+\tau_6}\left(\frac{B_{z,6}}{\mu_6}-\frac{\mu_0}{\mu_6}M_{0,6}\right)dz+0-\int_{\Delta_7}^{\Delta_7+\tau_7}\frac{B_{z,7}}{\mu_7}dz+0=0\\ \iff \frac{B_{04}}{\mu_4}\tau_4+\left(\frac{B_{06}}{\mu_6}-\frac{\mu_0}{\mu_6}M_{06}\right)\tau_6=0\end{aligned} \tag{3.27}$$

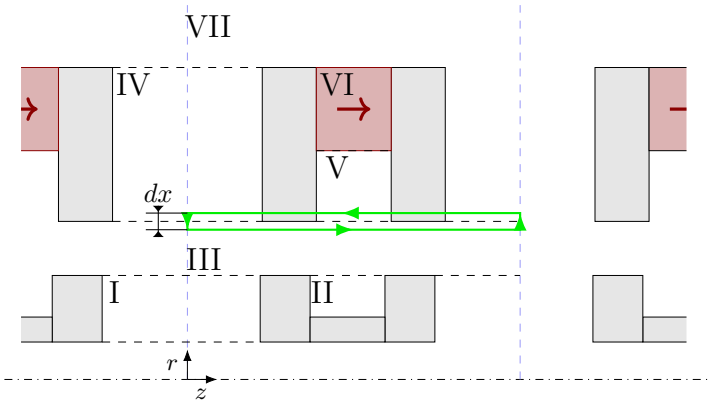

Figure 3.4: Illustration of one of the three possible closed loops used for the integration in the Ampere's law ($r = R_{R,i}$).

Magnetic flux conservation

Considering the $18n+6$ equations that are established, one additional equation is required to determine the $18n + 7$ unknowns. This equation is given by the conservation of the magnetic flux that is applied around one of the ferromagnetic blocks appearing in the model. The sum of the flux flowing through each of these surfaces must be equal to zero. The choice of the block around which the conservation of the magnetic flux is applied is arbitrary, and several solutions are possible. It was chosen to consider the left tooth of the stator.

The magnetic flux entering the stator tooth via the region IV, ϕ_4 is computed with the following integral:

$$\phi_4 = 2\pi\int_{R_{S,i}}^{R_{S,e}} B_{z,4}(r,\tau_4)rdr \tag{3.28}$$

that is further developed using the expression of the magnetic flux density:

$$\phi_4 = \pi B_{0,4}(R_{S,e}^2-R_{S,i}^2)+2\pi\sum_{q=1}^{n}(-1)^q a_{q,4}\int_{R_{S,i}}^{R_{S,e}} rI_0(q\omega_4 r)dr-(-1)^q b_{q,4}\int_{R_{S,i}}^{R_{S,e}} rK_0(q\omega_4 r)dr \tag{3.29}$$

where the integrals of the modified Bessel functions are evaluated numerically.

The expressions of the magnetic flux coming from regions V and VI are obtained by analogy to the one of region IV:

$$\begin{aligned}\phi_6 &= -\pi B_{0,6}(R_{S,e}^2-R_{PM,i}^2)-2\pi\sum_{q=1}^{n}(-1)^q a_{q,6}\int_{R_{PM,i}}^{R_{S,e}} rI_0(q\omega_6 r)dr\\ &\quad-(-1)^q b_{q,6}\int_{R_{PM,i}}^{R_{S,e}} rK_0(q\omega_6 r)dr\\ \phi_5 &= -\pi B_{0,5}(R_{PM,i}^2-R_{S,i}^2)-2\pi\sum_{q=1}^{n}(-1)^q a_{q,5}\int_{R_{S,i}}^{R_{PM,i}} rI_0(q\omega_5 r)dr\\ &\quad-(-1)^q b_{q,5}\int_{R_{S,i}}^{R_{PM,i}} rK_0(q\omega_5 r)dr\end{aligned} \tag{3.30}$$

The expression of the magnetic flux entering the stator tooth from the region VII is given by the following integral:

$$\phi_7 = 2\pi \int_{L_{ext}}^{L_{ext+L_{I,S}}} -R_{S,e} B_{r,7}(R_{S,e}, z) dz \tag{3.31}$$

that is further developed using the expression of the magnetic flux density:

$$\begin{aligned} \phi_7 = \sum_{n=1}^{n} & -2\pi R_{S,e} b_{n,7} K_1(n\omega_7 R_{S,e}) \int_{L_{ext}}^{L_{ext+L_{I,S}}} \sin(n\omega_7 z) dz \\ & + 2\pi R_{S,e} d_{n,7} K_1(n\omega_7 R_{S,e}) \int_{L_{ext}}^{L_e xt+L_{I,S}} \cos(n\omega_7 z) dz \end{aligned} \tag{3.32}$$

The expression of the flux entering the stator from region III is obtained by analogy to the one of region VII giving:

$$\begin{aligned} \phi_3 = \sum_{q=1}^{n} & 2\pi R_{S,i} (a_{q,3} I_1(q\omega_3 R_{S,i}) + b_{n,3} K_1(q\omega_3 R_{S,i})) \int_{L_{ext}}^{L_{ext+L_{I,S}}} \sin(q\omega_3 z) dz \\ & - 2\pi R_{S,i} (c_{q,3} I_1(q\omega_3 R_{S,i}) + d_{q,3} K_1(q\omega_3 R_{S,i})) \int_{L_{ext}}^{L_{ext+L_{I,S}}} \cos(q\omega_3 z) dz \end{aligned} \tag{3.33}$$

The equation of the magnetic flux conservation is then obtained by summing these fluxes and equalling the result to zero, giving:

$$\phi_4 + \phi_7 + \phi_6 + \phi_5 + \phi_3 = 0 \tag{3.34}$$

Number of harmonics

It was first considered that the number of harmonics n employed in each region was the same. The more harmonics are employed and the more accurate is the solution. However, for a same accuracy, regions with larger τ_k need more harmonics than shorter regions. Employing the same number of harmonics in every region is thus not the mos optimized choice regarding the size of the system of equations. A more appropriate choice is to employ more harmonics in wider regions than in shorter ones, which ensures a similar accuracy in every region.

The number of harmonics employed in a region k in the model is set proportionally to its width τ_k. As region II is one of the smallest regions, the number of harmonics employed in this region is left as a parameter from which the number of harmonics employed in the other regions is determined by a law of proportionality.

Conditioning of the matrix

The equations of the boundary conditions being linear with respect to the unknowns, they are written under the classical form of a linear system of equation $Ax = B$ that is solved with any numerical solver. The accuracy of the answer provided by the solver will be affected by the conditioning of the matrix A that characterizes the ratio of the relative error on the unknown vector x and the relative variation on the source term B such that:

$$K(A) = ||A^{-1}|| \cdot ||A|| \tag{3.35}$$

where $K(A)$ is the conditioning number of matrix A. A numerical solver taking a poorly conditioned matrix (high $K(A)$) outputs an inaccurate solution due to numerical errors. The conditioning number of A must thus be kept as small as possible.

The general form of most of the equations coming from the boundary conditions is:

$$aI_k(n\omega R) + bK_k(n\omega R) = b \tag{3.36}$$

They are thus generally composed of the sum of two terms multiplied by a modified Bessel function of the first and second kind. The fig. 3.3 shows that these two functions, for a same argument, might have output differences of several orders of magnitude, which typically degrades the conditioning of the system. The argument of the Bessel functions increases with the number of harmonics employed in the regions, which prevents from enjoying the increased accuracy of the increased number of harmonics.

It is possible to increase the number of harmonics without degrading the conditioning of the matrix if the equations are scaled over the modified Bessel functions such that:

$$a\frac{I_k(n\omega R)}{I_0(n\omega R_0)} + b\frac{K_k(n\omega R)}{K_0(n\omega R_0)} = b \tag{3.37}$$

where R_0 is a radius that belongs to the region concerned. The equation is slightly modified to replace the modified Bessel function by a ratio of the functions that have the same order of magnitude making the two terms of the equation similar. The solution of such a system does not provide directly the a, b, c and d coefficients but the value of, for example, $aI_0(n\omega R_0)$ from which the value of the unknown coefficients must be extracted. The value of R_0, should be chosen such that the two ratios of the equation are as close as possible to each other. After trying different possibilities, the average of the outer and inner radii of the region concerned by the equation is employed.

Exponentially scaled modified Bessel functions

Thanks to the scaling, the value of the modified Bessel functions is not present in the equations but still required in the evaluation of the ratios. Numerically, this leads to a problem regarding the floating point precision of computers that does not allow evaluating the high or small values that these functions can output for high number of harmonics. Exponentially scaled modified Bessel functions allow evaluating the ratios required in the equations without evaluating the actual values of the modified Bessel functions. The definitions of these functions are defined hereafter:

$$\begin{aligned} I_{\nu,e}(x) &= e^{-x}I_\nu(x) \\ K_{\nu,e}(x) &= e^{x}K_\nu(x) \end{aligned} \tag{3.38}$$

These exponentially scaled modified Bessel functions can consequently be evaluated for a higher argument before reaching the maximum or minimum floating point value of the computer, as they are less increasing than the classical modified Bessel functions. The ratios of the two modified Bessel functions are computed as performed in the example below:

$$\frac{I_0(n\omega R)}{I_0(n\omega R_0)} = \frac{e^{n\omega R}I_{0,e}(n\omega R)}{e^{n\omega R_0}I_{0,e}(n\omega R_0)} = e^{n\omega(R-R_0)}\frac{I_{0,e}(n\omega R)}{I_{0,e}(n\omega R_0)} \tag{3.39}$$

3.1.4 Results

A test machine, whose dimensions are given in table 3.3, is created for validation purpose. The distance seperating two models is set at 50 mm. The magnetic flux density distributions over the bearing have then been evaluated with the Fourier model for different numbers of harmonics and compared to the results obtained with a 2D Finite element analysis (FEA) in which the same assumptions employed to implement the Fourier based model are reproduced. Fig. 3.5 shows the radial and axial components of the magnetic flux density as a function of the axial position z in the middle of the air gap as it is the most critical distribution regarding the global values that will be extracted from the model. The number given for the Fourier based model (FBX) corresponds to the number of harmonics employed in region II. Appendix A shows that the limit boundary conditions are well fulfilled by the output solution.

Table 3.3: Dimensions of the test machine.

Parameter	value	unit
$L_{I,S}$	10	mm
L_{PM}	15	mm
$L_{I,R}$	10	mm
$L_{B,R}$	15	mm
$R_{R,d}$	45	mm
$R_{R,i}$	60	mm
$R_{R,e}$	72	mm
$R_{S,i}$	75	mm
$R_{PM,i}$	85	mm
$R_{S,e}$	105	mm
D_z	-5	mm
B_{rem}	1.44	T
$\mu_{r,PM}$	1.05	/

It is observed on this graph that, as expected, the solution given by the FB model tends towards the results given by the FEA as the number of harmonics is increased. Although a similar model, the convergence is slower than in [5]. The reason for this difference is the presence of 4 additional ferromagnetic corners at the rotor iron teeth, which tend to make the axial component of the magnetic flux density discontinuous, requiring a higher number of harmonics to be reached accurately with the Fourier series. The difficult convergence of the model is also explained by the presence of an additional combination of a

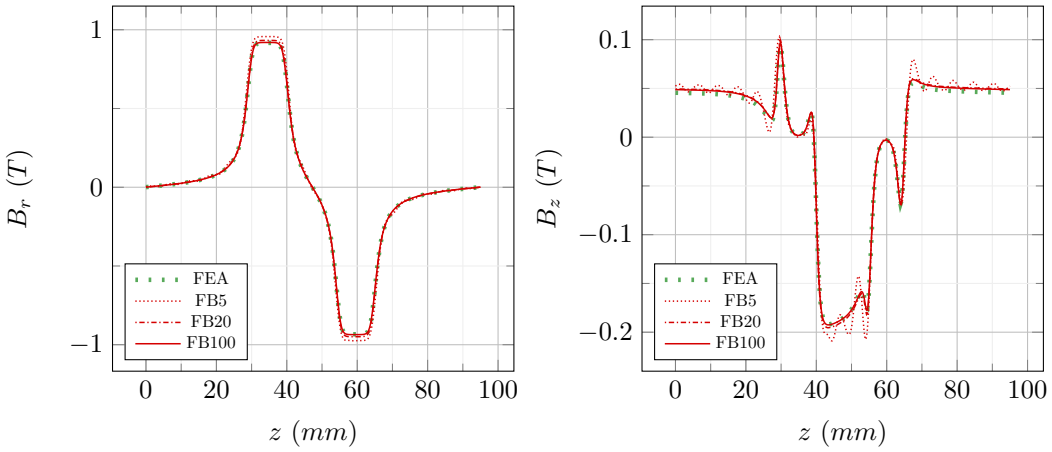

Figure 3.5: Air gap magnetic flux density distributions obtained with the FEA and Fourier model.

Neumann and continuous boundary condition at $r = R_{R,e}$. As explained in appendix A, the compliance of the solution to this kind of boundary condition depends on the number of harmonics that is employed, which explains that more harmonics are required for the convergence of the solution. It is also noticed, in fig. 3.5, that the radial magnetic flux density amplitude tends to be overestimated for a low number of harmonics, and decreases when this number is increased. The impact of this phenomenon is reflected in the values of the global characteristics of the bearing in the next sections.

3.2 Magnetic flux density distribution with eccentricity

The model presented in the previous section computes the magnetic flux density in the bearing for a rotor that is radially perfectly centered with respect to the stator. Despite the position of the rotor is controlled to remain centered, it is required to model the behavior of the magnetic flux density distribution for a rotor incurring an eccentricity to obtain some of its global characteristics. This section proposes a methodology that evaluates this distribution analytically without additional evaluations of the model using a modulation function, as presented in [5] in which the efficiency of the modulation function is demonstrated. The implementation of the modulation function is detailed and validated through a 3D FEA.

3.2.1 Modulation function

The methodology of the modulation function consists in assuming that the air gap magnetic flux density distribution with eccentricity is obtained by multiplying the magnetic flux density distribution of the centered configuration by a function of the azimuthal position θ as well as the eccentricity ϵ to account for the effect of this latter. This function is called the modulation function and is defined in eq. 3.40. The eccentricity of the rotor as well as the convention regarding θ are illustrated in fig. 3.6.

$$\Gamma(\theta, \epsilon) \triangleq \frac{B_r(r, z, \theta)\Big|_{\epsilon \neq 0}}{B_r(r, z)\Big|_{\epsilon = 0}} \tag{3.40}$$

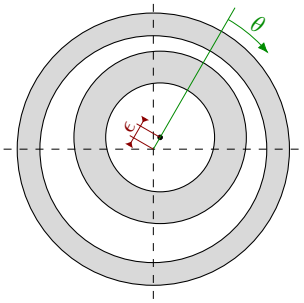

Figure 3.6: Eccentricity of the rotor.

The Γ function is made from two variations of the behavior of the magnetic flux density, both involving the magnetic permeance of the air gap. One of the contribution is the variation of the local permeance of a magnetic flux tube in the air gap. Fig. 3.6 shows that the eccentricity tends to tighten the air gap in the direction of the eccentricity and to make it longer in the opposite direction. As the stator and the rotor are ferromagnetic materials, the magnetic potential difference between these two latter will be the same in the whole air gap, implying a modulation of the magnetic flux density by the length of this air gap. The other contribution regards the global permeance of the air gap that is impacted by the eccentricity, which changes the working point of the permanent magnets. The two contributions are defined in eq. 3.41, illustrated in fig. 3.7 and detailed hereafter.

$$\Gamma(\theta, \epsilon) = \frac{P_{ag}\Big|_{\epsilon \neq 0}}{P_{ag}\Big|_{\epsilon = 0}} \times \frac{dP_{ag}(\theta)\Big|_{\epsilon \neq 0}}{dP_{ag}\Big|_{\epsilon = 0}} \tag{3.41}$$

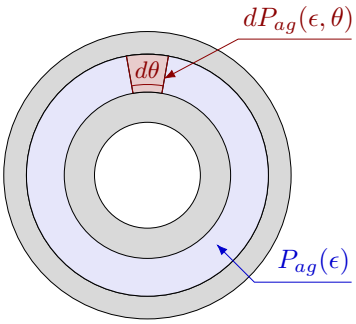

Figure 3.7: Local and global permeance of the air gap.

3.2.2 Air gap flux tube permeance

Assuming a small eccentricity ϵ compared to the internal and external radii of the stator and the rotor $R_{S,i}$ and $R_{R,e}$, it can be written that $e(\theta) = e - \epsilon\cos(\theta)$ where e is the length of the air gap for a centered position of the rotor (i.e. $R_{S,i} - R_{R,e}$). The eccentricity is thus considered to be equivalent to a centered configuration in which the stator has a radius that is a function of θ such that: $R_{S,i}(\theta) = R_{R,e} + e(\theta) = R_{S,i} - \epsilon\cos(\theta)$. By integrating from $R_{R,e}$ to $R_{S,i}(\theta)$ the expression of the reluctance of a local flux tube located at a radius r, with a radial width dr, an angular opening $d\theta$ and an axial length L, the following equation is obtained:

$$dR_{ag}(\theta) = \int_{R_{R,e}}^{R_{S,i}(\theta)} \frac{dr}{\mu_0 r d\theta L} = \frac{1}{\mu_0 d\theta L} \ln\left(\frac{R_{R,e}}{R_{S,i}(\theta)}\right) = \frac{1}{\mu_0 L d\theta} \ln\left(\frac{R_{S,i} - \epsilon\cos(\theta)}{R_{R,e}}\right) \tag{3.42}$$

The local permeance is found by inverting this latter expression. The assumption of small eccentricity allows for a Taylor approximation of the first order of the denominator, such that:

$$dP_{ag}(\theta) \simeq \frac{\mu_0 d\theta L}{\ln\left(\frac{R_{S,i}}{R_{R,e}}\right) - \frac{\epsilon\cos(\theta)}{R_{S,i}}} \tag{3.43}$$

This function is periodic along θ and has a period 2π. As suggested in [5], a development in a Fourier series with two harmonics is made to further simplify this expression:

$$dP_{ag}(\theta) \simeq \frac{\mu_0}{\ln\left(\frac{R_{S,i}}{R_{R,e}}\right)^3} \left(\ln\left(\frac{R_{S,i}}{R_{R,e}}\right)^2 + \left(\frac{\epsilon}{R_{S,i}}\right) \ln\left(\frac{R_{S,i}}{R_{R,e}}\right) \cos(\theta) + \left(\frac{\epsilon}{R_{S,i}}\right)^2 \cos(2\theta)\right) \tag{3.44}$$

The approximated expression of the local permeance contribution of the modulation function is therefore given by:

$$\frac{dP_{ag}(\theta)\Big|_{\epsilon\neq 0}}{dP_{ag}\Big|_{\epsilon=0}} = \left(1 + \frac{\epsilon}{R_{S,i}\ln\left(\frac{R_{S_i}}{R_{R_e}}\right)} cos(\theta) + \left(\frac{\epsilon}{R_{S_i}}\right)^2 \frac{1}{\ln\left(\frac{R_{S_i}}{R_{R_e}}\right)} cos(2\theta)\right) \tag{3.45}$$

3.2.3 Air gap global permeance

Employing the same assumption of small eccentricity, the expression of the global permeance is obtained by integrating eq. 3.44 over θ from 0 to 2π. The resulting expression is given by:

$$P_{ag} = \frac{2\pi\mu_0 L_{I,S}}{\ln(\frac{R_{S,i}}{R_{R,e}})} \tag{3.46}$$

This approximation not being a function of ϵ, the contribution of the global permeance of the air gap to the modulation function is neglected for small eccentricities. The final approximated expression of the modulation function is consequently given by:

$$\Gamma(\theta, \epsilon) = \left(1 + \frac{\epsilon}{R_{S,i}\ln\left(\frac{R_{S_i}}{R_{R_e}}\right)} cos(\theta) + \left(\frac{\epsilon}{R_{S_i}}\right)^2 \frac{1}{\ln\left(\frac{R_{S_i}}{R_{R_e}}\right)} cos(2\theta)\right) \tag{3.47}$$

3.2.4 Comparison with the Finite element analysis

The accuracy of the modulation function is assessed with a 3D FEA simulating the magnetic flux density distribution of an off-centered configuration. The air gap magnetic field is compared to the one obtained with the Fourier model and its modulation function inside and outside the iron poles to assess the validity of the modulation function over the whole period of the model (see fig. 3.8). The modulation function matches the results obtained with the FEA inside the iron pole, but the effect of the eccentricity is overestimated by the modulation function outside the iron pole. The modulation function being used over the whole width of the model in the evaluation of the global characteristics, this overestimation introduces error. The amplitude of the magnetic flux density being smaller where the modulation function is not accurate, the error committed in the evaluation of the global characteristics is not expected to be important after the integration over the whole period of the model.

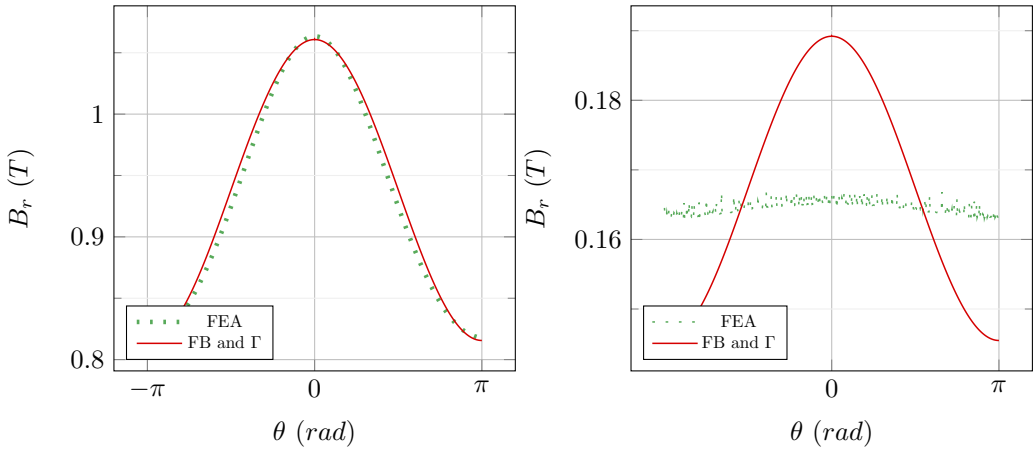

Figure 3.8: Air gap radial magnetic flux density inside (left) and outside (right) of the iron teeth of the bearing for a rotor off-centered of 100 μm. Comparison between FEA and the modulation function.

3.3 Global values

The previous sections present a tool capable of modelling locally the bearing and its magnetic flux density distribution. This section explains how the global characteristics of the bearing are extracted from this local model. The three position (radial, axial and tilt) stiffnesses presented in section 2.2 are first developed followed by the current stiffness as well as the electrical resistance of the windings.

3.3.1 Axial displacement stiffness

The Fourier model including a possibility to move the rotor axially and to compute the exact magnetic flux density of such a configuration, the characteristic linking the axial force and the axial displacement is directly obtained from the model. The value of the axial force is obtained by integration of the Maxwell's stress tensor (MST) over a closed surface The MST is defined in the coordinate system of the Fourier based model in eq. 3.48 in which a simplification is performed by removing the azimuthal component of the magnetic field.

$$\underset{\sim}{\sigma} = \frac{1}{\mu_0}\begin{pmatrix} \frac{1}{2}B_r^2 & B_rB_\theta & B_rB_z \\ B_rB_\theta & \frac{1}{2}B_\theta^2 & B_\theta B_z \\ B_rB_z & B_\theta B_z & \frac{1}{2}B_z^2 \end{pmatrix} = \frac{1}{\mu_0}\begin{pmatrix} \frac{1}{2}B_r^2 & 0 & B_rB_z \\ 0 & 0 & 0 \\ B_rB_z & 0 & \frac{1}{2}B_z^2 \end{pmatrix} \tag{3.48}$$

The chosen surface of integration is a cylinder aligned with the rotor and wrapping this later in the air gap, as represented in fig. 3.9. The radius of this cylinder is the average of $R_{S,i}$ and $R_{R,e}$ and its length is the period of repetition of the subdomain model so that the contributions of the MST in the two lateral surfaces (the disks) cancel each other. The normal vector associated to this cylinder is radial, such that $\vec{n} = \hat{e_r}$. The corresponding force per unit of area on the surface of integration is thus the first column of the MST ($\underset{\sim}{\sigma} \cdot \vec{n}$). which is made of a radial and an axial component. After integration, the radial component cancels itself due to the axisymmetry of B_r. The remaining component of the detent force is axial and given by:

$$F_{mag,z} = 2\pi\frac{R_{MST}}{\mu_0}\int_0^{2\tau_3} B_r(R_{MST}, z)B_z(R_{MST}, z)dz \tag{3.49}$$

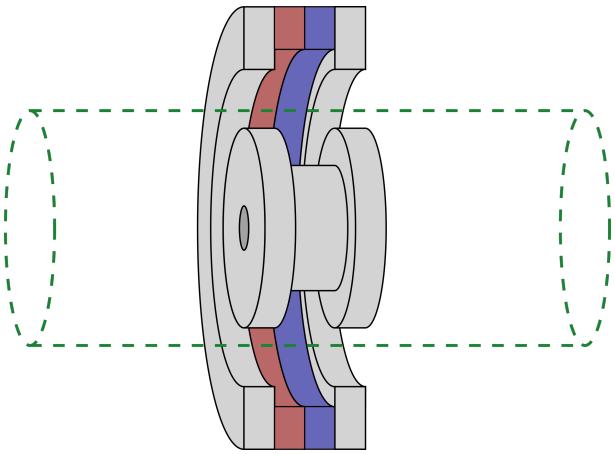

Figure 3.9: Illustration of the closed surface used for the integration of the MST.

The axial force - axial displacement characteristic obtained by the Fourier model has been validated through a 2D finite element analysis. The characteristics obtained with the FEA and the Fourier based model with different numbers of harmonics are presented in fig. 3.10. The average error committed with the Fourier models are also given in table 3.4 considering the FEA as a reference. As expected, the Fourier model tends to match the FEA as the number of harmonics is increased, which validates the computation of the axial detent force. For a given configuration of the bearing, the value of the axial force given by the Fourier based model decreases in amplitude if more harmonics are employed which is explained by the overestimation of the radial magnetic flux density amplitude for low number of harmonics (section 3.1.4).

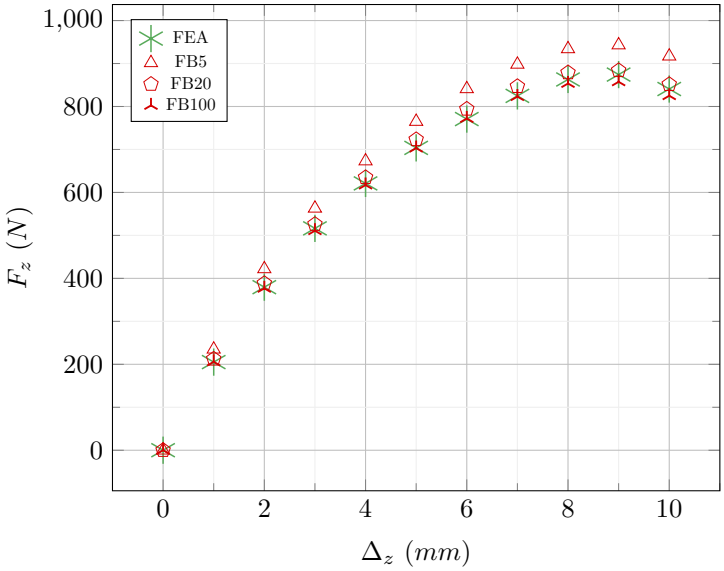

Figure 3.10: Axial displacement - Axial force characteristics. Comparison between FB and FEA.

Table 3.4: Average error commited by the Fourier model over the axial force.

	FB5	**FB20**	**FB100**
Relative error [%]	9.59	2.27	0.80

3.3.2 Radial displacement stiffness

Unlike for the axial stiffness, the radial force - radial displacement cannot be obtained directly from the model as it does not allow evaluating the exact magnetic flux density for such a configuration. The characteristic is thus approximated by the radial stiffness by the use of the modulation function presented in section 3.2. The value of the stiffness is, similarly to the modulation function, only valid for small eccentricities. The radial stiffness is defined by:

$$k_\epsilon \triangleq \frac{\partial F_r}{\partial \epsilon} \tag{3.50}$$

The radial force F_r is obtained by integrating the MST over the same integration surface employed for the axial force characteristic (fig. 3.9). The first column of the MST is thus also considered, in which the axial component of the force per unit of area is not of interest. The axisymmetry of the bearing not being conserved if incurring an eccentricity, the radial component of this force per unit of area vector allows obtaining the resulting radial force acting on the rotor after integration.

$$F_r = \frac{1}{\mu_0}\int_0^{2\tau_3}\int_0^{2\pi} \frac{B_r^2(R_{MST}, z)\Gamma(\theta,\epsilon)^2}{2} cos(\theta) R_{MST} d\theta dz \tag{3.51}$$

in which $\Gamma(\theta, \epsilon)$ is the modulation function. The radial force - radial position characteristic obtained with a 3D FEA is compared to the values of the radial stiffness obtained with the Fourier model for different numbers of harmonics (fig. 3.11). The radial stiffness computed with the Fourier model approximates accurately the characteristic obtained with the FEA around the centered. As it is observed with the axial stiffness, the radial stiffness is overestimated for small number of harmonics, which is also explained by the overestimation of the radial magnetic flux density amplitude by the model in these conditions.

3.3.3 Tilt stiffness

The tilt stiffness links the tilt degree of freedom of the rotor to the detent torque acting on it when incurring tilt. Similarly to what is performed for the radial stiffness, the Torque - tilt characteristic is approximated by a stiffness since the model does not allow evaluating the exact magnetic flux density in the bearing in such a configuration. The tilt stiffness is defined as:

$$k_\Psi \triangleq \frac{\partial T_\Psi}{\partial \Psi} \tag{3.52}$$

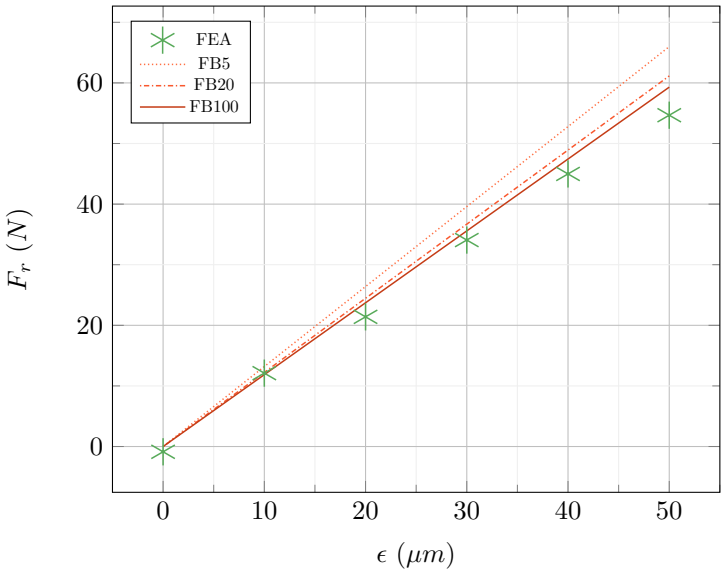

Figure 3.11: Radial displacement - Radial force characteristic of the bearing. Comparison between 3D FEA and FB model.

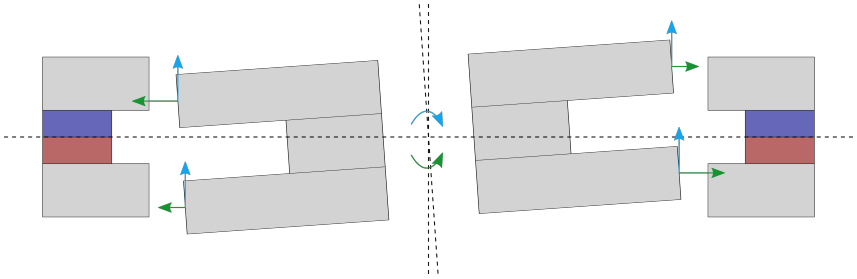

Figure 3.12: Illustration of the radial (green) and axial (blue) local forces contributing to the global tilt stiffness acting on the rotor. The axial contribution is stabilizing, unlike the radial contribution.

where Ψ is the angle of rotation of the rotor around its center of mass. It is considered that the center of mass of the rotor is radially centered and that the axis of rotation of the rotor goes through this center of mass.

The resulting torque on the rotor originates from two contributions. One of the contribution is axial and due to the azimuthal dependence of the axial local forces acting on the rotor, if this latter incurs tilt. This contribution is stabilizing, as it generates a resulting torque opposite to the tilt. The other contribution is radial and due to the disequilibrium of the local radial forces in the air gap if the rotor incurs tilt. This contribution is destabilizing, as it generates a resulting torque in the same direction as the tilt motion. The tilt degree of freedom of the rotor is stable as long as the axial contribution is greater than the radial one. The two contributions are illustrated in fig. 3.12 and evaluated separately before being summed to evaluate the global tilt stiffness.

Axial forces contribution

The axial contribution comes from the local axial displacement of the edges of the rotor that becomes a function of θ if the rotor presents a tilt angle Ψ. This local axial displacement, linked with the axial stiffness, leads to varying local axial forces, resulting in a torque. The axial deflection with respect to the axial equilibrium point of the rotor of a point located in (r, θ) on the rotor undergoing a small tilt angle Ψ is given by:

$$\delta(r, \theta) = \Psi r \cos(\theta) \tag{3.53}$$

As the iron rotor teeth are the part of the rotor that interact the most with the magnetic flied, it is assumed that the axial position stiffness is uniformly distributed over these teeth. An equivalent axial stiffness per unit of surface is defined and obtained by dividing the axial stiffness k_z (obtained by

performing a linear approximation of the characteristic presented in section 3.3.1) by the surface of the iron teeth (i.e. $\pi(R_{R,e}^2 - R_{R,i}^2)$). The local force generated by a local element of integration located in the rotor at $(r,\, \theta)$ is consequently:

$$dF = \delta(r,\theta)\frac{k_z}{\pi(R_{R,e}^2 - R_{R,i}^2)} r dr d\theta = \frac{\Psi r^2 \cos(\theta) dr d\theta}{\pi(R_{R,e}^2 - R_{R,i}^2)} \tag{3.54}$$

This local force, multiplied by its lever arm, is integrated over the surface of the iron teeth leading to the resulting torque:

$$T_{\Psi,z} = \int_0^{2\pi} \int_{R_{R,i}}^{R_{R,e}} r\cos(\theta) dF = \int_0^{2\pi} \int_{R_{R,i}}^{R_{R,e}} \frac{\Psi r^3 \cos(\theta)^2}{\pi(R_{R,e}^2 - R_{R,i}^2)} dr d\theta \tag{3.55}$$

from which the axial contribution of the tilt stiffness is obtained by derivation, with respect to Ψ:

$$k_{\Psi,z} = \frac{k_z}{4}\frac{R_{R,e}^4 - R_{R,i}^4}{R_{R,e}^2 - R_{R,i}^2} \tag{3.56}$$

Radial forces contribution

The evaluation of the radial contribution of the tilt stiffness is obtained similarly to the axial contribution. If undergoing a tilt angle, the position of a point located on the edge of the iron tooth becomes a function of z. This local radial displacement, linked to the radial stiffness, gives rise to unbalanced radial forces resulting in a torque on the rotor. These local radial displacements can be assimilated to a global eccentricity that becomes a function of z. If z_c is the axial position of the center of mass of the rotor in the frame of the model, the z-dependant eccentricity is given by:

$$\epsilon(z) = \Psi(z - zc) \tag{3.57}$$

It is assumed that the radial stiffness is uniformly distributed over the outer edges of the rotor, which allows to define an equivalent radial stiffness per unit of area by dividing the radial stiffness by the area of these edges. The local force acting on a point located in (r, z, θ) is thus given by:

$$dF = \frac{\Psi(z - z_c)k_\epsilon d\theta dz}{4\pi L_{I,R}} \tag{3.58}$$

The resulting torque is obtained by integrating the local force multiplied by its lever arm over the edges of the rotor iron teeth: The radial contribution of the tilt stiffness is thus given by:

$$k_{\Psi,r} = \frac{k_\epsilon}{6L_{I,R}}\left((z_1 - zc)^3 + (z_2 - z_c)^3 + (z_3 - z_c)^3 - (z_4 - z_c)^3\right) \tag{3.59}$$

where $z_1 = z_c - L_B/2 - L_{I,R}$, $z_2 = z_c - L_B/2$, $z_3 = z_c + L_B/2$ and $z_4 = z_c + L_B/2 + L_{I,R}$.

The tilt stiffnesses obtained with the Fourier model for different numbers of harmonics are compared to the results obtained with the 3D FEA in fig. 3.13. The tilt stiffness given by the Fourier based model tends to match the FEA analysis and the accuracy is enhanced for higher number of harmonics. The machine used for the validation of the model is stable in tilt, as the tilt stiffness is negative.

3.3.4 Current stiffness

The current stiffness is the value that links the current flowing through the windings to the resulting force that is applied to a radially centered rotor. Considering one radial degree of freedom for the rotor (the eccentricity ϵ), the equation of the electromagnetic force is obtained by derivation of the co-magnetic energy with respect to the eccentricity ϵ:

$$F_r = \frac{\partial W_{cmag,0}(\epsilon)}{\partial \epsilon} + \sum_{k=1}^{n} \frac{\partial \Phi_{k,0}(\epsilon)}{\partial \epsilon} i_k + \frac{1}{2}\sum_{k=1}^{n}\sum_{j=1}^{n} \frac{\partial L_{k,j}(\epsilon)}{\epsilon} i_k i_j \tag{3.60}$$

Where F_r is the resulting radial force, $W_{cmag,0}$ is the co-magnetic energy present in the bearing if no currents flow in the windings, $\Phi_{k,0}$ is the magnetic flux circled by the windings of phase k if no current flows in the windings, $L_{k,j}$ is the inductance coefficient linking the phase k with the phase j and i_k is the current flowing through the phase k. The first term represents the detent force, which is null for a

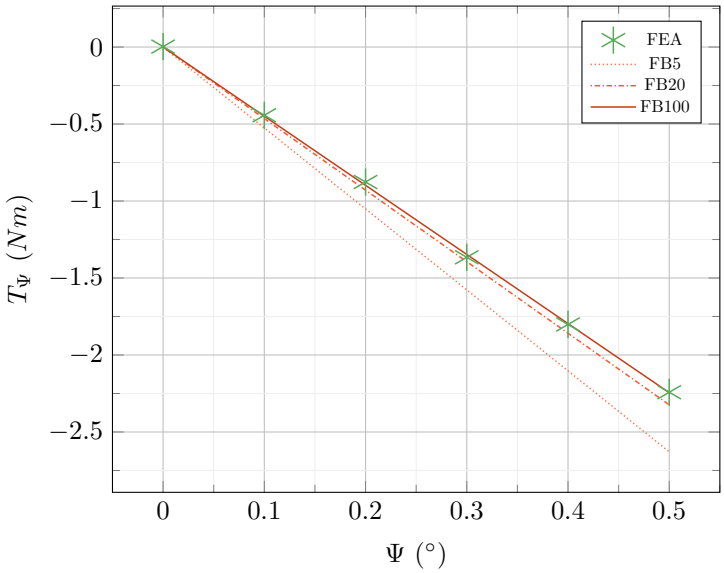

Figure 3.13: Tilt angle - Tilt torque characteristic of the bearing. Comparison between 3D FEA and FB model.

perfectly centered rotor. The last term of the equation is the reluctant force, due to the variation of the inductance coefficients of the windings with respect to the eccentricity and null for a perfectly centered rotor, the inductance coefficients of the windings being symmetrical around the centered position. The useful term of the equation corresponds thus to the electrodynamic force originating from the interaction between the magnetic flux generated by the permanent magnets and the current flowing through the windings. The current is consequently given by:

$$k_i = \frac{\partial \Phi}{\partial \epsilon} \tag{3.61}$$

where Φ is the total magnetic flux circled by the coils dedicated to one axis of actuation. Here, ϵ is the eccentricity in the direction aligned with the axis of actuation considered.

The magnetic flux circled by the windings is obtained by integrating the magnetic flux density obtained with the Fourier model and the modulation function over the four coils constituting a phase as in the following equation:

$$\Phi = \sum_{k=1}^{4} \int_{R_{W,i}}^{R_{S,i}} \int_{\Theta_{W,i,k}}^{\Theta_{W,e,k}} d\Phi_k \tag{3.62}$$

The term $d\Phi_k$ corresponds to the flux circled by a winding of infinitesimal section inside the real winding, as illustrated in fig. 3.14. The section of this coil is $dS = rdrd\theta$ and contains dSN_W/S_W turns, the go conductors are located in (r, θ) and the back ones at $(r, -\theta)$. The flux caught by such a winding is given by:

$$d\Phi = \frac{N_W}{S_W} dS \int_{-\theta}^{\theta} \int_{z1(\theta)}^{z2(\theta)} Br(r, z)\Gamma(\theta', \epsilon) r d\theta' dz \tag{3.63}$$

where z_1 and z_2 are the axial coordinates of the beginning and the end of the coil in the coordinate system of the model.

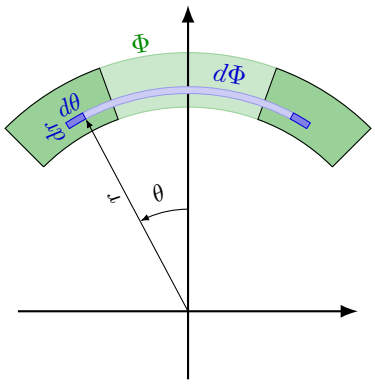

Figure 3.14: Illustration of the coil of infinitesimal section for the integration.

The stiffness given by the Fourier model is compared to the results of a FEA in table 3.5 for different numbers of harmonics. Even though the Fourier model tends to converge towards the FEA for an increased number of harmonics, the error made remains above 13 % of the value obtained with the finite element model. This error originates from the overestimation of the effect of the eccentricity over the magnetic flux density distribution outside an iron pole in the air gap (section 3.2.4). As the coils circle magnetic flux outside the iron teeth, this contribution to the current stiffness is also overestimated. The reason for which the radial stiffness is impacted to a lesser extent by this overestimation is that the square of the magnetic flux density is integrated for its evaluation, which reinforces the difference of magnitude of the radial magnetic flux density outside and inside the iron poles.

Table 3.5: Current stiffnesses obtained with different numbers of harmonics and the FEA.

	FB5	**FB20**	**FB100**	**FEA**
k_i $[N/A]$	15.771	15.187	14.9519	13.126
Relative error [%]	20.2	15.7	13.89	-

3.3.5 Windings electrical resistance

Although the electrical resistance of the windings is not a magnetic global value, this value remains useful to evaluate the performance of the bearing. The resistance of one phase of winding is evaluated similarly to what is done in [3], starting from the classical expression of the resistance:

$$R = \frac{\rho_{Cu} l}{A} \tag{3.64}$$

in which R is the resistance, ρ_{Cu} is the electrical resistivity of the material and l and A are namely the length and the cross-section area of the conductor.

The length of conductor is approximated by the average length of one spire L_{loop} multiplied by the number of spires in each coil N_W multiplied by the number of coils per phase, four. Considering the geometry of the coils, the average length of one loop is given by:

$$L_{loop} = L_{W,i} + L_{W,e} + \frac{(R_{S,i} + R_{W,i})}{2}\Big(\frac{\pi}{2}(\theta_{W,e} - \theta_{W,i}) + 2\theta_{W,i}\Big) \tag{3.65}$$

The cross-section of the cable used to form the windings is evaluated, considering the available space in one "slot" dedicated to the windings, the number of turns as well as the fill factor modelling the empty space around the conductors in the slot. The surface of one cable is consequently given by:

$$S_c = \eta \frac{S_{coil}}{N_W} = \eta \frac{(\theta_{W_e} - \theta_{W,i})(R_{S,i}^2 - R_{W,i}^2)}{4N_W} \tag{3.66}$$

leading to the expression of the electrical resistance of one phase of winding:

$$R = \frac{16 N_W^2 \rho_{Cu} L_{Loop}}{\eta(\theta_{W_e} - \theta_{W,i})(R_{S,i}^2 - R_{W,i}^2)} \tag{3.67}$$

3.4 Analyzis

This section analyzes the results provided by the Fourier model to draw conclusions about the behavior of the model and of the bearing. The impact of the periodization of the bearing in the Fourier model is first assesses. The evolution of the position and current stiffnesses with respect to the axial position of the rotor are then presented and analyzed.

3.4.1 Impact of the periodization

The impact of the periodization of the model is assessed by adjusting the length separating these repetitions L_{ext}. A model in which the periodization are separated by a long distance is more faithful to the reality, but requires more harmonics for an accurate evaluation of the solution. Models in which L_{ext} is smaller require fewer harmonics, but might not give relevant results as the periodization impacts these latter. Fig. 3.15 shows the axial detent force evaluated with the Fourier model with 20 harmonics in region II as a function of L_{ext}. The value of the axial magnetic force tends to oscillate as the value of L_{ext} is modified, but a convergence is roughly reached once the value of 60 mm is reached, which corresponds to 170 % of the axial width of the stator. Below this value, the periodization of the bearing alters the results given by the model. A similar observation is made for the other global values, as they originate from the same magnetic flux density distribution.

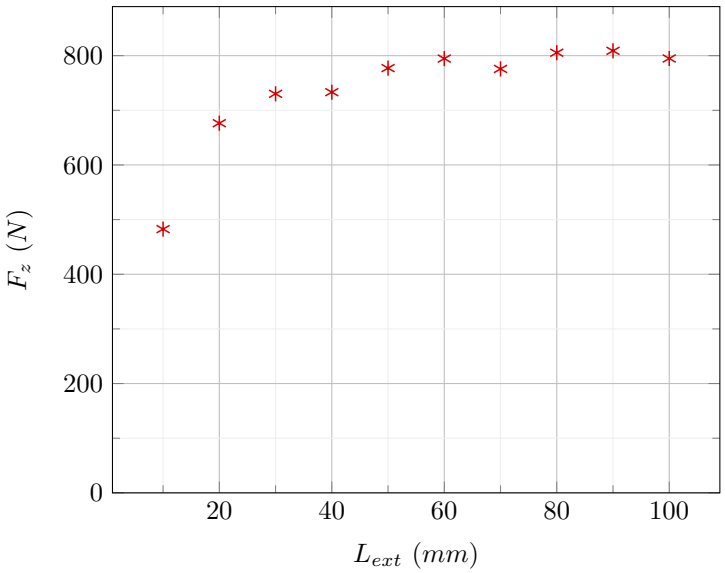

Figure 3.15: Axial magnetic force obtained with the Fourier model with 20 harmonics in region II as a function of L_{ext}.

Impact of the axial position of the rotor

As explained in chapter 2, the axial position of the rotor is expected to vary once the bearing is in operation. The axial position of the rotor Δ_z impacting the magnetic flux density distribution, it is interesting to assess how the global characteristics of the bearing vary with this position. Fig. 3.16 shows the radial position stiffness k_ϵ as a function of the axial displacement Δ_z. This stiffness remains constant as long as the axial displacement is kept smaller than 1 mm and is lowered by 16.7% for an axial displacement of 5 mm. Compared to fig. 3.10, this roughly corresponds to the linear portion of the axial force - axial displacement characteristic.

A similar observation is made for the current stiffness as it originates from the same phenomena as the radial position stiffness (fig. 3.17).

The tilt stiffness as a function of the axial displacement is provided in 3.18. It is observed that k_Ψ strongly depends on the axial position of the rotor. This observation finds its explanation considering that the lever arm of the radial detent force increases with Δ_z. If Δ_z increases, the lever arm of the radial local forces increases as well. The tilt stiffness being the sum of the axial contribution (negative) and radial contribution (positive), the resulting it increases similarly to an affine function.

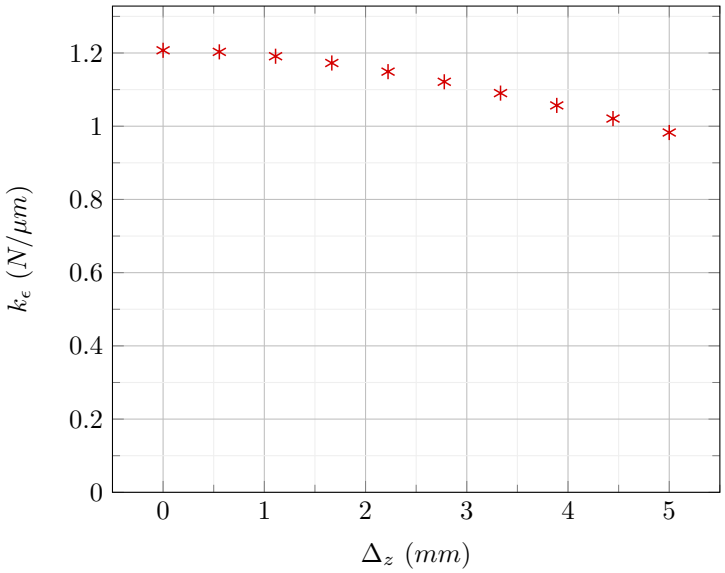

Figure 3.16: Radial position stiffness as a function of the axial displacement of the rotor Δ_z.

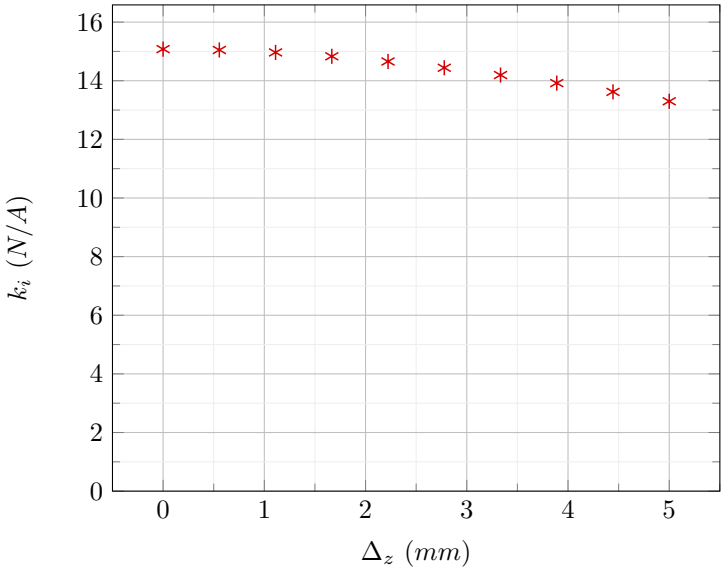

Figure 3.17: Current stiffness as a function of the axial displacement of the rotor Δ_z.

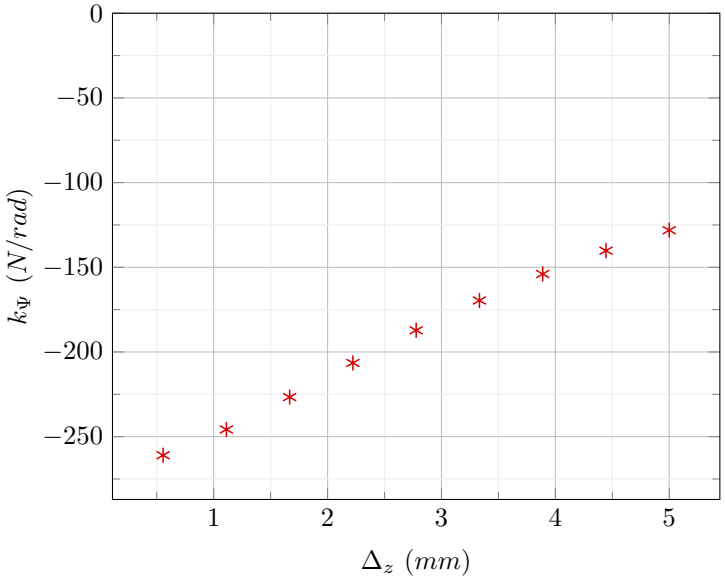

Figure 3.18: Tilt stiffness as a function of the axial displacement of the rotor Δ_z.

CHAPTER 4

MODELING THE FLYWHEEL

The dimensions of the FESS under development are determined by an optimization routine that aims at optimizing the performance of the system as a flywheel. This section details the model that allows for an evaluation of these performances and other global characteristics related to the FESS that are required in the optimization routine. These models are meant to be executed after the magnetic model of the bearing (see chapter 3) and use the global characteristics obtained with this model. The evaluation of the axial equilibrium point of the rotor is first presented, as this equilibrium point influences the value of the other global characteristics of the bearing. The mechanical model, characterizing the maximum speed of the rotor, is then established and the evaluation of the self-discharge rate of the system, taking into account the aerodynamic friction as well as the electrical consumption of the bearing, is finally presented.

4.1 Axial equilibrium point

The axial equilibrium point of the bearing is the axial position that the rotor reaches when it is incurs gravity. This position is such that the gravitational force acting downward on the rotor is compensated by the axial magnetic detent force that pulls the rotor upward. It is required to find the value of Δ_z such that $F_z(\Delta_z) = m_{rotor}g$, where m_{rotor} is the mass of the rotor and g is the gravity constant ($9.81\ m/s^2$).

This equilibrium point is obtained through a dichotomic method that iterates on the value of Δ_z until the condition is satisfied within a given tolerance. An initial value, $\Delta_{z,0}$ is arbitrary chosen as a fraction of the length of the permanent magnets L_{PM}. For this axial position, the magnetic model is evaluated and the magnetic detent force $F_{mag,0}$ is obtained and an axial equivalent stiffness $k_{z,0}$ is estimated by dividing $F_{mag,0}$ by $\Delta_z, 0$. From this axial stiffness, the axial equilibrium point $\Delta_{z,1}$ is estimated such that $k_{z,0}\Delta_{z,1} = m_{rotor}g$. The magnetic model of the bearing is thus evaluated with $\Delta_{z,1}$ and the same procedure is applied until the axial equilibrium point $\Delta_{z,n}$ is such that:

$$|F_{mag}(\Delta_{z,1}) - m_{rotor}g| < tol \tag{4.1}$$

where *tol* is the numerical tolerance. The dichotomic method is illustrated in fig. 4.1. The convergence of the method is ensured by the monotonicity of the axial force - axial displacement and would not converge if the initial axial position was chosen too far beyond the equilibrium point where the rotor is unlocked from the stator and does not interact with it anymore.

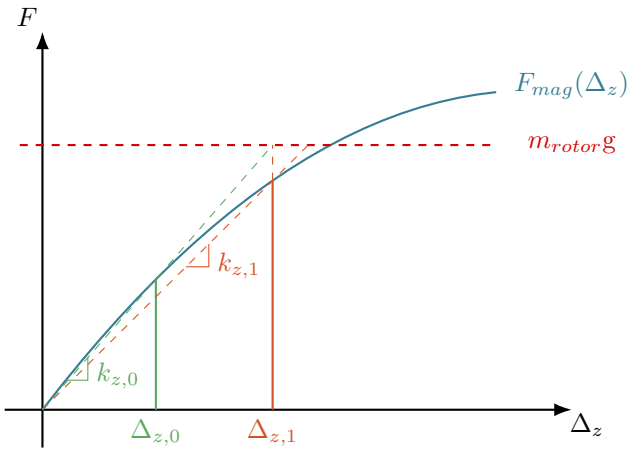

Figure 4.1: Illustration of the working principle and the convergence of the dichotomic method employed to obtain the axial equilibrium point of the rotor.

After the first iteration, the model compares the estimated axial equilibrium position with the total width of the rotor to stop the iteration process if the machine does not have a sufficient axial position stiffness to stand the weight of its rotor. This feature is employed in the optimization routine.

4.2 Speed limit: mechanical stress in the rotor

This section explains how the speed of the rotor is mechanically limited. When the flywheel rotates around its center of mass, mechanical stress appear inside the material due to the local centripetal acceleration. The mechanical stress increases with the speed of the rotor and, if not properly designed, gives rise to cracks leading to the failure. A limit upon the speed at which the rotor is allowed to rotate is required to avoid this problem, which imitates the maximum energy that can be stored in the FESS. The static and fatigue design leading to the evaluation of this limit is presented in this section.

4.2.1 Static design

The rotational speed of the rotor, Ω, is considered constant in the first place. To evaluate the mechanical stress in the rotor, this latter is considered as a hollow cylinder of inner radius $R_{R,d}$, outer radius $R_{R,e}$ and a height $2L_{I,S} + L_B$. This assumption adds matter to the real rotor and lead to an overestimation of the actual mechanical stress in the real rotor, which acts as a safety factor on the speed limit of the rotor. It is considered that the upper and lower surfaces of the cylinder deform themselves freely and that the rotation of the rotor only results in radial (σ_r) and azimuthal (σ_θ) stresses. The appendix B, inspired by [28], explains how to evaluate analytically the mechanical stress in a hollow cylinder rotating at constant speed. The resulting radial and azimuthal stresses are given by:

$$\sigma_r(r) = \frac{\rho\Omega^2}{8}\frac{3-2\nu}{1-\nu}\left(R_{R,e}^2 + R_{R,d}^2 - \frac{R_{R,e}^2 R_{R,d}^2}{r^2} - r^2\right) \tag{4.2}$$

$$\sigma_\theta(r) = \frac{\rho\Omega^2}{8}\frac{3-2\nu}{1-\nu}\left(R_{R,e}^2 + R_{R,d}^2 + \frac{R_{R,e}^2 R_{R,d}^2}{r^2} - \frac{(1+2\nu)}{3-2\nu}r^2\right) \tag{4.3}$$

where ν is the Poisson coefficient of the material and ρ is its density. The rotor being made of ductile materials, the equivalent Von Mises stress is compared to the yield stress of the material, σ_y to determine the speed limit of the rotor. The Von Mises stress, for a planar strain, is given by:

$$\sigma_{VM}(r) = \sqrt{\sigma_r^2 + \sigma_\theta^2 - \sigma_r\sigma_\theta} \tag{4.4}$$

The static condition to avoid a failure of the rotor is:

$$max(\sigma_{VM}(r)) < \frac{\sigma_y}{k_s} \tag{4.5}$$

where k_s is the safety factor, set to two in this application, that allows for taking into account the uncertainty over the materials, the load or the stress concentrations that appear because of the real shape of the rotor.

The Ω^2 present in the expression of the stresses is taken out of the square root, giving the following expression for the maximum speed that the rotor can reach in static:

$$\Omega_{max} = \sqrt{\frac{2\sigma_y}{k_s \times max(\sigma_{VM}(r)/\Omega^2)}} \tag{4.6}$$

4.2.2 Fatigue design

The assumption over the constant speed of the rotor is lifted in this section. Throughout its service, a flywheel undergoes cycles of charge and discharge in which the speed first increases to a given level and decreases until the flywheel is empty. The load introduced in the static design is thus not constant but cyclic. The cyclic load tends to give rise to cracks appearing in the material even though the rotor is well-designed to withstand the static load. A fatigue design must be applied to avoid the fatigue failure of the materials. The cyclability of the FESS being one of its main advantages over classical ESS, an infinite number of cycles is considered for the fatigue design. The methodology applied to design the rotor in fatigue is inspired by [27].

The endurance limit of the rotor is given by: $S_n = S'_n C_L C_G C_S C_T C_R$. Where S_n is the endurance limit in MPa, S'_n is the R.R.Moore's endurance limit in MPa, C_L is the load factor, C_G is the gradient factor, C_S is the surface finish factor, C_T is the temperature factor and C_R is the reliability factor. The values of these factors chosen for this application are given in table 4.1 considering a 10^6 cycles before failure which is equivalent to an infinite number of cycles before failure.

Table 4.1: Values of the factors used for fatigue design.

Factor	C_L	C_G	C_S	C_T	C_R
Values	1.0	1.0	0.6	1.0	0.753

The mean value (σ_m) and the alternating value (σ_a) of stress level are required for the fatigue design. It is considered that the load applied on the rotor varies between 0 and the maximum value σ_{VM} obtained in the static design, which corresponds to a situation in which the flywheel is fully charged and discharged at each cycle, and is the worst case for the fatigue design. The values of σ_m and σ_a are thus equal to the half of the maximum value of stress that can be achieved.

A constant-life fatigue diagram is built in fig. 4.2. The rotor withstands the cyclic load if the operating point, illustrated on the graph, that moves along the Load line as Ω is increased, remains in the green area, below the fatigue and static limit lines. The line on which the operating point moves follows the equation $\sigma_a(\sigma_m) = \sigma_m$, the static and fatigue limit lines are expressed by: $\sigma_a(\sigma_m) = \sigma_y - \sigma_m$ and $\sigma_a(\sigma_m) = S_n - \sigma_m \frac{S_n}{S_u}$, respectively. The intersection between the load and fatigue lines occurs at $\sigma_m = Sn - \sigma_m \frac{S_n}{S_u}$ and the intersection between the load and static line occurs at $\sigma_m = \sigma_y - \sigma_m$. The two solutions of these equations are given by eq. 4.7. The minimal value between these two solutions is consequently chosen for the fatigue design ($\sigma_{m,min}$). The maximum rotational speed of the rotor, that allows it to stand a cyclic load, is consequently such that $\sigma_m(\Omega) = \sigma_{m,max}$.

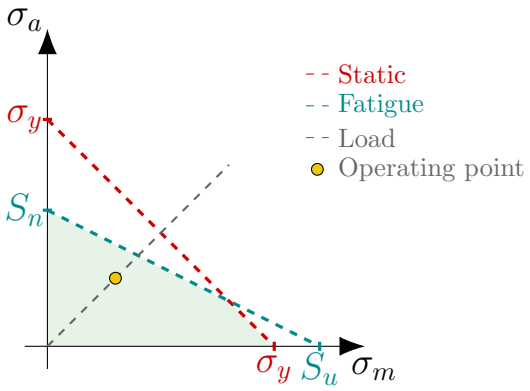

Figure 4.2: Constant-life fatigue diagram: the operating point must remain within the green area.

$$\begin{cases} \sigma_m \leq \frac{S_n}{1+S_n/S_u} \\ \sigma_m \leq \sigma_y/2 \end{cases} \tag{4.7}$$

4.3 Self-discharge time

As explained in section 1.1, the self-discharge of the FESS is a critical performance as it is the main disadvantage compared to other energy storage technologies such as Lithium-ion batteries. The SHH-AMB aiming at reducing the losses in the bearings, it is required to evaluate the duration in which the FESS discharges itself. The self-discharge time of the FESS under study is defined by the time required for the FESS to dissipate 50 % of the energy that was stored initially, if no power is injected or extracted from the energy storage system. It is considered, during this test, that the power consumption of the magnetic bearing is extracted from the flywheel such that no external power supply is connected to the device. As the iron losses occurring in the bearing are suppressed by the use of SHH-AMB, two kinds of losses give rise to the discharge of the flywheel: the power consumption of the magnetic bearing and the aerodynamic friction acting on the rotor in rotation. This section explains how these two contributions are estimated and what is their impact on the self-discharge time of the flywheel.

4.3.1 Conservation of the energy

The evaluation of the self-discharge time of the FESS requires the knowledge of the time evolution of the energy stored in the flywheel that is obtained by deriving the law of conservation of the energy applied to the rotor. The time variation of the kinetic energy stored inside the flywheel is equal to the power losses that it incurs. Considering the expression of the kinetic energy of rotation of a rotating mass, the law of conservation of energy for the flywheel is given by:

$$\frac{dE_k(t)}{dt} = \frac{d}{dt}\left(\frac{I_z\Omega(t)^2}{2}\right) = I_z\Omega(t)\frac{d\Omega(t)}{dt} = P_{Joule} + P_{Aero}(\Omega(t)) \tag{4.8}$$

where E_k is the kinetic energy of rotation of the rotor, I_z is its inertia along its principal axis of rotation, Ω is its rotation speed, and P_{Joule} and P_{Aero} are namely the Joule losses and the aerodynamic losses occurring within the system rotor and are negative. This differential equation is integrated, starting from an initial kinetic energy $E_{k,0}$, until it reaches the half of $E_{k,0}$ giving the self-discharge time of the flywheel.

4.3.2 Joule losses

The Joule losses come from the current flowing through the windings of the SHH-AMB, required to control the rotor position. Given a control current i_c, the Joule losses are given by:

$$P_{Joule} = Ri_c^2 \tag{4.9}$$

where R is the resistance of one phase of the windings of the bearing (section 3.3.5).

The control current is determined by the disturbances acting on the rotor, as a not disturbed rotor does not require current to remain in a central position. Among the disturbances that the rotor incurs, it is assumed the one coming from the not perfectly balanced rotor is the most critical. Indeed, to every manufactured rotating part constituting a mechanical system, is associated a balance grade G in accordance with the ISO 21940 standard. The G grade of a part refers to the radial distance Δ_ϵ between the geometrical center of the part and its actual center of mass, as depicted in fig. 4.3. A well-balanced part has a small G and implies a small distance between the two centers. Typical values of G grades are given in [44]. A grade of 6.3 for the FESS is advised but, this grade being a choice left to the manufacturer, a value of 2.5 is chosen to improve the performances of the bearing while remaining within a realistic value, typically used for electrical motors and generators.

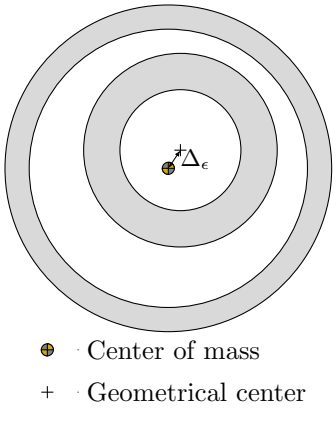

Figure 4.3: The rotor and its unbalanced center of mass.

The relation linking Δ_ϵ to the G grade is given by:

$$G = \Omega_0\Delta_\epsilon \tag{4.10}$$

where Ω_0 is the operational rotation speed of the rotating mass. In the case of the FESS under study, the operational speed is considered to be the speed at which the kinetic energy of the flywheel is equal to $E_{k,0}$.

The control of the rotor is such that it rotates around its principal axis of inertia (i.e. around the center of mass) and presents a constant eccentricity Δ_ϵ once it is in rotation. This eccentricity, through the radial position stiffness k_ϵ, gives rise to a radial detent forces that needs to be compensated by the control currents of the axis of actuation. The current required to compensate the radial detent force due to the eccentricity if this latter is aligned with the concerned axis of actuation is given by:

$$i_c = \frac{k_\epsilon \Delta_\epsilon}{k_i} \tag{4.11}$$

Due to the rotation of the rotor, the control current that compensates this eccentricity is an alternative current oscillating between this value and its opposite at a frequency Ω. The RMS value of this control current and the Joule losses that it generates when flowing through the two phases of windings is given by:

$$i_{c,RMS} = \frac{k_\epsilon \Delta_\epsilon}{k_i \sqrt{2}} \iff P_{Joule} = R_W \frac{k_\epsilon^2 {\Delta_\epsilon}^2}{k_i^2} \tag{4.12}$$

The value of the Joule losses does not vary with time or the rotation speed and is constant during the whole discharge of the FESS.

4.3.3 Aerodynamic friction

An accurate evaluation of the friction losses occurring within the bearing requires complex numerical methods such as FEA to be performed. These models are not compatible with the optimization routine and would slow down the characterization of the system as a flywheel and would make the quick evaluation of the magnetic properties of the bearing useless. The problem fluid mechanics problem is thus split into several simple problems that can be approximated analytically.

Fig. 4.4 illustrates the three origins of aerodynamic friction into which the complex problem is decomposed. The red area represents the friction occurring in the air gap. The problem is assimilated to two cylindrical walls separated by air, one of which rotates at a rotational speed of Ω. The green area represents the friction occurring between the PM ring and the inner part of the rotor. The fluid mechanics problem in this part is approximated similarly to the one in the red area. The orange area represents the friction occurring on the upper and lower edges of the rotor, where a boundary layer problem is considered.

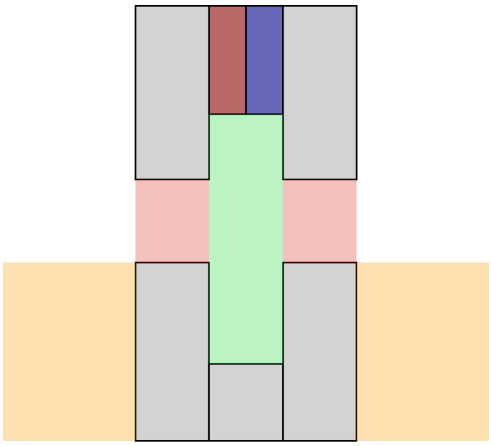

Figure 4.4: Illustration of the different origins of aerodynamic friction occurring on the rotor.

Air gap aerodynamic friction

Similarly to [45], an incompressible Couette flow is considered within the air gap. It assumed that this flow is turbulent as the flywheel is meant to rotate at high speed. The shear stress applied onto the rotor surface τ_{wall} due to such a flow, is given by:

$$\tau_{wall} = \frac{1}{2} c_f \rho_{air} \left(\frac{v_{wall}}{2} \right)^2 \tag{4.13}$$

where c_f is the skin-friction coefficient, ρ_{air} is the density of the fluid and v_{wall} is the speed of the surface of the rotor in contact with the air. The expression of the skin-friction coefficient c_f is given by:

$$c_f = 2\left(\frac{\kappa}{\ln Re_c} G(\Lambda, D)\right) \tag{4.14}$$

where $G(\Lambda, D)$ is a function defined such that $\frac{\Lambda}{G} + 2\ln\frac{\Lambda}{G} - D$, $\Lambda = 2\ln Re_c$, D is a coefficient equal to $2(\ln 2\kappa + \kappa(C^+ + \overline{C}))$, κ is the Karman constant (0.41), C^+ is a universal constant equal to (5) and $\overline{C}$ is evaluated at 2.1 through experimental approximations. The Reynold number Re_c is defined as $\rho_{air}\frac{v_{wall}h}{\mu_{air}}$, where h is the axial length of the Couette flow.

The value of τ_{wall} is multiplied by the radius of the rotor and integrated over the outer surface of the rotor iron teeth to obtain the resulting torque applied to the rotor. By multiplying this torque by the rotational speed of the rotor, the air gap origin of the aerodynamic friction losses is obtained:

$$P_{friction,airgap} = \frac{c_f \rho_{air} \pi R_{R,e}^4 L_{I,r} \Omega^3}{4} \tag{4.15}$$

Aerodynamic friction between the inner part of the rotor and the permanent magnet ring

The same procedure is applied to obtain the friction torque and losses occurring in the region between the permanent magnets and the inner part of the rotor:

$$P_{friction,PM-rot} = \frac{c_f \rho_{air} \pi R_{R,i}^4 L_{B,R} \Omega^3}{4} \tag{4.16}$$

Aerodynamic friction on the upper and lower edges of the rotor

On the edges of the rotor, a boundary layer problem is considered in which the rotating disk of the rotor is assimilated to a moving wall in contact with ambient air. Classical boundary layer problems are applied to a planar wall travelling at a constant speed. The disks forming the edges are thus decomposed into an infinite number of bands of radial thickness dr travelling at a speed Ωr to which a classical boundary layer problem is applied. The resulting torque is obtained by integrating the shear stress obtained from the boundary layer problem.

The friction shear stress acting on the circular band is obtained through the skin-friction coefficient that is approximated in boundary layer problems by:

$$c_f = \frac{\tau_{wall}}{1/2\rho_{air} u_{wall}^2} \simeq 0.664 Re_x^{-1/2} \tag{4.17}$$

where the characteristic length x for the Reynold number Re_x is the length of the considered band $2\pi r$. The expression of τ_{wall} is given by:

$$\tau_{wall}(r) = \frac{0.664 \rho_{air} \Omega^{3/2} r}{2} \left(\frac{2\pi}{\nu_{air}}\right)^{-1/2} \tag{4.18}$$

where ν_{air} is the kinematic viscosity of the air.

The resulting torque is obtained by integrating the expression of τ_{wall} multiplied by its lever arm over the disks forming the edges of the rotor. The aerodynamic losses due to this torque is given by:

$$P_{friction,edges} = \frac{R_{R,e}^4 - R_{R,d}^4}{4} \frac{0.664}{2} \left(\frac{2\pi}{\nu}\right) 2\pi\rho\Omega^{5/2} \tag{4.19}$$

CHAPTER 5

OPTIMIZATION

This chapter explains the optimization routine used to obtain the parameters of the SHH-AMB under study, leading to the best performances as a FESS. The optimization is a multi-objective problem acting on several variables, being the parameters of the bearing, while ensuring the compliance to constraints that are applied to the devices encountered during the routine. The result of such a procedure is a Pareto front whose every device is the best in one of the objectives for a given performance in the other objectives. The algorithm that is used to solve this problem is a non-dominated sorted genetic algorithm-II (NSGA-II), implemented in the platform *Optimeed*. This chapter starts by presenting the objectives of the optimization problem. Secondly, the variables on which the algorithm acts are listed and explained. The constraints applied to the devices generated by the algorithm are then presented and justified. The process through which a device goes once it is generated by the algorithm, allowing to evaluate the objectives and the constraints, is then explained and the results of the optimization procedure are presented and analyzed.

5.1 Optimization objectives

The objectives that are given to the optimization algorithm are meant to represent the performances of the SHH-AMB under study as a FESS rather than as a bearing. The role of the active magnetic bearing being to reduce the losses whose the guidance system is responsible, it seems relevant to evaluate the self-discharge rate of the FESS, presented in section 4.3 as it is also the main disadvantage of FESS with respect to other energy storage systems. The first objective given to the optimization procedure is thus the self-discharge time defined as the time required for the system to dissipate half of the energy that was initially present within the system. The amount of initial energy E_0 is chosen here as the amount of energy stored in a small battery having the following specifications: 12 V and 100 mAh, corresponding to 4320 J. Regarding the aerodynamic environment of the flywheel, the optimization is performed in two configurations: at atmospheric pressure or at a lower pressure to simulate the flywheel performing in a vacuum chamber. The considered aerodynamic characteristics in the two possible configurations are presented in table 5.1

Table 5.1: Aerodynamic characteristics of the air in the two configurations considered.

Configuration	**Pressure** (bar)	**Density** (kg/m^3)	**Dynamic viscosity** ($\mu Ns/m^2$)
Atmospheric	1.0325	1.292	18.03
Vacuum	0.001	0.00108	19.622

Another issue with FESS is their weight and the space they can take, especially if the self-discharge time is aimed at being maximized. To avoid the results of the optimization simply being the heaviest flywheel, a second objective is given to the algorithm, being the total mass of the system that is to be minimized. The purpose of the optimization procedure is thus to find the FESS that dissipates the less quickly its energy while being as light as possible. The optimization objectives are summarized in table 5.2.

Table 5.2: Optimization objectives.

Objective	**Target**
Self-discharge time	maximize
Total mass	minimize

5.2 Optimization variables

This section enumerates the variables that are given to the optimization algorithm and how they are linked to the SHH-AMB. The variables are split in different sets regarding the nature of the effect of the parameters. The variables affecting the dimensions of the ferromagnetic parts, the permanent magnets and the windings dimensions are first presented. The second set of variables affects the electromagnetic behavior of the bearing through the windings and the permanent magnets.

5.2.1 Geometrical variables

A significant part of the variables given to the optimization procedure are related to the geometry of the bearing. It could be chosen to provide each of the parameters presented in fig. 2.2 to the optimization algorithm to let it act on the dimensions of the bearing to obtain the best performances. This choice would lead to many devices that are not physically possible due to the random nature of the value that takes the optimization variables in a genetic algorithm (e.g., a bearing with inner radii greater than outer ones). Constraints could be employed to remove these unfeasible devices, but would degrade the convergence of the algorithm. It has been decided to employ ratios rather than absolute values of the dimensions to avoid this problem. The value of the outer radius of the stator $R_{S,e}$, which is the greatest radius for a feasible machine, is first set and the other radii are determined thanks to the ratios defined in table 5.3. In that way, unfeasible machines are avoided without additional constraints. The value of $R_{S,e}$ is not set as an optimization variable but at 130 mm, the maximum acceptable value possible for the prototype, as it has been observed in preliminary optimizations that maximizing the self-discharge time of a FESS leads to machines that are radially spread at a most. The same idea is employed for the axial lengths that are determined from the value of L_{PM} and the ratios defined in table 5.3. As no similar conclusions can be drawn for the length of the permanent magnets L_{PM}, this latter is part of the optimization variables provided to the algorithm.

Table 5.3: Definition of the ratios over the dimensions of the bearing that are employed as optimization variables.

Symbol	Signification	Expression
$\alpha_{R_{PM}}$	Ratio between the stator outer radius and PM inner radius	$R_{S,e}/R_{PM,i}$
$\alpha_{R_{S,i}}$	Ratio between the PM inner radius and stator inner radius	$R_{PM,i}/R_{S,i}$
$\alpha_{R_{W,i}}$	Ratio between the stator inner radius and windings inner radius	$R_{S,i}/R_{W,i}$
$\alpha_{R_{R,e}}$	Ratio between the windings inner radius and rotor outer radius	$R_{R,e}/R_{W,i}$
$\alpha_{R_{R,i}}$	Ratio between the rotor outer radius and rotor inner radius	$R_{R,i}/R_{R,e}$
$\alpha_{R_{R,d}}$	Ratio between the rotor inner radius and rotor innermost radius	$R_{R,i}/R_{R,d}$
α_{L_B}	Ratio between the rotor middle width and stator PM width	$L_{B,r}/L_{PM}$
α_{L_R}	Ratio between the rotor iron teeth width and rotor middle width	$L_{I,r}/L_{B,r}$
α_{L_S}	Ratio between the stator iron teeth width and PM width	$L_{I,s}/L_{PM}$
α_{L_W}	Ratio between the winding inner width and stator iron teeth width	$L_{W,i}/L_{I,s}$

To optimize the performances of the bearing, the value of the outer opening angle of the windings $\Theta_{W,e}$ is set at the maximum possible value: 90 °. The inner opening angle $\Theta_{W,i}$ is left as an optimization variable from which the outer axial length of the end windings $L_{W,e}$ is determined so that the cross-sectional area of the windings in the (r, θ) and (r, z) planes are equal, leading to:

$$L_{W,e} = 2(S_W/(R_{S,i} - R_{W,i} + L_{W,i}) \tag{5.1}$$

where S_W is the cross-sectional area of the windings evaluated in the (r, θ) plane:

$$S_W = \frac{(\Theta_{W,e} - \Theta_{W,i})\left(R_{S,i}^2 - R_{W,i}^2\right)}{2} \tag{5.2}$$

5.2.2 Electromagnetic variables

The other variables are related to the magnetization of the permanent magnets and the number of turns in the windings. The number of turns in the windings N_W impacts the current stiffness, which is proportional to this number. On the other hand, the electrical resistance also depends on this number. The number of turns N_W is thus provided as a variable to the optimization algorithm so that a trade-off between high current stiffness and high electrical resistance is found by the algorithm.

To make the polarizing magnetic flux density independent of the dimensions of the bearing, a fill factor is applied to the permanent magnet PM_{FF} that multiplies the remanent flux density of the permanent magnets. This factor also helps to model the real permanent magnet that is not made of one ring but of several rectangular permanent magnets that do not occupy all the available area. This fill factor is also provided as an optimization variable.

The optimization variables and the intervals of values the algorithm is allowed to give to these variables are summarized in table 5.4.

Table 5.4: Optimization variables.

Variable	**Units**	**Range**
$\alpha_{R_{PM}}$	-	[0.7 - 0.999]
$\alpha_{R_{S,i}}$	-	[0.7 - 1]
$\alpha_{R_{W,i}}$	-	[0.9 - 0.999]
$\alpha_{R_{R,e}}$	-	[0.85 - 0.999]
$\alpha_{R_{R,i}}$	-	[0.05 - 0.95]
$\alpha_{R_{R,d}}$	-	[0.05 - 0.9]
L_{PM}	mm	[10 - 30]
α_{L_B}	-	[0.9 - 1.2]
α_{L_R}	-	[0.7 - 1.4]
α_{L_S}	-	[0.6 - 1.3]
$\Theta_{W,i}$	$^\circ$	[65 - 88]
α_{L_W}	-	[0.0 - 1.1]
N_W	#	[20 - 300]
PM_{FF}	-	[0.45 - 0.9]

5.3 Optimization constraints

The optimization algorithm generates machines from the variables given in section 5.2. Some of these machines might not be feasible, for practical reasons. To avoid this kind of unfeasible machines being output by the algorithm, optimization constraints are added to the problem. The machines that do not comply with these additional constraints are removed from the Pareto front that is output by the algorithm. In the interface used for the optimization, to each constraint is associated an expression that is evaluated for each machine that is generated by the algorithm. The machine complies with the constraints only if the values of all the expressions are negative. The expression related to a constraint must be chosen carefully so that a machine that almost complies to the constraint has a value that is slightly positive for this expression, as the algorithm considers this value to adapt the variables in the next generation of machine. The constraints employed for this optimization are presented, justified and grouped by their nature.

5.3.1 Geometrical constraints

The geometrical constraints groups the constraints that are required to ensure the geometrical coherence of the machine that cannot be ensured by the intervals used in the optimization variables. These constraints concern the overlapping nature of the windings and the number of turns in the coils.

Overlapping constraints

As explained in section 2.1, the parameters used to describe the bearing allow the windings to be inset and overlapping which means the end windings are allowed to be placed inside the iron poles (inset) and that the end windings of two coils are allowed to be placed on each other. It is required to apply a limit over the external length of the windings $L_{W,e}$ to avoid the end windings to reach the other iron pole and to leave enough space to bend the cables (fig. 5.1). The overlapping configuration also requires room for the end windings to be superimposed, either in the air gap or between the permanent magnets and the stator iron teeth. Fig. 5.2 illustrates the two configurations. As the results of the preliminary optimizations show long air gaps, the windings are superimposed in the air gap.

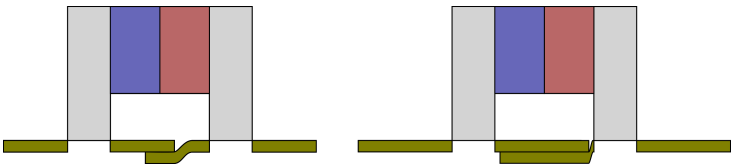

Figure 5.1: Overlapping configuration. The left configuration is not feasible because of a too big outer axial length of the winding, leaving not enough space to bend the cables.

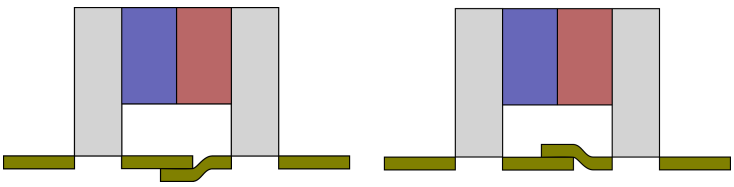

Figure 5.2: Overlapping configuration: The windings are superimposed in the air gap (left) or between the permanent magnets and the stator iron teeth (right).

These two constraints are modeled with the following expressions:

$$\begin{aligned} &L_{W,e} - L_{I,S} - 2L_{PM} + 3(R_{S,i} - R_{W,i}) \\ &2R_{S,i} - R_{PM,i} - R_{W,i} \end{aligned} \tag{5.3}$$

where the first and second lines are respectively the constraints related to the axial length of the end windings and to the radial space available in the air gap.

Number of turns in the coils

The number of turns in the coils N_W is left as an optimization variable. From this number, the fill factor η and the cross-sectional area of one coil, the maximum cross-sectional area of the conductors is evaluated. The more turns are made, the smaller this area is. As infinitely thin cables are not achievable, a minimal cross-sectional area of cable is added to the optimization constraints to avoid unfeasible windings:

$$S_{c,min} - \frac{S_W \eta}{N_W} \tag{5.4}$$

where $S_{c,min}$ is the minimal cross-sectional area of the conductors, set to 0.1 mm^2.

5.3.2 Saturation constraints

The model developed in chapter 3 does not take the magnetic saturation occurring in the ferromagnetic materials into account. This is not a problem if the magnetic flux density in the ferromagnetic materials remains under the saturation level of the material. Otherwise, the global characteristics obtained by the model are not valid for the real bearing. Machines in which saturation of the magnetic flux density occurs in the ferromagnetic materials must be removed from the optimization.

In the SHH-AMB under study, the magnetic saturation is likely to appear in three regions of the bearing: The stator and rotor iron teeth and the inner part of the rotor. As illustrated in fig. 5.3, the magnetic saturation appears if the section perpendicular to the circulation of the magnetic flux density of one of these regions becomes too small.

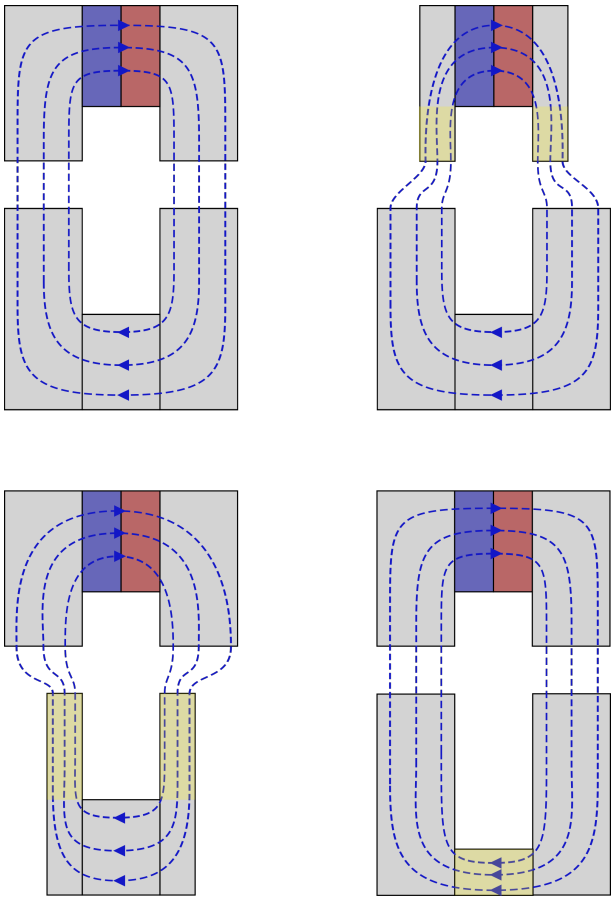

Figure 5.3: Illustration of the three places at which magnetic saturation can occur in the SHH-AMB: No saturation (upper left), saturation in the stator iron teeth (upper, right), in the rotor iron teeth (lower left) and in the inner part of the rotor (lower right).

The model not computing the magnetic flux density inside the ferromagnetic materials, this latter is estimated from the magnetic flux density in the air gap. As the ferromagnetic are assumed ideal in the model, the magnetic flux entering in one of the iron teeth is conserved in the whole ferromagnetic

part. The magnetic flux flowing through the stator teeth $\Phi_{iron,stator}$ is obtained by integrating the air gap radial magnetic flux density over the entry of one of the stator iron teeth. By assuming a uniform distribution of the magnetic flux density in the iron teeth, the magnetic flux density is estimated by dividing the magnetic flux by the surface. The most critical place is where the surface is the smaller, for the stator, it is at the entry of the iron teeth, at $r = R_{S,i}$. The saturation constraint for the stator iron teeth is thus given by:

$$\frac{\Phi_{iron,stator}}{2\pi R_{S,i} L_{I,S}} - B_{sat} \tag{5.5}$$

where B_{sat} is the saturation level of the ferromagnetic materials, set at 1.5 T in this optimization.

The saturation constraint for the rotor iron teeth is obtained by analogy to the stator one. The most critical surface is at the smallest radius $R_{R,i}$:

$$\frac{\Phi_{iron,rotor}}{2\pi R_{R,d} L_{I,R}} - B_{sat} \tag{5.6}$$

The constraint avoiding the saturation in the inner part of the rotor is obtained by estimating the magnetic flux density from the magnetic flux $\Phi_{iron,rotor}$ as it is conserved in the magnetic circuit that is the rotor. This constraint is thus written:

$$\frac{\Phi_{iron,rotor}}{\pi \left(R_{R,i}^2 - R_{R,d}^2 \right)} - B_{sat} \tag{5.7}$$

5.3.3 Performances constraints

The last set of constraints regard the performances of the bearing. The optimization not aiming at optimizing these performances, it is required to ensure that the bearing is performant enough to be used in this flywheel application.

Axial stability

Section 4.1 presented a module that evaluates the axial equilibrium position of the rotor, once gravity is applied. If the axial stiffness is not sufficient, the bearing is not capable of sustaining its own weight and the axial equilibrium module returns a very high unrealistic value Δ_z. Such machines are removed from the optimization by applying the following constraint:

$$\Delta_{z,eq} - \Delta_{z,max} \tag{5.8}$$

where $\Delta_{z,max}$ is a maximum value of axial equilibrium point, set at 5 mm for this optimization.

A safety factor is additionally applied to the weight that the bearing is able to heave through an additional constraint consisting in evaluating the magnetic force developed on the rotor showing an axial displacement being twice the value of the equilibrium point. This force is expected to be twice the weight of the rotor, if not, it means that the rotor is unlocked from the stator and is not stable enough axially. To account for the degressive behavior of the axial displacement - axial force characteristic, machines that produce at least 90 % of twice the weight of the rotor are accepted by the constraint that is illustrated in fig. 5.4. This gives rise to the following expression:

$$F_{mag}(2\Delta_{z,eq}) - 0.9 \times 2 m_{rotor} g \tag{5.9}$$

Lift-off current

I f the controller of the active magnetic bearing is turned off, the rotor rests on lift-off ball bearings that leave a free play. The rotor is not in contact with this ball bearing as its position is controlled. As the controller is turned on, it is required to overcome the radial detent force by imposing a sufficient current in the windings whose minimal value i_{min} is given by:

$$i_{min} = \frac{k_\epsilon \epsilon_{init}}{k_i} \tag{5.10}$$

where ϵ_{init} is the free play left by the lift-off ball bearings, set at 1.5 mm in this optimization.

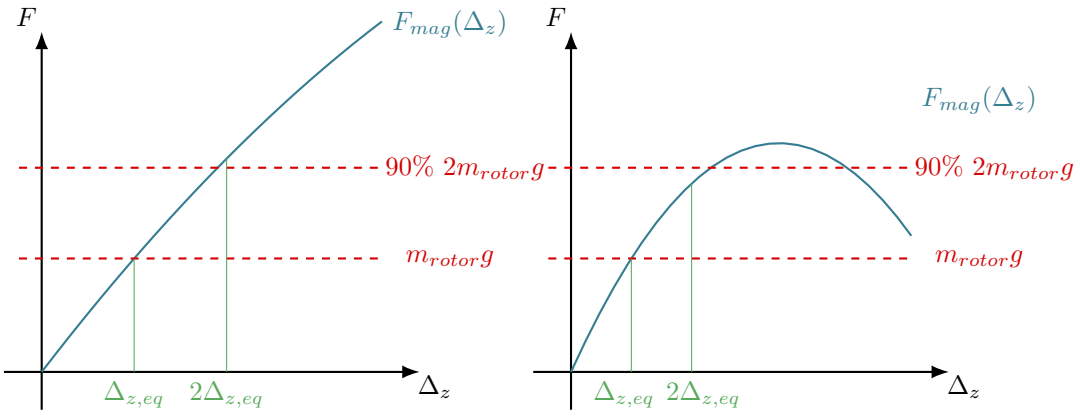

Figure 5.4: Illustration of the axial stability constraint. The left and right machines are respectively stable and not stable enough.

The maximum achievable current I_{max} is set by the power electronics that supplies the magnetic bearing either by the voltage limit V_{max} set at 12 V or by the power limit P_{max} set at 24 W:

$$i_{max} = min(\frac{V_{max}}{R}, \sqrt{\frac{P_{max}}{R}}) \tag{5.11}$$

The lift-off current constraint ensures that the power electronics is capable of lifting the bearing such that i_{max} is greater than I_{min}:

$$i_{min} - i_{max} \tag{5.12}$$

5.3.4 Maximum speed

The optimization objective related to the self-discharge time considers an initial energy of 4320 J stored in the flywheel. It is thus required that the mechanical design of section 4.2 allows the rotor to rotate fast enough to store this energy. The constraints is expressed as:

$$E_0 - \frac{I_z \Omega_{max}^2}{2} \tag{5.13}$$

where Ω_{max} is the maximum rotation speed of the rotor.

The constraints applied in the optimization problem are summarized in table 5.5

Table 5.5: Optimization constraints.

Constraint	**Expression** (< 0)	**Units**
Overlap, axial	$L_{W,e} - L_{I,S} - 2L_{PM} + 3(R_{S,i} - R_{W,i})$	mm
Overlap, radial	$2R_{S,i} - R_{PM,i} - R_{W,i}$	mm
Conductor cross-section	$S_{c,min} - \frac{S_W \eta}{N_W}$	mm^2
Saturation, stator teeth	$\frac{\Phi_{iron,stator}}{2\pi R_{S,i} L_{I,S}} - B_{sat}$	T
Saturation, rotor teeth	$\frac{\Phi_{iron,rotor}}{2\pi R_{R,d} L_{I,R}} - B_{sat}$	T
Saturation, rotor inner part	$\frac{\Phi_{iron,rotor}}{\pi\left(R_{R,i}^2 - R_{R,d}^2\right)} - B_{sat}$	T
Axial equilibrium	$\Delta_{z,eq} - \Delta_{z,max}$	mm
Axial stability	$F_{mag}(2\Delta_{z,eq}) - 0.9 \times 2m_{rotor}g$	N
Lift-off current	$i_{min} - i_{max}$	A
Maximum speed	$E_0 - \frac{I_z \Omega_{max}^2}{2}$	J

5.4 Optimization chart

This section presents a block diagram explaining the process through which goes a machine generated by the algorithm to evaluate the constraints and the objective thanks to the models presented in chapters 3 and 4 in an appropriate order. The optimization chart is available in fig. 5.5

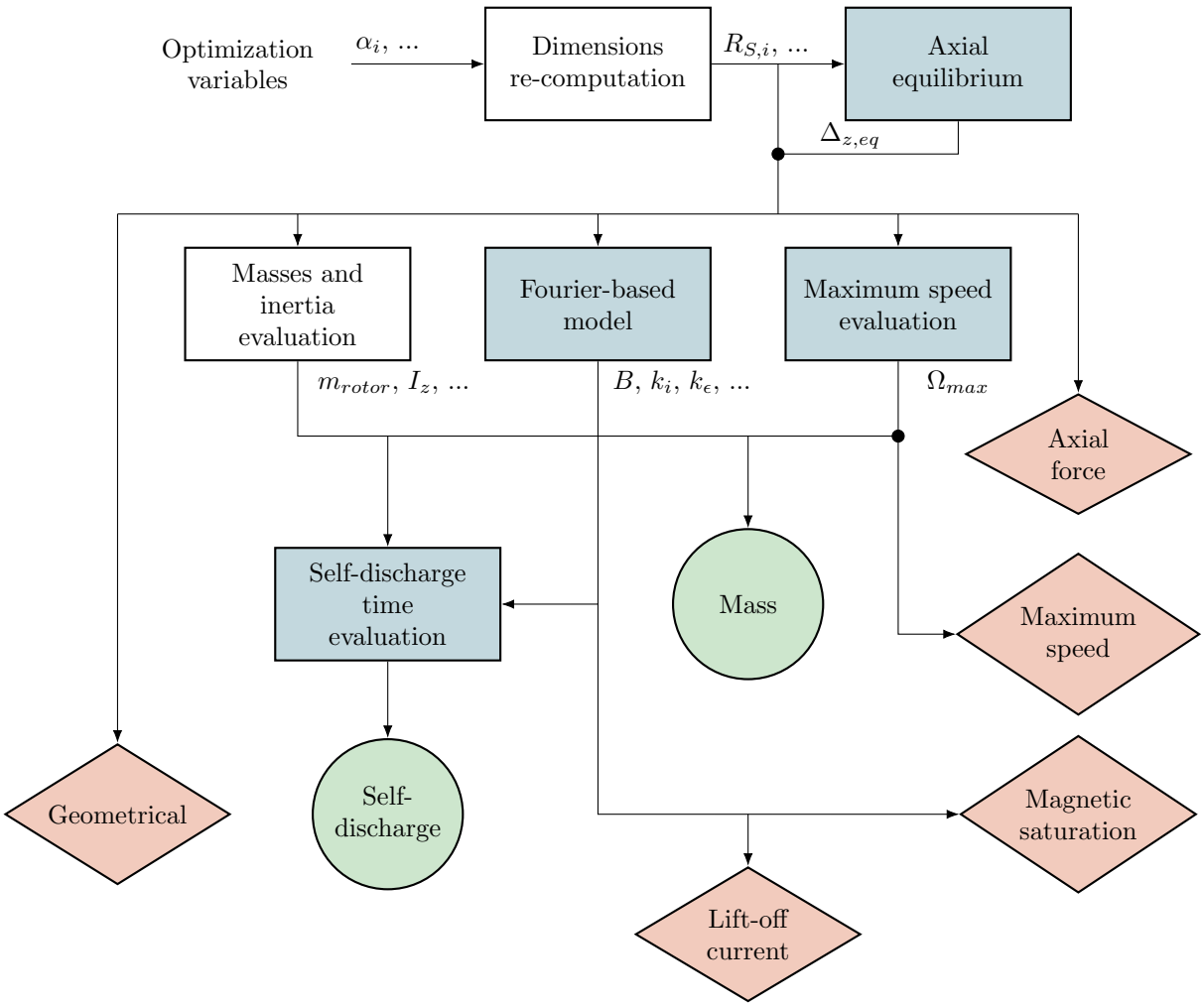

Figure 5.5: Optimization chart. Models are in blue rectangles, constraints in red rhombuses and objectives in green circles.

5.5 Results and analysis

This section shows the results that are output from the optimization algorithm with the optimization objectives, variables, and constraints that are presented in this chapter. The validity of the optimization is first assessed by analyzing the variables and the value of the constraints of the machines that are part of the Pareto front. The Pareto fronts are presented, and the methodology employed to choose the dimensions of the prototype is finally explained.

5.5.1 Variables and constraints at the stop

Table 5.4 shows the different optimization variables and the range of value of the optimization algorithm is allowed to give to these variables. The upper and lower limits of these intervals are called the stop. It is important to make sure that the optimization variables of the machines of the Pareto front output by the optimization algorithm are not at one of the stop of the interval concerned. If it is the case, the stop applied to this interval limits the performances of the machine and the value of the stop must be called into question. If the stop cannot be changed for practical reasons, the optimization variables are removed from the optimization problem and are set at the value of the stop to improve the convergence of the algorithm. The same procedure is applied to the constraints. This sections details the variables that are subject to this concern by analyzing the results of the first optimization and explains the changes that are applied.

Inner radius of the permanent magnets

The optimization variable $\alpha_{R_{S,i}}$ of the machines being part of the Pareto front tends to be at the upper stop of its interval (1.0) giving rise to a machine similar to what is shown in fig.5.6 in which the permanent magnets have the same inner radius than the stator teeth. The effect of the iron teeth is still present in such a configuration, as the permanent magnets have a relative magnetic permeability similar to the air. As the Fourier model does not require the existence of the region V to be functional, the optimization variable is removed from the problem and $R_{S,i}$ is set equal to $R_{PM,i}$.

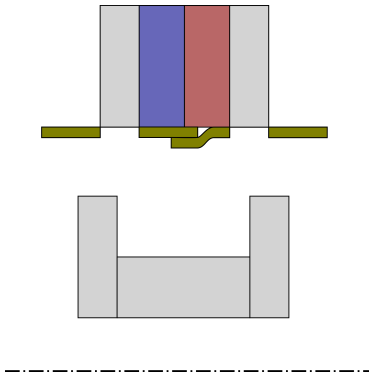

Figure 5.6: Illustration of a machine whose $\alpha_{R_{S,i}}$ is equal to 1.0.

Radius of the hole of the rotor

The optimization variable $\alpha_{R_{R,d}}$ also tends to be at its lower stop for the machine of the Pareto front leading to rotor as radially spread as possible (fig. 5.7). This result seems obvious in the point of view of the optimization of the self-discharge time as the inner elements of the rotor are subject to less aerodynamic friction than the outer parts of the rotor. As room in the hole of the rotor is required for auxiliary elements (chapter 6) full rotors are not possible and a minimal value for $R_{R,d}$ is required. The optimization variable is removed from the problem, the value of $R_{R,d}$ is set at $25mm$ and a constraint is added to avoid machines presenting a $R_{R,i}$ smaller than $R_{R,d}$.

Magnetic saturation

The constraint related to the magnetic saturation in the inner part of the rotor tends to be as close to zero as possible, such that the machine of the Pareto front have a magnetic flux density inside the rotor as close to the saturation level as possible. As the aerodynamic friction occurring between the inner part of the rotor and the permanent magnets is taken into account, the optimization algorithm tries to move the matter of the rotor toward the iron teeth that are really useful to limit the friction and to minimize

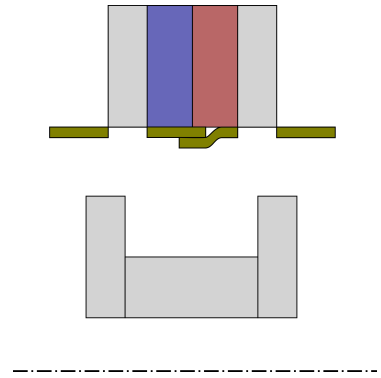

Figure 5.7: Illustration of a machine whose $\alpha_{R_{R,d}}$ is at its lower stop.

the mass of the bearing. The same observation is made in the saturation constraint in the stator teeth. The magnetic saturation constraint requiring an evaluation of the magnetic flux density distribution by the Fourier model to obtain the magnetic fluxes, nothing can be changed in the problem to improve the convergence.

5.5.2 Pareto fronts

Fig. 5.8 shows the results of the optimization procedure and highlights the Pareto front gathering the optimized machines presenting a maximum self-discharge time for a given total mass. The optimization is performed at atmospheric aerodynamic conditions and in the vacuum. As the machine resulting of the two optimizations are similar, only the results output by the optimization in the vacuum are kept. Fig. 5.9 illustrates three machines being part of the Pareto front, the lightest machine with the smallest self-discharge time, the heaviest machine with the greatest self-discharge time and an intermediate machine chosen in the middle of the Pareto front.

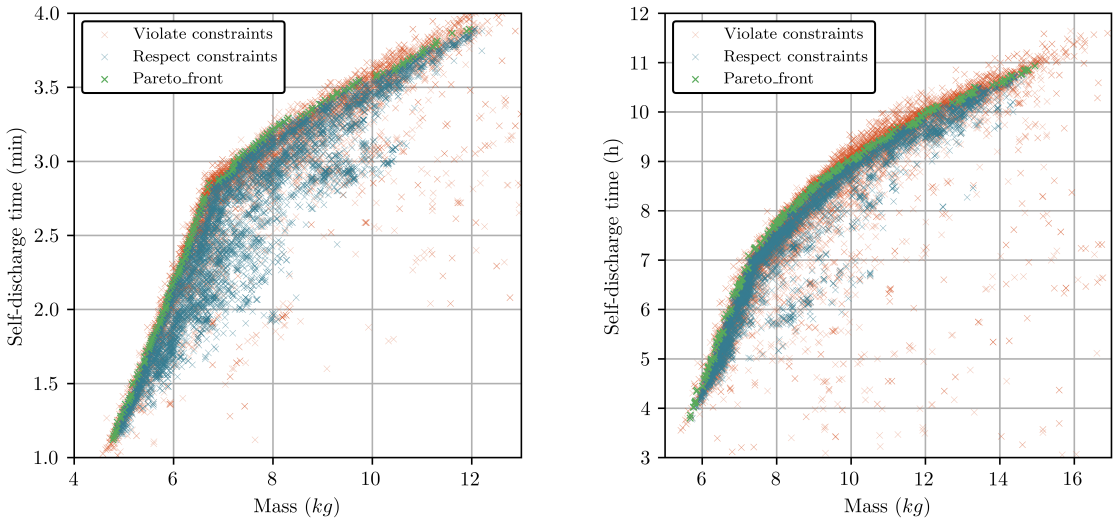

Figure 5.8: Results of the optimization procedure for two aerodynamic conditions: Atmospheric pressure (left) and vacuum (right). The units of the self-discharge time for the atmospheric is the minute and the hour for the vacuum.

5.5.3 Analysis

Elbow in the Pareto front

The Pareto front of fig. 5.8, presents an elbow. The self-discharge time of the machine increases with respect to the mass faster for machines with masses smaller than 7 kg than for heavier machines. Such elbow appears in optimization problems as one of the optimization variables reaches or leaves its lower

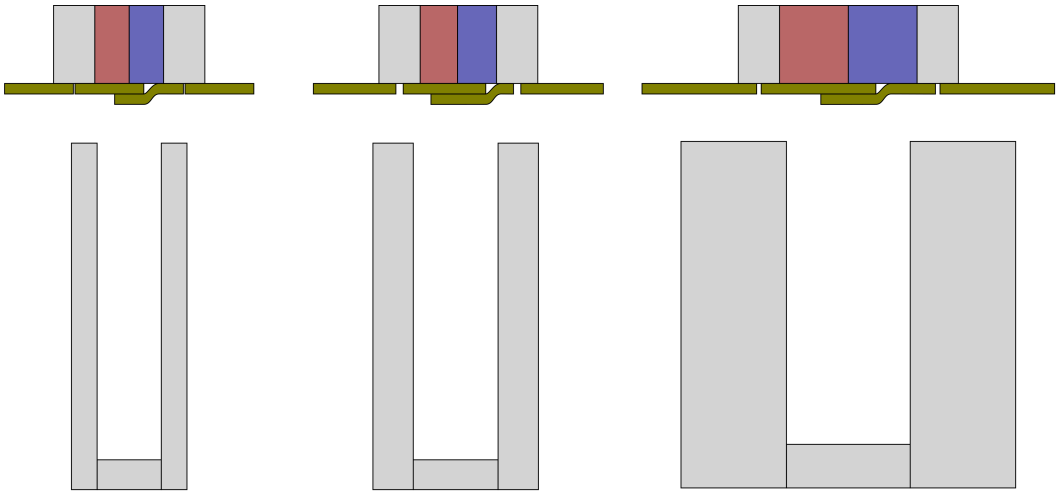

Figure 5.9: Machines being part of the Pareto front: Lightest machine with lowest self-discharge time (left), the heaviest machine with greatest self-discharge time (right) and intermediate machine (center).

or upper stop, respectively. The optimization variable responsible for the elbow is identified by observing the value of the optimization variables of the machine being part of the Pareto front with respect to one of the objectives. The variable that leaves or reaches one of its stops when the optimization objective reaches the value at which the elbow occurs is responsible for the elbow. Fig. 5.10 shows that the axial length of the permanent magnet L_{PM} is the variable responsible for the elbow in the Pareto front.

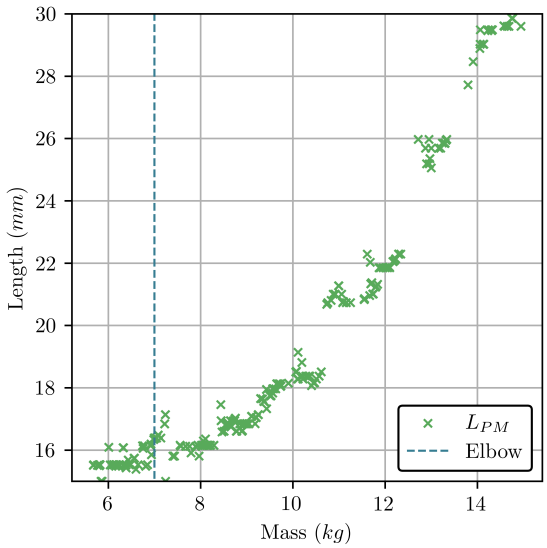

Figure 5.10: L_{PM} with respect to the mass for the machine part of the Pareto front. The variable leaves its lower stop (15 mm) when the mass of the machine is $7kg$.

The length of the permanent magnets being the responsible of the presence of the elbow translates the trend of the algorithm to minimize the axial length of the rotor as long as it is possible to minimize the weight as it is more efficient to add matter radially to improve the self-discharge time than axially. Once it is not possible to add matter radially, the algorithm increases the axial size and the inertia of the machine to keep improving the self-discharge time at a minimal weight.

Length of the air gap

The machines being part of the Pareto front tend to show high value of air gap length (about 10 mm) compared to what is classically observed for magnetic bearings and electrical machines (about 1 mm). To explain the presence of such big air gaps, the performances of one machine, chosen arbitrary among those forming the Pareto front, with respect to the length of this air gap is assessed in fig. 5.11. The losses leading to the discharge are evaluated separately by distinguishing the aerodynamic losses and the Joule losses. The length of the air gap is changed with the outer radius of the rotor $R_{R,e}$. If the air gap is shorter, the contribution of the aerodynamic losses is smaller than the contribution of the Joule losses, leading to a smaller self-discharge time. Such an observation is explained by the characteristics of the bearings presented in fig. 5.12. The aerodynamic losses are reduced with the smaller air gap length because the inertia of the rotor is increased and the speed required to store the initial energy is lowered. The rotor operates at lower speed and incurs less friction. The Joule losses are increased when the air gap is tightened because the radial stiffness increases faster than the current stiffness. The current required to control the bearing is thus more important, and so are the Joule losses. The algorithm tends to minimize the Joule losses due to their constant nature, unlike the aerodynamic losses that are more significant at high speed than at low speed. The self-discharge time of the flywheel would be improved if the air gap was slightly longer, but such machines do not have sufficient axial position stiffness to withstand the rotor and are removed from the optimization.

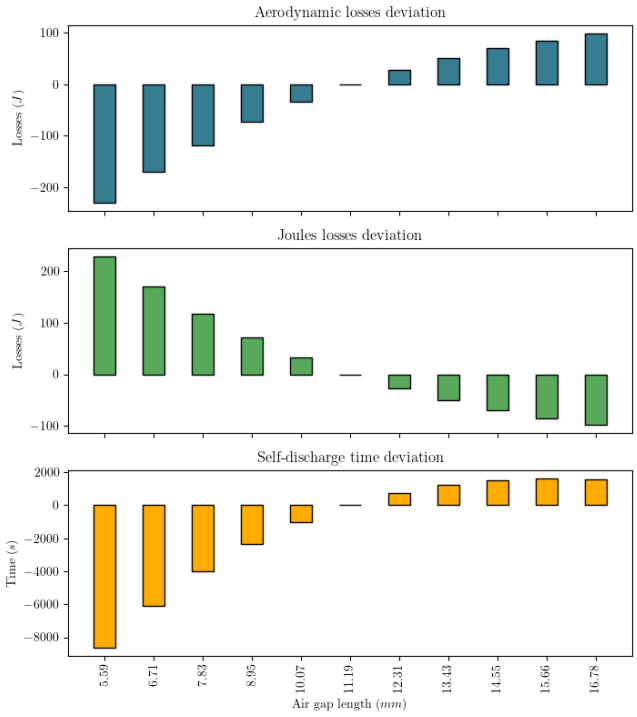

Figure 5.11: Performances of the flywheel with respect to the length of the air gap. The optimized machine is at the center of the figure.

5.5.4 Choice of the dimensions

The optimization problem being a multi-objective problem, the output of the optimization algorithm is a Pareto front whose every machine is optimal in its manner. By choosing a machine from this Pareto front, it is ensured that no other machine with the same mass has a better self-discharge time. But selecting one machine can still be more judicious than choosing another one. This section explains how the dimensions selected for the prototype are obtained.

Fig. 5.10 showed that machine under 7 kg have the optimization variable L_{PM} at its lower stop. It seems thus intuitive not to pick one of these machines as the algorithm was constrained to this value of L_{PM} and the machines are thus not optimal compared those that would have been obtained if the lower

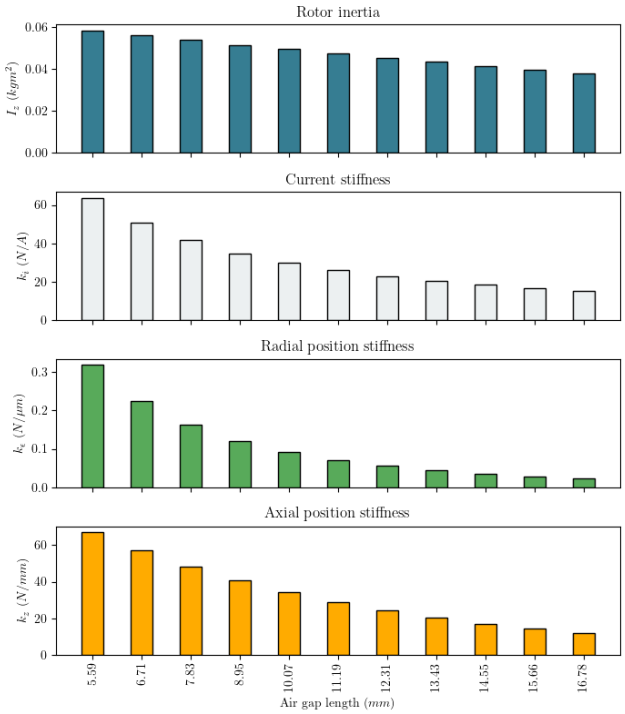

Figure 5.12: Characteristics of the bearing with respect to the length of the air gap. The optimized machine is at the center of the figure.

stop was set to a smaller value. Similarly, machines above 14 kg have L_{PM} at its upper stop and are not selected. From that point, the choice of the machine relates to the acceptable weight and the desired self-discharge performances. The exact values of the parameters chosen for the prototype are given in chapter 6.

CHAPTER 6

EXPERIMENTAL VALIDATION

This chapter presents the prototype and its working environment for the experimental validation of the SHH-AMB topology employed as a FESS. The objective of this experimental validation is to test the feasibility of such a device, but also to assess the accuracy of the magnetic model developed in chapter 3. A prototype was designed based on the output of the optimization presented in chapter 5 and built to be characterized. This chapter is organized as follows: the dimensions and characteristics of the prototype are first presented. Secondly, the assembly of the different parts is detailed. The next section is about the manufacturing processes tried to produce the windings. A description of the connection of the test bench is then presented. The controller allowing the flywheel to levitate is then designed. Finally, the resulting performances of the prototype are discussed and compared to the predictions of the magnetic model.

6.1 Dimensions and characteristics

The dimensions and characteristics of the prototype presented in this chapter are given in table 6.1. These values are based on the results of the optimization realized in chapter 5 to offer optimal performances. Some of these values have been adjusted for various reasons, such as $R_{R,d}$, which has been reduced to adjust the play, left between the rotor and the lift-off ball bearings. The length of the permanent magnets L_{PM} was constrained by the dimensions of the available products. Regarding $R_{W,i}$, it has been reduced as the windings were handcrafted and required more space, as shown in section 6.3.

Table 6.1: Dimensions and characteristics of the prototype.

Parameter	Output of the optimization	Reviewed value	Unit
$L_{I,s}$	5.378140876145302	5	mm
$R_{S,i}$	121.6665788425991	121	mm
$R_{S,e}$	130.0	130	mm
$L_{I,r}$	9.747852612729723	10	mm
L_B	22.259575271463756	22	mm
$R_{R,i}$	34.737440896239607	35	mm
$R_{R,e}$	111.10561554554418	111	mm
$R_{R,d}$	25.0	24.5	mm
L_{PM}	21.57223057900924	21	mm
$R_{PM,i}$	121.6665788425991	121	mm
PM_{FF}	0.7	0.7	$-$
B_{rem}	1.44	1.44	T
$L_{W,i}$	8.047032692554037	8	mm
$L_{W,e}$	44.06283447725961	44	mm
$R_{W,i}$	120.51058300006301	115	mm
$T_{W,i}$	71.95831512482563	72	$^\circ$
$T_{W,e}$	89.0	89	$^\circ$
N_W	41	41	$\#$
k_z	14.32102	14.32102	N/mm
k_ϵ	0.02828	0.02828	$N/\mu m$
k_i	8.53442	8.53442	N/A

6.2 Prototype assembly

This section details the different parts constituting the prototype and the procedure to assemble them. The parts have been designed to respect the dimensions specified in table 6.1. The main assembly is divided into two subassemblies: the rotor and the stator. An overview of the main assembly is shown in fig. 6.1. Other parts have been designed to provide specific tools to assemble the prototype.

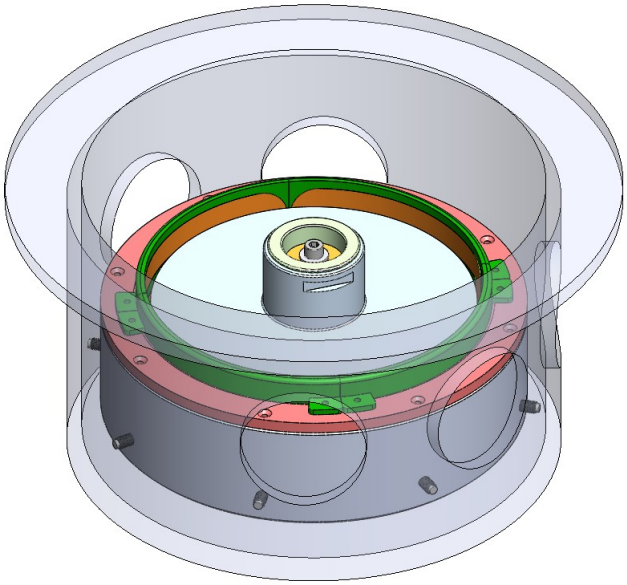

Figure 6.1: Total assembly within the vacuum enclosure.

6.2.1 Rotor assembly

The rotor assembly is composed of two parts, the first one being the rotor or flywheel itself and the second part being the squirrel cage for the induction machine. The rotor assembly is shown in fig. 6.2.

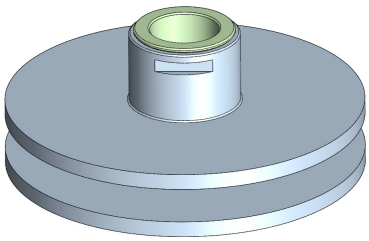

Figure 6.2: Rotor assembly with the flywheel in gray and the squirrel cage in green.

Rotor / Flywheel

The flywheel is the main part of the rotor assembly. It is made of steel (ST37 - s235 - 1.0037) and weights 6.750 kg. Different views of the flywheel model as well as a real picture of it are depicted in fig. 6.3. It is noticed that there are two grooves on the top of it that are used to put the claws of a bearing extractor, as explained in section 6.2.3.

Squirrel cage

The squirrel cage is the rotor of the induction machine that is directly mounted on the flywheel. It is made of aluminum (6061-T6) to carry the current induced by the stator of the motor. Different views of the squirrel cage model as well as a real picture of it are depicted in fig. 6.4.

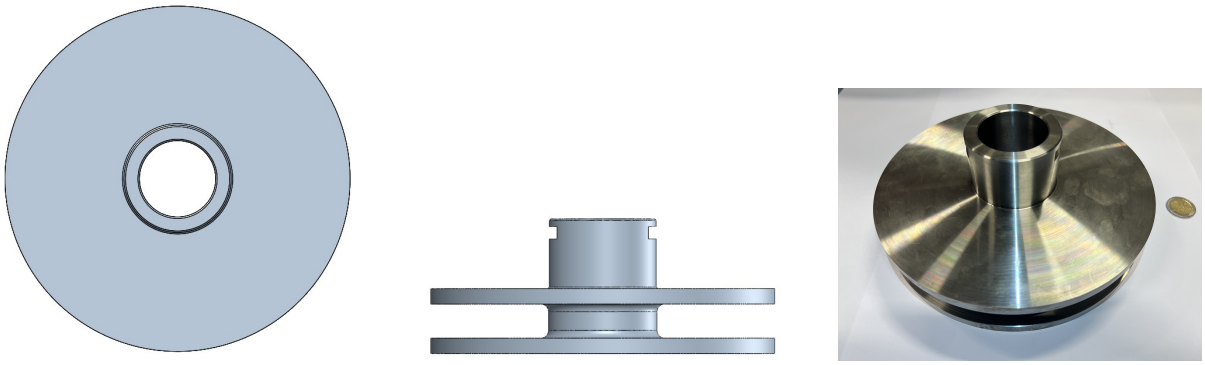

(a) (b) (c)

Figure 6.3: Different views of the flywheel: (a) top view (b) side view (c) real view.

(a) (b) (c)

Figure 6.4: Different views of the squirrel cage: (a) top view (b) side view (c) real view.

Rotor assembling process

Fig. 6.5 shows how the squirrel cage is inserted into the flywheel. A $k5/H6$ tolerance is imposed between these two parts so that the squirrel cage is tightened enough to drive the flywheel.

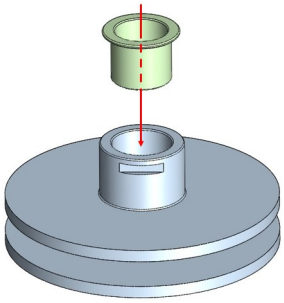

Figure 6.5: Fitting the squirrel cage into the flywheel.

6.2.2 Stator assembly

The stator part of the assembly is composed of many parts, as depicted in fig. 6.6. It is formed by the following subassemblies:

- The support of the stator and its axial and lateral supports.
- The shaft with the lift-off ball bearings, the armature of the induction machine, the spacers, and the fixation elements.
- The stator of the magnetic bearing composed of two rings between which permanent magnets are inserted and maintained thanks to a spacing part.

- A clamping part to maintain the stator of the magnetic bearing in place and to fix the supports of the windings.
- The windings and their supports.

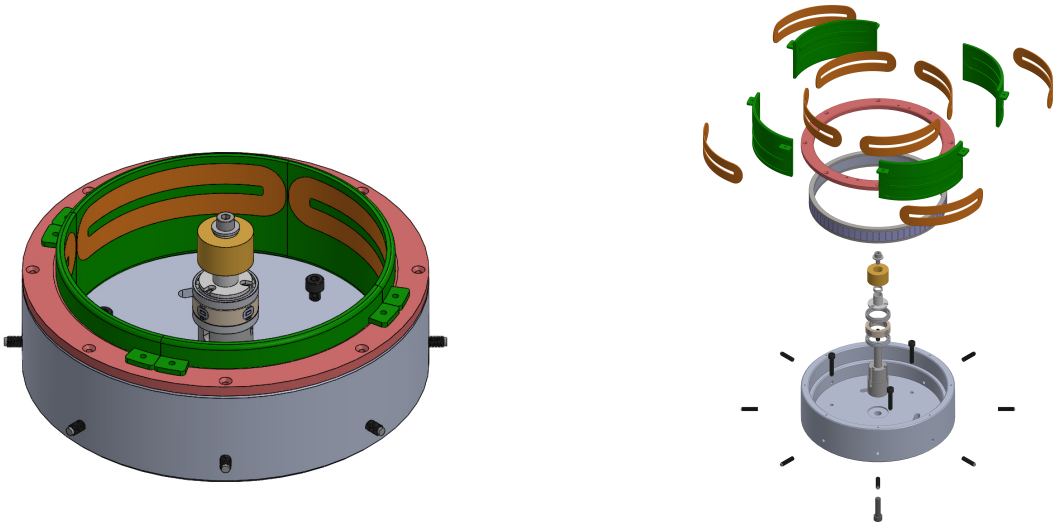

(a) (b)

Figure 6.6: Stator assembly: (a) Assembled, (b) Splitted.

Support of the stator subassembly

The support of the stator subassembly is mainly composed of an aluminum part, which is the base of the stator assembly. Several holes of different sizes are drilled and threaded, as it is visible in fig. 6.7:

- height tapped holes on the top to fix the clamping part
- height tapped holes on the side to put lateral supports
- three tapped holes at the bottom to put axial supports
- three curved buttonholes for routing sensor and motor cables
- one screw hole at the bottom center for the bottom screw of the shaft

(a) (b) (c)

Figure 6.7: Different views of the support of the stator: (a) top view (b) side view (c) real view.

The support of the stator is designed to fit in a vacuum enclosure, and to be maintained thanks to axial and lateral supports. These supports are screws with a soft-tip to damp the vibrations of the device due to the motion of the flywheel (fig. 6.8). The axial supports have a screw head that remains below the flywheel, and that allows to adjust the height of the support of the stator from the top. The radial supports do not have a screw head, so that they can be totally inserted in their thread to leave space for the support of the windings. They are used to adjust the position of the support of the stator in the center of the enclosure and block its motion.

Figure 6.8: Radial (left) and axial (right) soft-tip screws.

At the center of the support of the stator, a recess has been designed to accommodate the shaft assembly with a g6/H7 tolerance (fig. 6.7a and 6.7c).

Shaft subassembly

The shaft assembly, presented in fig. 6.9, is composed of several parts that ensure different functions. The shaft itself, made of stainless steel (AISI 316L), supports the following parts. From top to bottom, the first element is the armature of the induction machine (the yellow part in fig. 6.9a and 6.9b) that is maintained by two aluminum (6061-T6) spacer. The lower spacer of the armature of the motor is in contact with the inner ring of a first lift-off ball bearing. Grooves are made in this spacer to leave a possibility to route the three cables of the motor from below. A second lift-off ball bearing, whose inner ring lies on the lowest shoulder of the shaft, surrounds the position sensors compartment with the first bearing. The position sensors compartment is composed of four copper coils that form inductances within a 3D-printed resin support. Resin printing has been chosen for its great precision. These elements are clamped against the bottom shoulder thanks to a screw and a washer inserted in the upper tip of the shaft. The shaft is attached to the support of the stator with a screw and a washer on the bottom of it, in its dedicated bore.

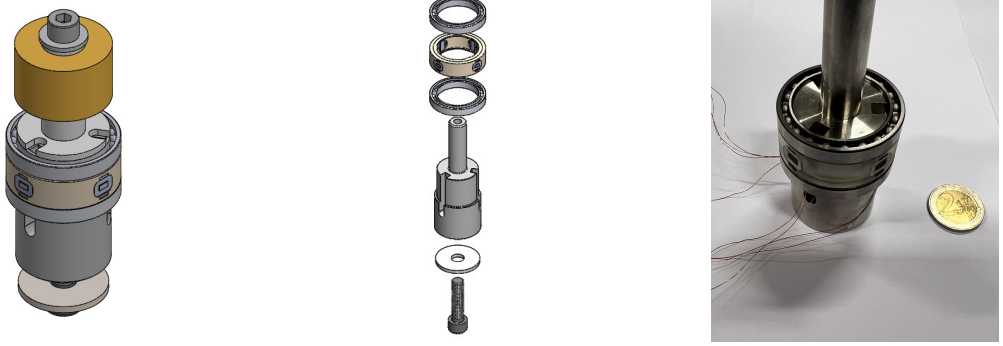

(a) (b) (c)

Figure 6.9: Shaft subassembly: (a) assembled, (b) splitted, (c) real view (partial assembly).

The shaft subassembly ensures four main functions within the global assembly. It contributes to the centering of the flywheel before it lifts off thanks to the two lift-off ball bearings, which show the largest diameter within the shaft subassembly. The outer radius of the bearings being 23.5 mm and the inner radius of the flywheel being 24.5 mm, a radial backlash of 1 mm remains. This function avoids the rotor to enter in contact with the windings when the controller is off. These bearings also have a safety function in case of malfunction. If the control of the flywheel fails, its motion would be limited by these same ball bearings. The position sensors, placed between the ball bearings, provide the position of the flywheel for its control in the x and y-directions. The operation of these sensors is described in section 6.4. The shaft also contains the armature of the motor that gives or takes energy from the flywheel.

Stator of the magnetic bearing subassembly

The stator of this SHH-AMB topology is made of two ferromagnetic hollow cylinders that surround 69 rectangular parallelepipedic permanent magnets (PMs) arranged to form a hollow cylinder as well (fig. 6.10). The PMs are polarized axially and generate the bias magnetic flux density of the bearing. The choice of using several PMs instead of a cylindrical one relates to financial reasons, a tailor-made permanent magnet being much more expensive than several existing ones. The magnets on the market that were the most suited were rectangular parallelepipedic PMs polarized along the height. The dimensions of these magnets being $10x8x21\ mm$, the model provided by the optimization was slightly modified (see L_{PM} in table 6.1 that should have been rounded to 22 mm). The grade of these PMs is N42 Neodymium magnets that offer a remanent magnetic flux density of 1.3 T. The magnet fill factor output by the optimization routine being 70 % with a remanent flux density of 1.44 T, the required number of PM is obtained by conserving the magnetic flux. The total magnetic flux in the model output by the optimization and the magnetic flux generated by one single PM are given by:

$$\begin{aligned} \phi_{tot,opti} &= 0.7 \times 1.44 \times S_{PMs} = 0.7 \times 1.44 \times \pi(R_{S,e}^2 - R_{PM,i}^2) = 7.154 \times 10^{-3}\ \text{Wb} \\ \phi_{1PM} &= 1.3 \times S_{1PM} = 1.3 \times 0.01 \times 0.008 = 1.04 \times 10^{-4}\ \text{Wb} \end{aligned} \tag{6.1}$$

where S_{PMs} and S_{1PM} are the cross-sections of all the PMs (as considered in the optimization) and of one single PM, respectively. The required number of PM $\#_{PMs}$ to generate the same magnetic flux is given by:

$$\begin{aligned} \phi_{tot,opti} &= \#_{PMs} \times \phi_{1PM} \\ \#_{PMs} &= \frac{\phi_{tot,opti}}{\phi_{1PM}} = 68.78 \approx 69\ \text{PMs} \end{aligned} \tag{6.2}$$

The two ferromagnetic rings that surround the PMs are made of steel (ST37- s235 - 1.0037), similarly to the rotor, to carry the magnetic flux density. A g6/H7 tolerance is applied to their external diameter and to the internal diameter of the support of the stator to ensure the mounting by hand. They fit inside the support of the stator with a tolerance g6/H7.

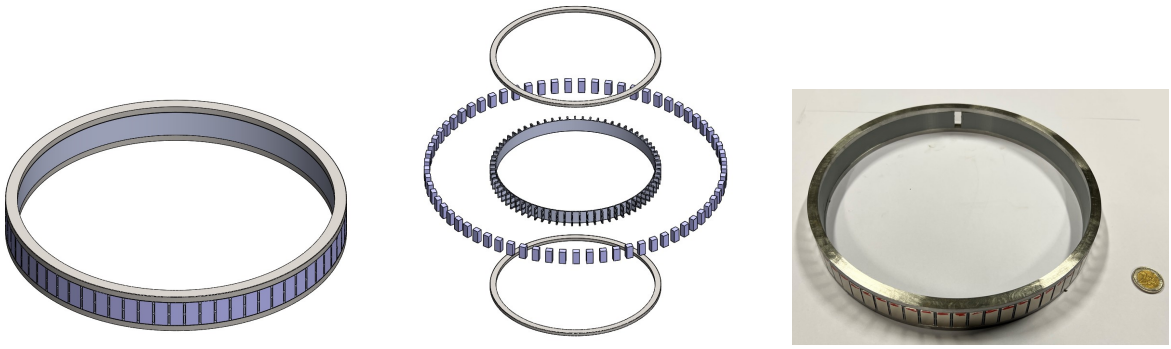

(a) (b) (c)

Figure 6.10: Stator of the magnetic bearing subassembly: (a) assembled (b) splitted (c) real view.

To place the PMs in the most uniform way, a part represented in dark gray in fig. 6.10b, is 3D printed. This part allows to uniformly separate the 69 PMs and facilitates the assembly of the PMs on the ferromagnetic rings. The distance that separates the PM to ensure the right fill-factor is just above 1 mm. To improve the resistance of such a thin part, the cross-section of the separations alternates between trapezoidal and rectangular (fig. 6.11). One of the slots of this part was cut to allow a play on the width of the last permanent magnet that has been adjusted by electrical discharge machining.

Clamping part

The clamping part is a 3D-printed part made of PLA that clamps the stator of the magnetic bearing against the support of the stator (represented in red in fig. 6.6 and 6.12). Four 3D printed PLA shims have been placed underneath (see the gray parts in fig. 6.12b) for to ensure the clamping of the stator of the magnetic bearing if the clamping part is screwed to the top of the support of the stator. The clamping part also acts as an anchor point to attach the supports of the windings.

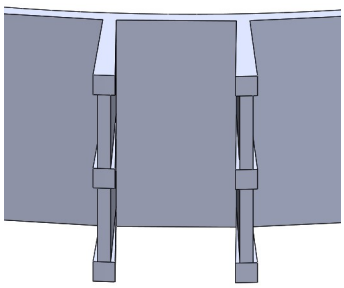

Figure 6.11: Design of the separations between PMs of the 3D printed part.

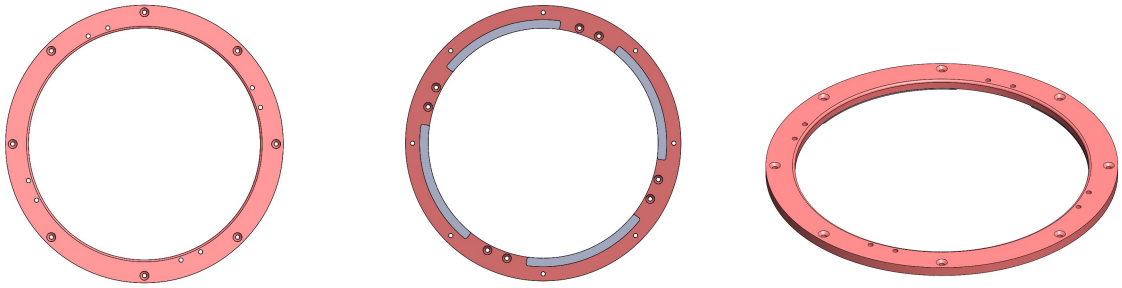

(a) (b) (c)

Figure 6.12: Clamping part: (a) top view (b) bottom view (c) isometric view.

Windings subassembly

The windings subassembly is made of a 3D printed PLA support which consists in a fourth of hollow cylinder that holds a pair of windings as shown in fig. 6.13. Each winding is made of copper wires of 1 mm of cross-section. Four of these subassemblies are employed in the model to form the windings. Each support holds a pair of windings, one on the top of its inner wall, which is aligned with the upper tooth of the rotor. The other on the bottom of its outer wall, which is aligned with the lower tooth of the rotor. The windings laying on the same support are connected in series and produce a magnetic field in opposite directions. The pair of windings that face each other are connected in anti-series so that if the circulation of the magnetic field is reinforced on one side, it is warped on the other side.

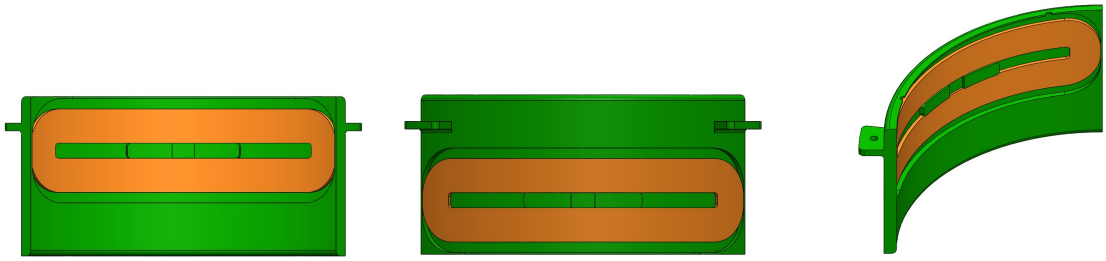

(a) (b) (c)

Figure 6.13: Windings subassembly: (a) inner view (b) outer view (c) isometric view.

The windings are glued to their support with cyanoacrylate glue. The vertical centering of the windings is ensured by a protuberance on the support that is aligned with the stator teeth. At the center of the protuberances, a recess is added to allow to solder the windings, as explained in section 6.3. Small recesses at the top of the support are also added to extract the wire ends of the windings.

6.2.3 Specific tools for assembling

To assemble and place correctly the parts previously presented, some tools have been designed and do not appear in the final assembly.

One of these tools is a 3D printed guiding arrow shown in fig. 6.14, used to orientate correctly the sensors with the windings before screwing the shaft on the support of the stator. The arrow points exactly in the middle of one of the windings if the shaft is correctly in set up (fig. 6.15).

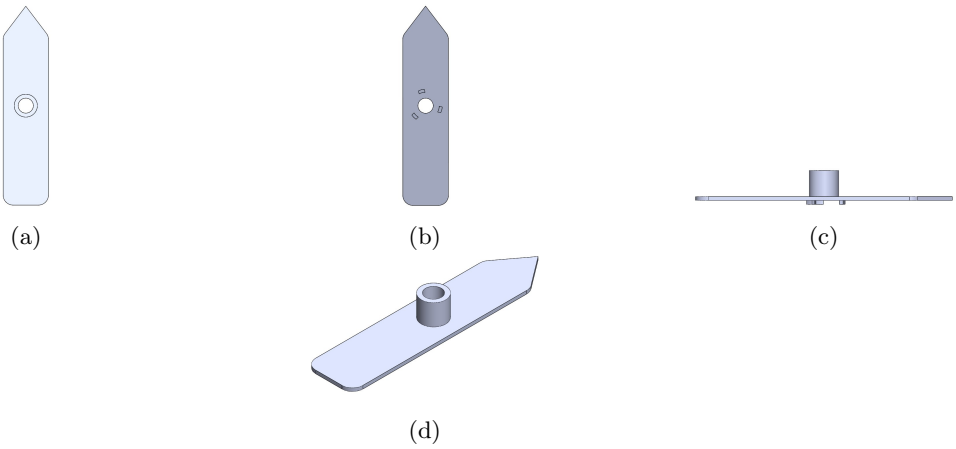

Figure 6.14: Guiding arrow: (a) top view (b) bottom view (c) side view (d) isometric view.

The second tool that has been designed is a steel cylinder, inserted on the upper tip of the shaft before installing the other elements, that allows the insertion of the rotor within the stator, as depicted in fig. 6.16. On the top, of this part, an inward point was hollowed so that the bearing extractor can be placed. To insert the flywheel, the cylinder is put on the shaft and the two claws of the bearing extractor claws the flywheel at the level of its grooves as shown in fig. 6.17. This mechanism is used for safety reasons, as the magnetic forces between the permanent magnets of the stator and the flywheel are high. This way, the flywheel is safely lowered in the stator. Moreover, it is almost impossible to remove by hand the flywheel from the stator once it is inside. This is also reversible to remove the rotor from the stator.

6.2.4 Manufacturing of the parts of the prototype

This section lists, in table 6.2, the suppliers of the prototypes parts presented in the previous sections. The mechanical drawings of the parts that have been manufactured are available in appendix D.

6.3 Windings

This section explains how the windings have been handcrafted. The required characteristics are given by the optimization (see table 6.1): each winding must have 41 turns. As the lift-off current is estimated at 3.917 A, a copper of 1 mm of diameter was selected. The windings have to be curved and fit in a restricted space due to the shape of the topology (see fig. 6.6 and table 6.1). Two layers of wire are required to fit the 41 turns in the dedicated space. Several tests have been performed to obtain the best

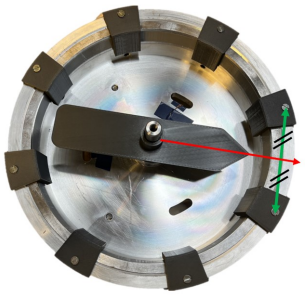

Figure 6.15: Geometrical alignment for the position sensors with the guiding arrow.

(a) (b)

Figure 6.16: Cylinder to insert and extract the flywheel: (a) 2D cut view (b) real view.

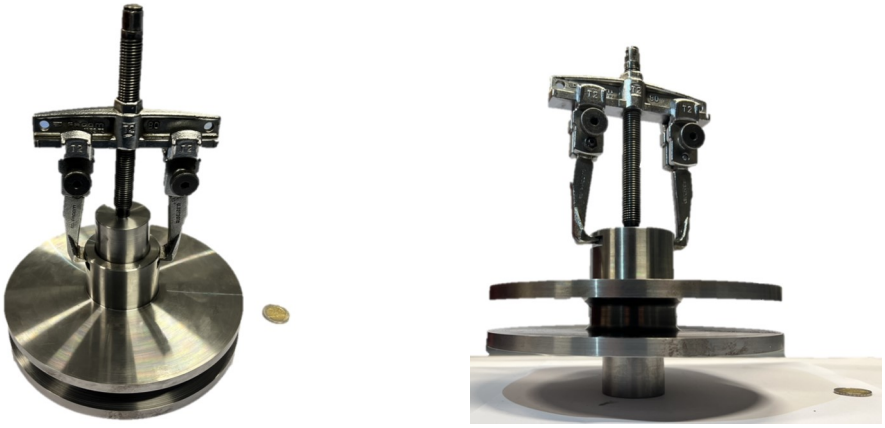

(a) (b)

Figure 6.17: Insertion and extraction of the flywheel: (a) diving view (b) lateral view.

windings results. This section only presents the solution that offers the best results, and the evolution of the winding procedure is detailed in appendix C.

The process used to build the windings consists in winding of the 41 loops at a time, and to assemble to two half windings afterward. The setup is shown in fig. 6.18a. A plate with the dimensions of the required windings (inner or outer winding) is clamped in a vise. This plate has a protuberance at its center with a height of 1 mm on which two smaller plates are screwed. These smaller plates allow clamping the wire against the main plate and avoid the natural formation of overlapping loops when they are tightened against each other. These plates do not cover the whole main plate so that glue can be applied to fix the loops between them every few turns. The resulting half winding is shown in fig. 6.18b and 6.18c. Once two half windings are formed, they are bent and glued together on their support. The electrical connection is then made by welding the cables at the center of the coils.

(a) (b) (c)

Figure 6.18: Winding method: (a) Setup to wind (b) Top view of a half winding (c) Side view of a half winding

Table 6.2: Manufacturing of the parts of the prototype.

Subassembly	Part of the prototype	Manufacturing
Rotor	Rotor	SuNPe
	Squirrel cage	SuNPe
Support the stator	Support of the stator	SuNPe
	Radial and axial soft-tip screws	Misumi
Shaft	Shaft	SuNPe
	Screws and washers	Misumi
	Aluminum spacer ring	Misumi
	Armature of induction machine	Provided by UCLouvain
	Aluminum spacer with grooves	SuNPe
	Ball bearings	Misumi
	Sensors supprt	3D printed
	Inductive sensors	Handcrafted at UCLouvain
Stator of the magnetic bearing	Ferromagnetic hollow cylinders	SuNPe
	Permanent magnets	First 4 Magnets
	PM separator	3D printed
Clamping part	Clamping part	3D printed
	Shims	3D printed
Windings	Windings supports	3D printed
	Windings	Handcrafted
Specific tools	Guiding arrow	3D printed
	Cylinder for insertion and extraction	UCLouvain
	Bearing extractor	Provided by UCLouvain

6.4 Connection diagram

This section describes the connection diagram for the test bench of the prototype. Several components are required for an AMB to operate. These elements are depicted in the connection diagram in fig. 6.19 and are detailed in this section.

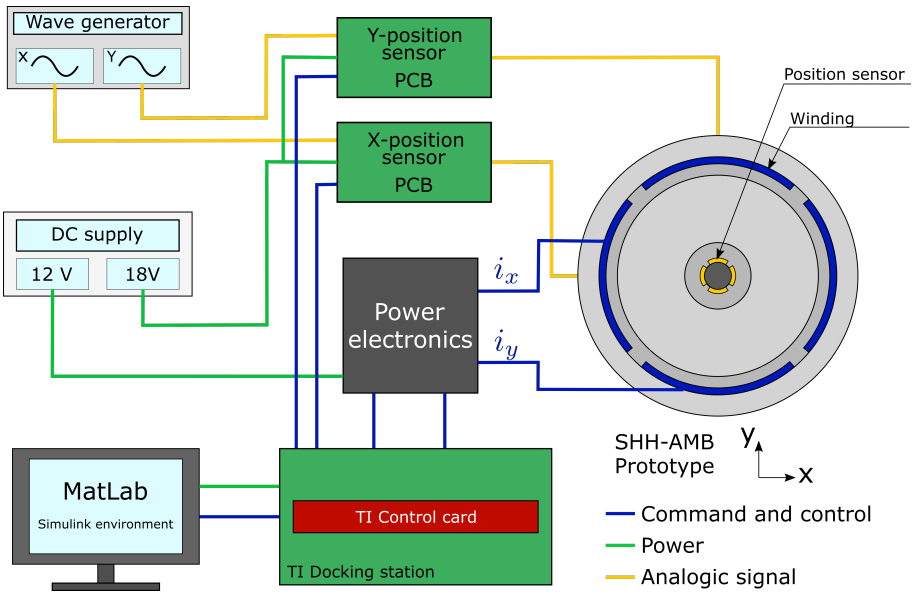

Figure 6.19: Connection diagram of the prototype.

Working principle of the prototype

The control of the prototype is based on a Matlab Simulink routine which consists in a PID controller, developed in section 6.5. This routine is either be tuned and monitored in real-time or permanently flashed in a Texas Instrument control card (TMDSCNCD28335PGF). The control card executes the instructions

of the Matlab Simulink, that was translated in a C code. This card contains analog-to-digital converters (ADC) that receive position information of the prototype, necessary for the controller. The interface between the control card and the elements connected to it is provided by a Texas Instrument docking station on which the control card is plugged. From there, the connection diagram splits into two parts: the power electronics that supplies the windings and the acquisition of the flywheel position.

The power electronics (DFRobot DC motor Driver 2x15A) is a board that modulates the power supplied to the windings of the prototype with the information received from the control card as a pulse-width modulation (PWM). It is powered by a 12V power supply, and outputs a voltage ranging from $-12V$ to $12V$ depending on the input coming from the controller. Two such bridges are present, one for each axis of actuation of the bearing.

The acquisition of the radial position of the flywheel in the xy-plane is done through two pairs of coils, one pair for each direction. Each pair is connected in a bridge (fig. 6.20), and is powered by a signal generator in A with an AC signal whose frequency and amplitude is determined experimentally to extract the most of the dynamic of the coils. The coils act as eddy-current sensors which work on the principle of electromagnetic induction: the alternating current flowing through the coils of the sensors gives rise to a varying magnetic field within the flywheel, inducing Eddy currents that alters the impedance of the coil as a function of the distance between the coil and the rotor. The change of impedance impacts the voltage of point B and the distance is retrieved with a phase lock-in amplifier (PCB sensor) that extracts the altered signal from the signal generator flowing through the coils in B and removes a part of the noise. The amplifier is powered by a 18 V DC power supply and gives a DC signal as output whose amplitude is a function of the distance, provided to the ADC of the control card.

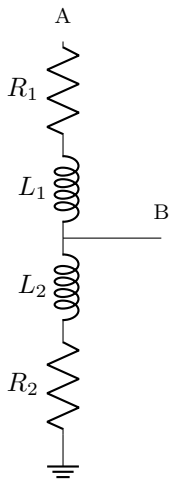

Figure 6.20: Schematic of a position sensor.

Set up of the position sensors

To calibrate the position sensors and enjoy the maximum of dynamic range possible from it, a resistance (potentiometer) in parallel with the coils and the powering signal have been tuned experimentally. The dynamic range of the sensors measure corresponds to the range of the position of the rotor that does not give rise to a saturated signal. The maximum range is limited by the PCB of the sensors, whose output is comprised between 0 and 3.3 V. The potentiometer allows tuning the offset of the sensors to match the middle of the dynamic and the centered position of the flywheel (1.65 V). To make the best use of the dynamic range, an AC signal of 0.5 V (0.75 V) at 29 kHz is generated and provided to the x-direction set of windings (y-direction). In that way, the output of the position sensor remains within its supply rails and the position of the rotor can be measured wherever it is located.

6.5 Control

This section details the control model developed for the prototype. As explained in section 1.2.4, an AMB requires a controller to ensure the stability of the flywheel. It is also demonstrated that a PID controller is required to comply with the stability criteria, which explains the use of such a controller for the prototype.

The Matlab Simulink block diagram transmitted to the control card is depicted under a block diagram in fig. 6.21. This block diagram represents the control of the x-axis and is duplicated to control the y-axis. At the bottom left, the reference voltage command of the direction, which corresponds to a centered flywheel, is compared to the signal provided by the sensor PCB through an ADC. A low-pass filter that reduces the high-frequency noise coming from the measure is added. The difference between these signals is treated by the PID controller made of:

- a proportional action modulates the output command with a constant gain K_P.
- an integral action that allows neutralizing the static error with a factor K_I.
- a derivative action to damp the motion with a constant gain K_D, required for the stability.

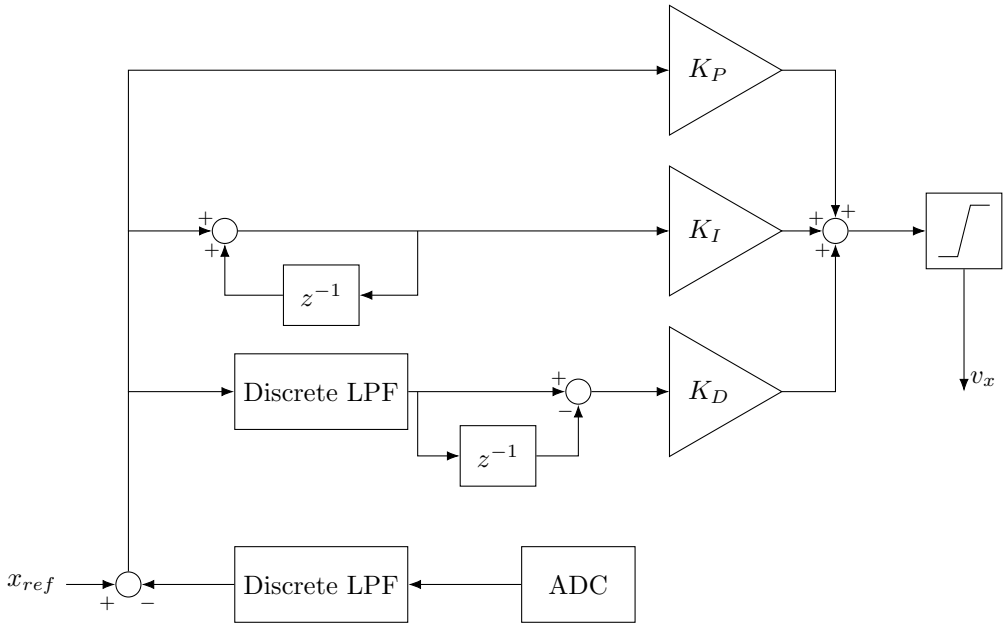

Figure 6.21: Block diagram of the PID controller used for the control of one phase of the prototype.

An additional low-pass filter is placed before the derivative action, as this latter is sensitive to high frequency noise that pollutes the output of the derivative. A saturation block at the end of the controller is also added to limit the output voltage within the supported range.

The values of the K_P and K_D gains have been estimated thanks to a one degree of freedom model, and the minimal value of K_P is obtained through the equation found in chapter 1:

$$K_P k_i - k_\epsilon > 0 \tag{6.3}$$

With the values of current and radial stiffnesses, k_i and k_ϵ, provided by the analytical and FEM models, the minimum value of K_P to stabilize the rotor is given by: $Value$. The value of K_I is first set to 0 as this action is not required for the stability, and slowly increased in real time to remove the static error on the position of the rotor.

6.6 Results

This section provides a review of the results obtained with the prototype. The objective of the prototype is to validate the results obtained with the Fourier model developed in chapter 3, and to validate the practical feasibility of such a magnetic bearing and FESS. The experimental validation of the model consists in comparing the results in terms of radial, axial, tilt and current stiffnesses. Except for the axial stiffness, the computation of these values requires the levitation of the rotor. This section explains the achievements as well as the problems encountered with the prototype, as well as the characteristics that could be measured.

Three main results were achieved with the prototype. Firstly, the axial stiffness was evaluated and corresponds to the prediction of the Fourier model. The experimental value was evaluated by measuring the equilibrium position of the rotor, and by comparing it to the weight of the rotor. The measured value of the axial stiffness is 14.017 N/mm while the FEA and the Fourier models provide a value of 14.33 and 14.321 N/mm respectively. Secondly, the good operation of the windings and the electrodynamic force has been demonstrated by injecting current in open loop in one axis at a time. With such currents, the rotor lies on the lift-off bearings, on the side corresponding to the force that is applied via the windings. Finally, using the control presented in section 6.5, a closed loop control is possible in one direction at a time. The rotor remains on the lift-off bearing, but is centered regarding the considered axis and can reject a disturbance. Despite a multitude of trials, the closed-loop control of the two axes at the same time has however not been achieved due to stability issues, making the measure of the other global characteristics not possible at this state of the work.

Several hypotheses have been put forward to explain why the control fails in its task. Firstly, an important noise component lies in the measure of the position, especially in one of the axis. It may be due to a malfunction in the corresponding phase lock-in amplifier PCB or to a problem in the sensor itself. The noise is amplified when current flows through the windings of the corresponding axis, which might relate to EMI interferences with the PWM output by the power electronics. Twisting the wires and using coaxial cables reduces the noise, but does not remove it.

The way the control is carried out can also be called into question. Voltage control has been chosen for its ease of installation. The current is thus controlled through the voltage that is applied to the windings. However, this kind of control neglects the electrical dynamic. It has been demonstrated in the literature that a robust voltage control should include the Faraday's law of induction that applies to the windings dynamics [46]. The voltage controller could thus be redesigned to take this consideration into account.

The last hypothesis concerns a phenomenon that has been observed during the tests. When the closed loop control of the two axes is tried, the rotor tends to incur significant tilt oscillations. These oscillations are explained by the parasitic torque that the current flowing through the windings produces, additionally to the desired electrodynamic force. As no tilt control is implemented to compensate for these oscillations, these latter are not damped throughout the time. This parasitic torque was evaluated with a FEA providing a significant value of 0.35 Nm.

Different solutions are considerable to comply to these problems. A first solution could be to redesign the prototype with the optimization procedure to which a constraint over the value of this parasitic torque is added. It would thus be required to evaluate the parasitic torque with the Fourier model. The prototype could be kept if a measure of the tilt position and a tilt controller is added. The current in each of the windings would thus be imposed independently of each other. The FESS could be made of two AMB, which would remove the tilt, if the centers of the rotors are well controlled.

CHAPTER 7

CONCLUSION

As a reminder, this master's thesis is based on the observation that AMBs induce iron losses that can be mitigated by using a particular topology: the hybrid homopolar slotless AMB. This improvement combined with the increasing demand for energy storage makes this topology a good candidate for FESS. As developed in chapter 1, FESS is becoming an interesting energy storage system for a lot of applications due to its performances, its flexible design and its low environmental impact. It has also been shown that control represents a major challenge for such systems. Designs of SHH-AMB have already been proposed in the literature, but none of them proposes an additional stabilization in the axial direction. However, this feature can make the system more robust to perturbation and ease the control. That is why, this thesis consisted in developing a semi-analytical model that could be used to design and characterize a SHH-AMB with an axial stabilization.

To begin this thesis, the layout of the topology under study has been described followed by a proof of concept in chapter 2. It enabled to understand the challenges of implementing such a topology. Indeed, setting up an AMB requires anticipating the behavior of the rotor to ensure its stability but also to the efficiency of the system. This process also enabled to have a global view of the elements involved to make it work. These elements are not only the parts that constitute the AMB, but also all the physical phenomena that lie behind it.

With the topology clarified, a magnetic model of the AMB has been developed in chapter 3. The aim of this model is to predict the behavior of any dimensional configuration of the topology. The proposed model is a semi-analytical model based on a Fourier approach, also known as the subdomain method. The Maxwell's equations are solved in every subdomain, to describe the magnetic flux density semi-analytically. As the model was built to be used in an optimization routine, intrinsic elements of the model were discussed to increase the computation performances. This is the case for the number of harmonics that is used to accurately evaluate the magnetic flux density distribution. By adjusting this number with the dimension of the subdomain, it allows for a relative fast and accurate computation. The conditioning of the system of equations limits the performances of the model by lowering the numerical precision of the solver. To deal with this restriction, exponentially scaled Bessel functions have been employed to increase the number of harmonics without degrading the conditioning of the system. The magnetic model has also been extended to take the radial eccentricity of the rotor into account. It allows extracting the global characteristics of the bearing related to the radial direction, which are important for its control, such as the radial, the current, and the tilt stiffnesses. The other global values which are the axial stiffness and the resistance of the windings have been determined. In parallel to the semi-analytical model, a model based on FEM has been developed. The comparison between the two models, for the same bearing parameters, gave encouraging results regarding the validity of the Fourier-based model.

To evaluate the performances of a given AMB employed as a FESS, a mechanical model has been developed in chapter 4. It was done with a view to provide evaluation criteria for an optimization routine. The axial equilibrium point of the rotor was the first characteristic to be developed, since it is used to compute other quantities. The mechanical performances that have been computed to evaluate an AMB are the speed limit of the rotor and its self-discharging time. For the speed limit, the mechanical stress within the rotor has been evaluated through a static and a fatigue design. Regarding the self-discharging time, it required to evaluate, the Joule losses due to the current in the windings as well as the aerodynamic friction due to the rotation of the rotor.

With the magnetic model and the mechanical model implemented, an optimization was performed to provide the best candidates for a prototype in chapter 5. It consisted in a multi-objective problem, with two objectives being the maximization of the self-discharging time while minimizing the total mass of the bearing. To reach these objectives, the optimization algorithm had the parameters of the bearing as lever arms. These parameters were both the geometrical and electromagnetic variables of the bearing. There

were also constraints to rule out unfeasible machines. These constraints were about the geometry, the magnetic saturation in the ferromagnetic materials, the performances required for the axial stability and the lift-off as well as the maximum rotating speed of the rotor. As output of the optimization, Pareto fronts of optimized AMB were given to allow the selection of a candidate. The selection process was based on an analysis of the parameters of the machine part of the Pareto front.

With the selected candidate out of the optimization, a prototype has been designed for the experimental validation of the magnetic model in chapter 6. The parts of the prototype as well as the elements to assemble it were first presented and discussed. Particular attention has been paid to the windings whose handcrafting has been detailed. To make the prototype work, specific equipments such as wave generators, power supplies, power electronics position sensors and a control card were required. The control card executes the controller that was designed using Matlab Simulink. Some difficulties have been encountered regarding this part of the prototype. Indeed, even if open loop and closed loop controls in one direction were possible, the controller always failed to totally lift-off the rotor. Several avenues for improvement have been proposed to solve this issue. Nevertheless, the prototype still allowed to assess the axial stiffness. This latter has been evaluated and compared to the results of the semi-analytical model with a really low error.

Although the prototype has not yet provided all the results for the experimental validation of the magnetic model, the main objectives of this master's thesis have been reached. Indeed, a FESS based on the SHH-AMB topology was designed on the basis of models to evaluate its performances and an optimization. Efforts will continue to be devoted to make the prototype works properly to present the results obtained in a conference paper for the 2023 *IEEE Energy Conversion Congress and Exposition.*

BIBLIOGRAPHY

[1] W. Zhang and H. Zhu, "Radial magnetic bearings: An overview," *Results in Physics*, vol. 7, p. 3756–3766, 2017.

[2] F. Jiancheng, W. Xi, W. Tong, T. Enqiong, and F. Yahong, "Homopolar 2-pole radial permanent-magnet biased magnetic bearing with low rotating loss," *IEEE Transactions on Magnetics*, vol. 48, no. 8, p. 2293–2303, Aug 2012.

[3] G. Colinet and B. Dehez, "Investigations on a new slotless homopolar hybrid active magnetic bearing," *Dial UCLouvain*, 2017.

[4] P. Tsao, S. Sanders, and G. Risk, "A self-sensing homopolar magnetic bearing: analysis and experimental results," in *Conference Record of the 1999 IEEE Industry Applications Conference. Thirty-Forth IAS Annual Meeting (Cat. No.99CH36370)*, vol. 4. Phoenix, AZ, USA: IEEE, 1999, p. 2560–2565. [Online]. Available: http://ieeexplore.ieee.org/document/799200/

[5] G. Colinet and B. Dehez, "Modeling of magnetic field distribution in slotless homopolar active magnetic bearing with eccentricity using fourier analysis."

[6] M. E. Amiryar and K. R. Pullen, "A review of flywheel energy storage system technologies and their applications," *Applied Sciences*, vol. 7, no. 3, 2017. [Online]. Available: https://www.mdpi.com/2076-3417/7/3/286

[7] A. Olabi, C. Onumaegbu, T. Wilberforce, M. Ramadan, M. A. Abdelkareem, and A. H. Al – Alami, "Critical review of energy storage systems," *Energy*, vol. 214, p. 118987, 2021. [Online]. Available: https://www.sciencedirect.com/science/article/pii/S0360544220320946

[8] S. Sabihuddin, A. Kiprakis, and M. Mueller, "A numerical and graphical review of energy storage technologies," *Energies*, vol. 8, no. 1, p. 172–216, 2014. [Online]. Available: https://dx.doi.org/10.3390/en8010172

[9] M. S. Guney and Y. Tepe, "Classification and assessment of energy storage systems," *Renewable and Sustainable Energy Reviews*, vol. 75, pp. 1187–1197, 2017. [Online]. Available: https://www.sciencedirect.com/science/article/pii/S1364032116308218

[10] X. Li and A. Palazzolo, "A review of flywheel energy storage systems: state of the art and opportunities," *Journal of Energy Storage*, vol. 46, p. 103576, Feb 2022.

[11] A. G. Olabi, T. Wilberforce, M. A. Abdelkareem, and M. Ramadan, "Critical review of flywheel energy storage system," *Energies*, vol. 14, no. 8, 2021. [Online]. Available: https://www.mdpi.com/1996-1073/14/8/2159

[12] C. K. Das, O. Bass, G. Kothapalli, T. S. Mahmoud, and D. Habibi, "Overview of energy storage systems in distribution networks: Placement, sizing, operation, and power quality," *Renewable and Sustainable Energy Reviews*, vol. 91, pp. 1205–1230, 2018. [Online]. Available: https://www.sciencedirect.com/science/article/pii/S1364032118301606

[13] M. K. Khawaja, A. Alkhalidi, and S. Mansour, "Environmental impacts of energy storage waste and regional legislation to curtail their effects – highlighting the status in jordan," *Journal of Energy Storage*, vol. 26, p. 100919, 2019. [Online]. Available: https://www.sciencedirect.com/science/article/pii/S2352152X19304815

[14] P. Kokkotis, C. Psomopoulos, G. Ioannidis, and S. KAMINARIS, "Small scale energy storage systems. a short review in their potential environmental impact," *Fresenius Environmental Bulletin*, vol. Volume 26, pp. 5658–5665, 09 2017.

[15] A. Evans, V. Strezov, and T. J. Evans, "Assessment of utility energy storage options for increased renewable energy penetration," *Renewable and Sustainable Energy Reviews*, vol. 16, no. 6, pp. 4141–4147, 2012. [Online]. Available: https://www.sciencedirect.com/science/article/pii/S1364032112002316

[16] R. Weissbach, G. Karady, and R. Farmer, "A combined uninterruptible power supply and dynamic voltage compensator using a flywheel energy storage system," *IEEE Transactions on Power Delivery*, vol. 16, no. 2, pp. 265–270, 2001.

[17] B. Amel, Z. Soraya, and C. Abdelkader, "Intelligent control of flywheel energy storage system associated with the wind generator for uninterrupted power supply," *International Journal of Power Electronics and Drive Systems*, vol. 11, no. 4, p. 2062, 2020.

[18] E. Elbouchikhi, Y. Amirat, G. Feld, M. Benbouzid, and Z. Zhou, "A lab-scale flywheel energy storage system: Control strategy and domestic applications," *Energies*, vol. 13, no. 3, 2020. [Online]. Available: https://www.mdpi.com/1996-1073/13/3/653

[19] L. V. Truong, F. J. Wolff, and N. V. Dravid, "Simulation of flywheel electrical system for aerospace applications," in *Collection of Technical Papers. 35th Intersociety Energy Conversion Engineering Conference and Exhibit (IECEC)(Cat. No. 00CH37022)*, vol. 1. IEEE, 2000, pp. 601–608.

[20] S. Sabihuddin, A. E. Kiprakis, and M. Mueller, "A numerical and graphical review of energy storage technologies," *Energies*, vol. 8, no. 1, pp. 172–216, 2014.

[21] M. Hedlund, J. Lundin, J. De Santiago, J. Abrahamsson, and H. Bernhoff, "Flywheel energy storage for automotive applications," *Energies*, vol. 8, no. 10, pp. 10 636–10 663, 2015. [Online]. Available: https://www.mdpi.com/1996-1073/8/10/10636

[22] X. Liu and K. Li, "Energy storage devices in electrified railway systems: A review," *Transportation safety and environment*, vol. 2, no. 3, pp. 183–201, 2020.

[23] P. Schöggl, A. Haimann, and L. Ress, "Hybrid in motorsports," *ATZ worldwide eMagazine*, vol. 113, no. 2, pp. 40–45, 2011.

[24] B. Sun, T. Dragičević, F. D. Freijedo, J. C. Vasquez, and J. M. Guerrero, "A control algorithm for electric vehicle fast charging stations equipped with flywheel energy storage systems," *IEEE Transactions on Power Electronics*, vol. 31, no. 9, pp. 6674–6685, 2015.

[25] M. E. Amiryar, K. R. Pullen, and D. Nankoo, "Development of a high-fidelity model for an electrically driven energy storage flywheel suitable for small scale residential applications," *Applied Sciences*, vol. 8, no. 3, 2018. [Online]. Available: https://www.mdpi.com/2076-3417/8/3/453

[26] M. A. Conteh and E. C. Nsofor, "Composite flywheel material design for high-speed energy storage," *Journal of applied research and technology*, vol. 14, no. 3, pp. 184–190, 2016.

[27] K. M. M. Robert C. Juvinal, *Fundamentals of Machine Component Design, chap. 8, Fatigue*, 7th ed. Wiley.

[28] "Roymech.org rotating disks and cylinders," https://roymech.org/Useful_Tables/Mechanics/Rotating_cylinders.html, accessed: 2023-05-06.

[29] A. K. Arani, H. Karami, G. Gharehpetian, and M. Hejazi, "Review of flywheel energy storage systems structures and applications in power systems and microgrids," *Renewable and Sustainable Energy Reviews*, vol. 69, pp. 9–18, 2017. [Online]. Available: https://www.sciencedirect.com/science/article/pii/S1364032116309054

[30] R. Sebastián and R. Peña Alzola, "Flywheel energy storage systems: Review and simulation for an isolated wind power system," *Renewable and Sustainable Energy Reviews*, vol. 16, no. 9, pp. 6803–6813, 2012. [Online]. Available: https://www.sciencedirect.com/science/article/pii/S1364032112004777

[31] P. Tsao, M. Senesky, and S. Sanders, "A synchronous homopolar machine for high-speed applications," in *Conference Record of the 2002 IEEE Industry Applications Conference. 37th IAS Annual Meeting (Cat. No.02CH37344)*, vol. 1, 2002, pp. 406–416 vol.1.

[32] N. Tănase and A. M. Morega, "Passive magnetic bearings for flywheel energy storage-numerical design. passive magnetic bearings design," in *2014 International Conference on Applied and Theoretical Electricity (ICATE)*. IEEE, 2014, pp. 1–4.

[33] H.-J. Hu, K. Liu, H. Wang, and J.-B. Wei, "A wide bandwidth gan switching power amplifier of active magnetic bearing for a flywheel energy storage system," *IEEE Transactions on Power Electronics*, vol. 38, no. 2, pp. 2589–2605, 2022.

[34] M. Strasik, P. E. Johnson, A. Day, J. Mittleider, M. Higgins, J. Edwards, J. Schindler, K. McCrary, C. McIver, D. Carlson *et al.*, "Design, fabrication, and test of a 5-kwh/100-kw flywheel energy storage utilizing a high-temperature superconducting bearing," *IEEE transactions on applied superconductivity*, vol. 17, no. 2, pp. 2133–2137, 2007.

[35] K. Hameyer, U. Palmer, D. Dolinar, and G. Stumberger, "Optimization of radial active magnetic bearings using the finite element technique and the differential evolution algorithm," *IEEE Transactions on Magnetics*, vol. 36, no. 4, p. 1009–1013, Jul 2000.

[36] R. Ravaud, G. Lemarquand, and V. Lemarquand, "Force and stiffness of passive magnetic bearings using permanent magnets. part 1: Axial magnetization," *IEEE Transactions on Magnetics*, vol. 45, no. 7, pp. 2996–3002, 2009.

[37] G. Burnand, A. Thabuis, D. M. Araujo, and Y. Perriard, "Novel optimized shape and topology for slotless windings in bldc machines," *IEEE Transactions on Industry Applications*, vol. 56, no. 2, p. 1275–1283, Mar 2020.

[38] "Maxon maxon motor hits the right note," https://www.maxongroup.com/maxon/view/application/maxon-motor-hits-the-right-note, accessed: 2023-05-31.

[39] B. Dehez, F. Baudart, M. Markovic, and Y. Perriard, "Theoretical and experimental investigation of flex-pcb air-gap windings in slotless bldc machines," *IEEE Transactions on Industry Applications*, vol. 50, no. 5, p. 3153–3160, Sep 2014.

[40] A. Chiba, *Magnetic bearing controllers*. Elsevier, 2005, p. 45–84. [Online]. Available: https://linkinghub.elsevier.com/retrieve/pii/B9780750657273500067

[41] C. Guillaume and D. Bruno, "Influence of end winding configuration on the performance of slotless homopolar hybrid active magnetic bearings," in *2021 24th International Conference on Electrical Machines and Systems (ICEMS)*. Gyeongju, Korea, Republic of: IEEE, Oct 2021, p. 530–535. [Online]. Available: https://ieeexplore.ieee.org/document/9634351/

[42] B. L. J. Gysen, K. J. Meessen, J. J. H. Paulides, and E. A. Lomonova, "General formulation of the electromagnetic field distribution in machines and devices using fourier analysis," *IEEE Transactions on Magnetics*, vol. 46, no. 1, pp. 39–52, 2010.

[43] B. Hannon, P. Sergeant, L. Dupre, and P.-D. Pfister, "Two-dimensional fourier-based modeling of electric machines—an overview," *IEEE Transactions on Magnetics*, vol. 55, no. 10, p. 1–17, Oct 2019.

[44] "Universal balancing iso 21940 balance g grades," https://www.universal-balancing.com/en/resources/iso-21940-g-grades/, accessed: 2023-05-10.

[45] V. Kluyskens, "Thermal model for a low-speed flywheel in low vacuum."

[46] S.-L. Chen and C.-C. Weng, "Robust control of a voltage-controlled three-pole active magnetic bearing system," *IEEE/ASME Transactions on Mechatronics*, vol. 15, no. 3, pp. 381–388, 2010.

APPENDIX A

COMPLIANCE TO THE BOUNDARY CONDITIONS

This chapter demonstrates the well-functionning of the Fourier based model by verifying the compliance of the solution to the boundary conditions developed in chapter 3. The machine used for this validation is the test machine modeled with 20 harmonics in region II (equivalent to FB20).

A.1 Full Neumann boundary condition

Fig. A.1 shows the graph of the axial magnetic flux density in region II at $r = R_{R,i}$. To fulfill the Neumann boundary condition, the magnetic flux density should be equal to 0. The graph shows that the value oscillates between 4×10^{-18} and -4×10^{-18} which can be assimilated to numerical noise. The solution complies thus to the boundary condition.

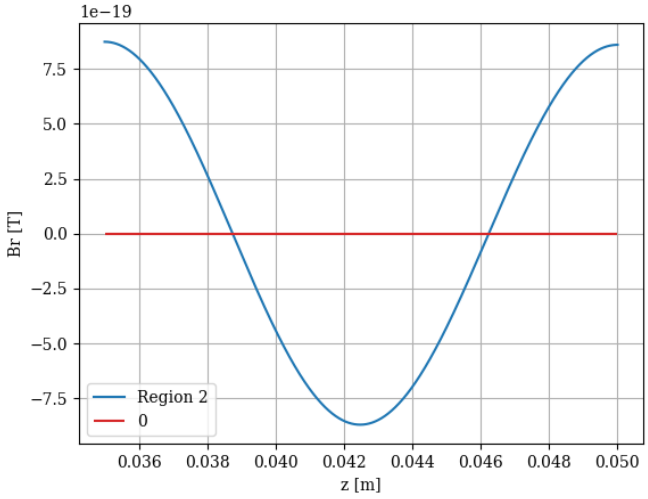

Figure A.1: Axial magnetic flux density of region II at $r = R_{R,i}$. The y-axis is scaled up by 10^{18}.

A.2 Full continuous boundary condition

The continuity between region V and VI is such that the radial magnetic flux density and the axial magnetic strength are equals at $r = R_{PM,i}$ in both regions. Fig. A.2 shows that these two quantities are indeed equal to each other, and validates the compliance of the solution to the boundary condition.

A.3 Combination of Neumann and continuous boundary conditions

A.3.1 $r = R_{R,e}$

This condition ensures the continuity of the radial magnetic flux density and the axial magnetic strength between region III and I and between III and II as well as the zero axial component of the magnetic flux density on the two rotor iron teeth. Fig. A.3 shows the concerned quantities along the period of the

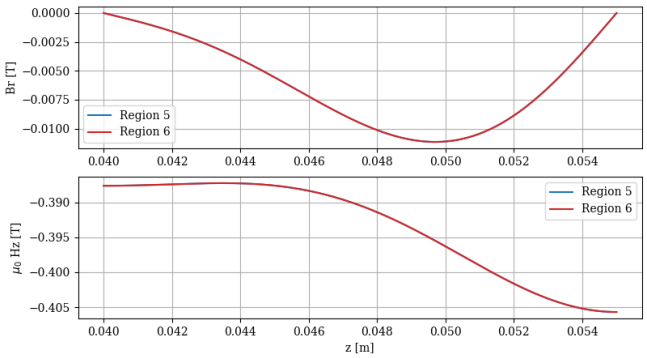

Figure A.2: Radial magnetic flux density (upper) and axial magnetic strength (lower) of regions V and VI at $r = R_{R,i}$

model at $r = R_{R,e}$. The radial magnetic flux densitie and axial magnetic strength of region I and II seem to match the curve of region III where it is required. The difficulty to reach the continuity is visible on the radial magnetic flux density of regions I and II at the begining of the iron teeth. The axial magnetic strength is indeed equal to zero on the rotor iron teeth. The oscillations of the curves shows that the compliance to this boundary condition strongly depends on the number of harmonics that is employed in each region.

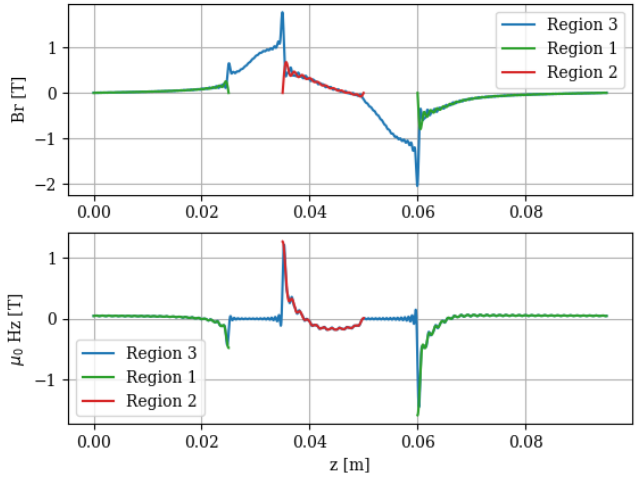

Figure A.3: Radial magnetic flux density (upper) and axial magnetic strength (lower) of region I, II and III at $r = R_{R,e}$.

A.3.2 $r = R_{S,i}$ and $r = R_{S,e}$

The same observations are made for the condition applied between region IV, V and III at $r = R_{s,i}$ (fig. A.4 and A.5).

A.4 Dirichlet's condition

Fig. A.6 shows the radial magnetic flux density of region I at $r = R_{R,d}$ that is imposed at zero by the Dirichlet's condition. Similarly to what is observed for the Neumann conditon, the order of magnitude of the solution is 10^{-18} which is assimilated to numerical noise. The condition is thus fulfilled.

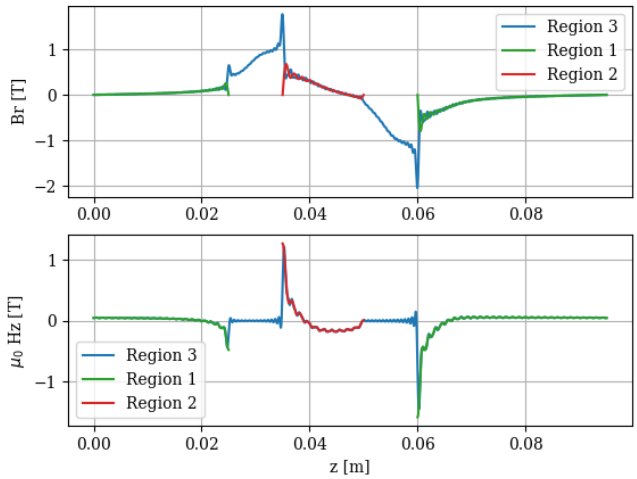

Figure A.4: Radial magnetic flux density (upper) and axial magnetic strength (lower) of regions IV, V and III at $r = R_{S,i}$.

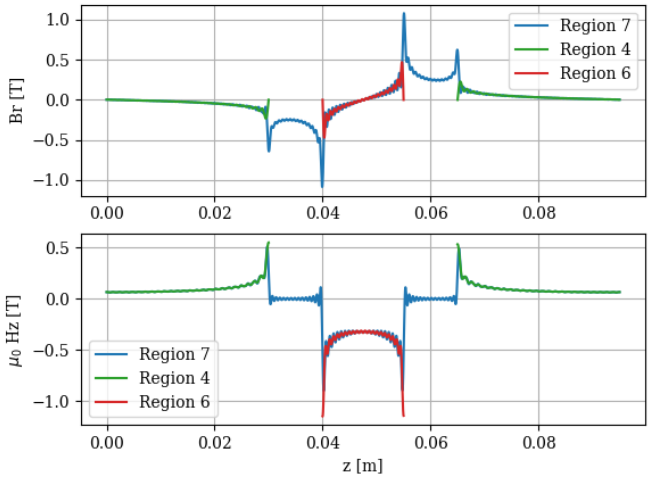

Figure A.5: Radial magnetic flux density (upper) and axial magnetic strength (lower) of regions IV, VI and VII at $r = R_{S,e}$.

A.5 Ampere's law

The three Ampere's law applied to three paths are verified by computing the value associated to the equation that that should be equal to 0. Table A.1 shows the values for the three equations, which are either exactly equal to 0 or have an order of magntiude of 10^{-17}, which corresponds to numerical noise. The condition is thus indeed fulfilled.

A.6 Magnetic flux conservation

The conservation of the magnetic flux around the concerned stator iron tooth is verified by integrating numerically the magnetic flux density around the iron tooth in each region. The sum of these fluxes is expected to be equal to 0. Table A.2 shows the magnetic fluxes entering the iron tooth from region III, IV, V, VI and VII, as well as their sum. As the total magnetic flux has an order of magnitude of 10^{-16}, which corresponds to numerical noise, the condition is fulfilled.

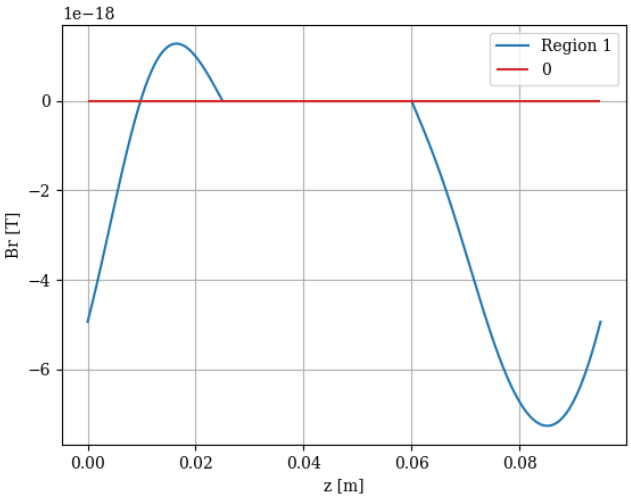

Figure A.6: Radial magnetic flux density of region I at $r = R_{R,d}$. The y-axis is scaled up by 10^{18}.

Table A.1: Verification of the compliance to the Ampere's law

Radius r	Value
$R_{R,e}$	-5.49×10^{-17}
$R_{S,i}$	0.0
$R_{S,e}$	-9.02×10^{-17}

Table A.2: Verification of the compliance to the magnetic flux conservation

Region	ϕ (Wb)
III	0.0038839221088559583
IV	0.0035784381605941766
V	0.002196036432258397
VI	−0.011889775764775045
VII	0.002231379063066629
Sum	$1.1622647289044608 \times 10^{-16}$

APPENDIX B

MECHANICAL STRESS IN A ROTATING HOLLOW CYLINDER

The mechanical stress in the rotating hollow cylinder is obtained considering an infinitesimal angular sector (see fig. B.1) of angular opening $d\theta$, radial width dr, and located in (r, θ). The deformation of such an angular sector incurring the stress appearing with the rotation is illustrated in fig. B.2 as well as the notation that are employed in the following developments. The axial stress in the cylinder σ_z is assumed to remain constant such that the cross-section remains planar. The equations linking the mechanical stresses σ to the deformation vector ϵ are given by:

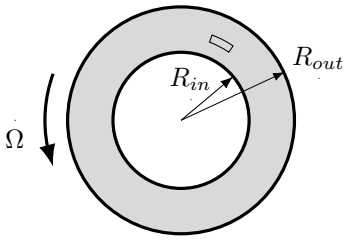

Figure B.1: Hollow cylinder considered for the stress computation.

$$\begin{aligned} E\epsilon_z &= \sigma_z - \nu\sigma_\theta - \nu\sigma_r \\ E\epsilon_\theta &= E\frac{u}{r} = \sigma_\theta - \nu\sigma_z - \nu\sigma_r \\ E\epsilon_r &= E\frac{du}{dr} = \sigma_r - \nu\sigma_\theta - \nu\sigma_z \end{aligned} \tag{B.1}$$

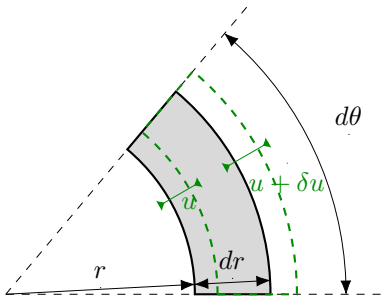

Figure B.2: Infinitesimal angular sector of the hollow cylinder and its deformation due to the mechanical stresses in rotation.

where ϵ is the strain, E is the Young modulus and ν is the Poisson's coefficient. The second line is multiplied by r and differentiated with respect to r and equalled to the third line, giving rise to:

$$(\sigma_\theta - \sigma_r)(1+\nu) + r\frac{d\sigma_\theta}{dr} - r\nu\frac{d\sigma_z}{dr} - r\nu\frac{d\sigma_r}{dr} = 0 \tag{B.2}$$

As ϵ_z is constant, the first line of eq. B.1 gives after derivation:

$$\frac{d\sigma_z}{dr} = \nu(\frac{d\sigma_\theta}{dr} + \frac{d\sigma_r}{dr}) \tag{B.3}$$

and eq. B.2 becomes:

$$(\sigma_\theta - \sigma_r) + r(1-\nu)\frac{d\sigma_\theta}{dr} - r\nu\frac{d\sigma_r}{dr} = 0 \tag{B.4}$$

The force equilibrium for an infinitesimal cross-section is considered and illustrated in fig. B.3.

The force equilibrium provides the following equation:

$$2\sigma_\theta dr\sin(\frac{d\theta}{2}) + \sigma_r r d\theta - (\sigma_r + d\sigma_r)(r+dr)d\theta = \rho r^2\Omega^2 dr d\theta \tag{B.5}$$

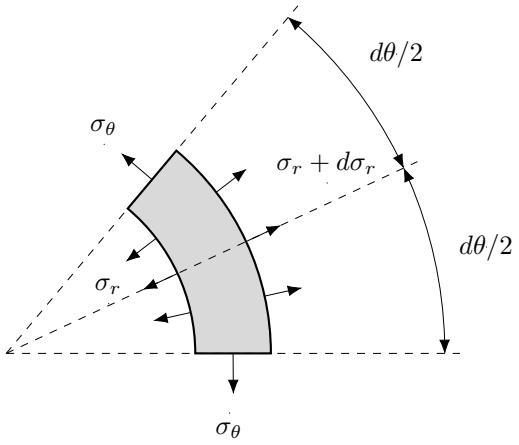

Figure B.3: Mechanical stress applied on the infinitesimal angular sector.

The following mathematical developments are then performed to obtain the general form of the solution for σ_r and σ_θ.

$$\begin{aligned}
&\sigma_\theta - \sigma_r - r\frac{d\sigma_r}{dr} = \rho r^2\Omega^2 \\
\iff &\frac{d\sigma_\theta}{dr} + \frac{d\sigma_r}{dr} = \frac{-\rho r\Omega^2}{1-\nu} \\
\iff &\sigma_\theta + \sigma_r = \frac{-\rho r^2\Omega^2}{2(1-\nu)} + K_1 \\
\iff &2\sigma_r + r\frac{d\sigma_r}{dr} = K_1 - \rho r^2\Omega^2 - \frac{\rho r^2\Omega^2}{2(1-\nu)} \\
\iff &\frac{d(\sigma_r r^2)}{dr} = K_1 r - \frac{\rho r^3\Omega^2(3-2\nu)}{2(1-\nu)} \\
\iff &\sigma_r = \frac{-\rho r^2\Omega^2(3-2\nu)}{8(1-\nu)} + \frac{K_1}{2} - \frac{K_2}{r^2} \\
\iff &\sigma_\theta = \frac{-\rho r^2\Omega^2(1+2\nu)}{8(1-\nu)} + \frac{K_1}{2} + \frac{K_2}{r^2}
\end{aligned} \tag{B.6}$$

The values of K_1 and K_2 are obtained by applying the limit conditions. The inner and outer surfaces of the ring being free to deform themselves, the radial stress on these surfaces is imposed to zero giving the final values of the two unknowns that are injected in the expression of the stresses.

$$K_1 = \frac{\rho\Omega^2(3-2\nu)}{4(1-\nu)}(R_{out}^2 + R_{in}^2) \tag{B.7}$$

$$K_2 = \frac{\rho\Omega^2(3-2\nu)}{8(1-\nu)}R_{out}^2 R_{in}^2 \tag{B.8}$$

APPENDIX C

TRIED MANUFACTURING PROCESSES FOR HANDCRAFTED WINDINGS

This appendix explains the problems encountered during the manufacturing of the windings of the prototype. As mentioned in section 6.3, it took several tries before finding the method that provide acceptable results. Before that, four different methods have been tried and are described in this chapter.

The first method tried involved winding the cable directly bent between two curved plates with a guiding element at the center. See fig. C.1 for the setup of this method. The two curved plates are clamped together by bolts. To fix the wires between them, silicone glue was used. This method encountered several issues. Firstly, it was difficult to wind two layers curved at the same time, since the outer one always wanted to go over the inner layer. Moreover, the transition between an inner and outer layer was taking space and increased the height of the winding. Finally, the silicone glue was not strong enough to keep the wire together and too thick also resulting in a too large winding height. The resulting winding using this method can be observed in fig. C.5a.

Figure C.1: First method: winding between two curved plates

The second method is quite similar to the first, except that the winding operation is realized between two flat plates (see fig. C.2). Indeed, the copper wire is flexible enough to be bent after being winded and so even if there is the presence of glue. This time, cyanoacrylate has also been used between the loops instead of silicone glue and gave a more convincing result. The problem with this method is that the wire was pushing on the plates since the space between them was exactly 2 mm which was theoretically just enough for the two layers of copper wire desired. However, when pushing the loops against each other to squeeze them as tightly as possible, they had the tendency to form a third and even sometimes a fourth layer of copper wire by deforming the 3D printed plates in PLA. The winding resulting from this method is shown in fig. C.5b.

Considering the problems of the methods previously tried, it was chosen to wind only one layer at the time and repeat the operation twice to have two half windings that can be glue and solder to form one winding. The setup is almost the same as the second method (see fig. C.2), but this time, two flat plates with just above 1 mm of space between them were used as shown in fig. C.3. This way, there was less constraint from the wire against the plates, but the problem is that it was impossible to properly applied

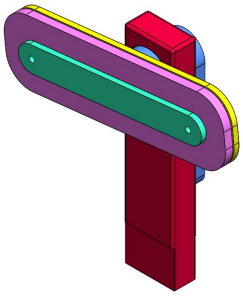

Figure C.2: Second method: winding between two flat plates

glue since the space was too tight. It resulted in a winding that unwound itself when the plates were loosened, as shown in fig. C.5c.

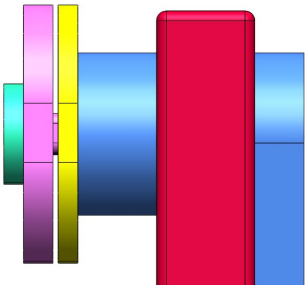

Figure C.3: Third method: reducing the space between the flat plates compared to the second method

The fourth method is based on the previous one, but this time notches have been designed in one of the plates (see fig. C.4) for glue application. This method was working relatively well until the separation of the plates. At this time, the glue had already dried between the loops but also between the loops and one plate, and it was then impossible to separate the winding from that plate as depicted in fig. C.5d. Moreover, it was also more difficult to tight the loops between them due to the notches where the pushing tool was deflected.

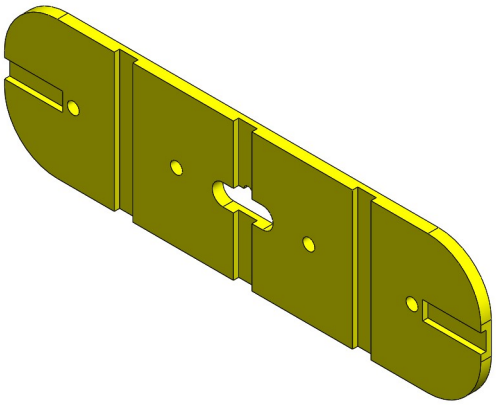

Figure C.4: Fourth method: similar to third method but with notches for glue application

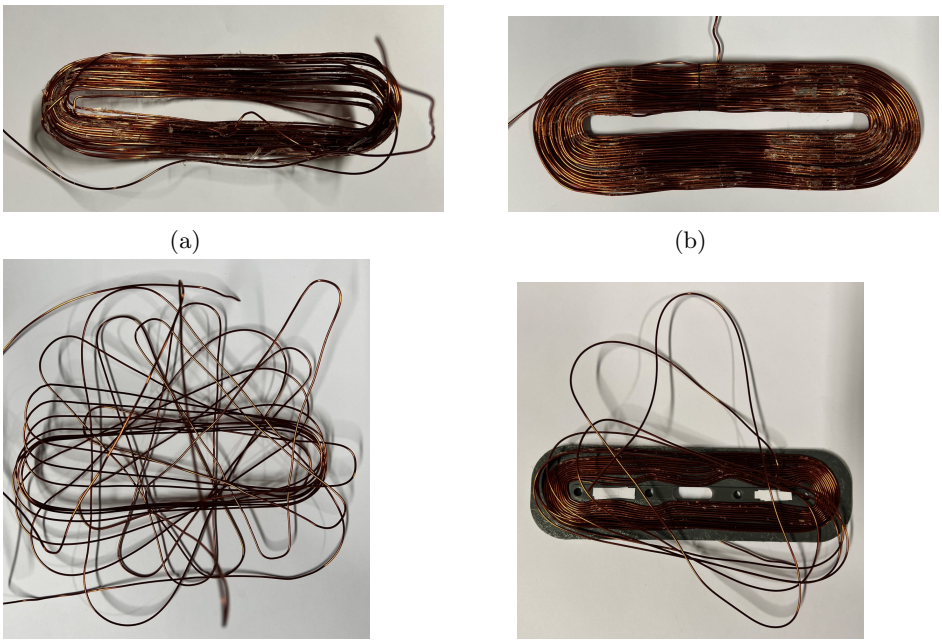

(a) (b)

(c) (d)

Figure C.5: Resulting windings from the different methods: (a) first method (b) second method (c) third method (d) fourth method

APPENDIX D

DRAWINGS

This appendix presents the mechanical drawings used for the manufacture of the parts of the prototype. The drawings appears in the following order:

- Rotor of the bearing
- Stator rings of the bearing
- Support of the stator
- Shaft
- Washer with holes for the cables
- Squirrel cage
- Cylinder used for the installation of the rotor

COUPE A-A

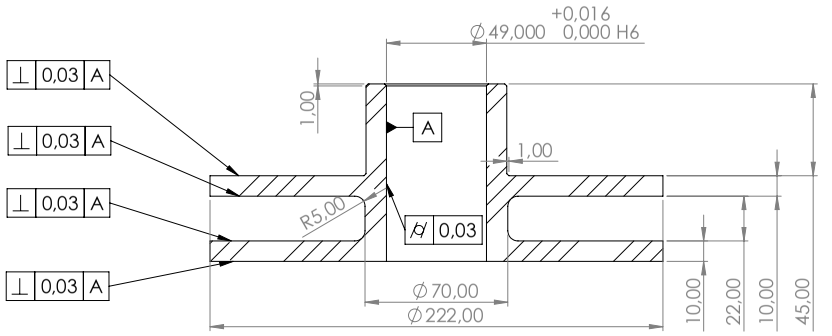

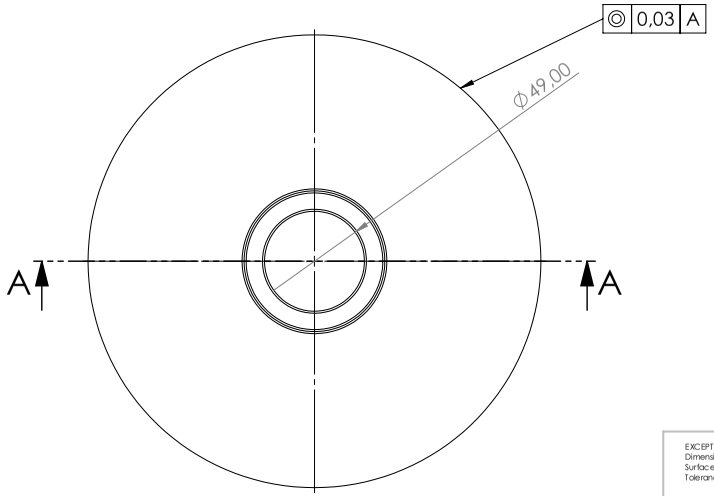

EXCEPT IF INDICATED : Dimensions are in millimeters Surface finish : Tolerances: ISO22081	FINITION:				DO NOT CHANGE THE SCALE	REVISION
	NAME	FIRSTNAME	DATE		TITLE:	
AUTHORS	BOULANGER	François	29/03/2023		Rotor	
	BOSSCHAERT	Sébastien	29/03/2023			
VERIF.						
APPR.						
FAB.				MATERIAL:	Number of plan	A3
QUAL.				ST37 - s235 - 1.0037	3	
				MASS: 6.750 kg	SCALE:1:2	SHEET 1 OF 1

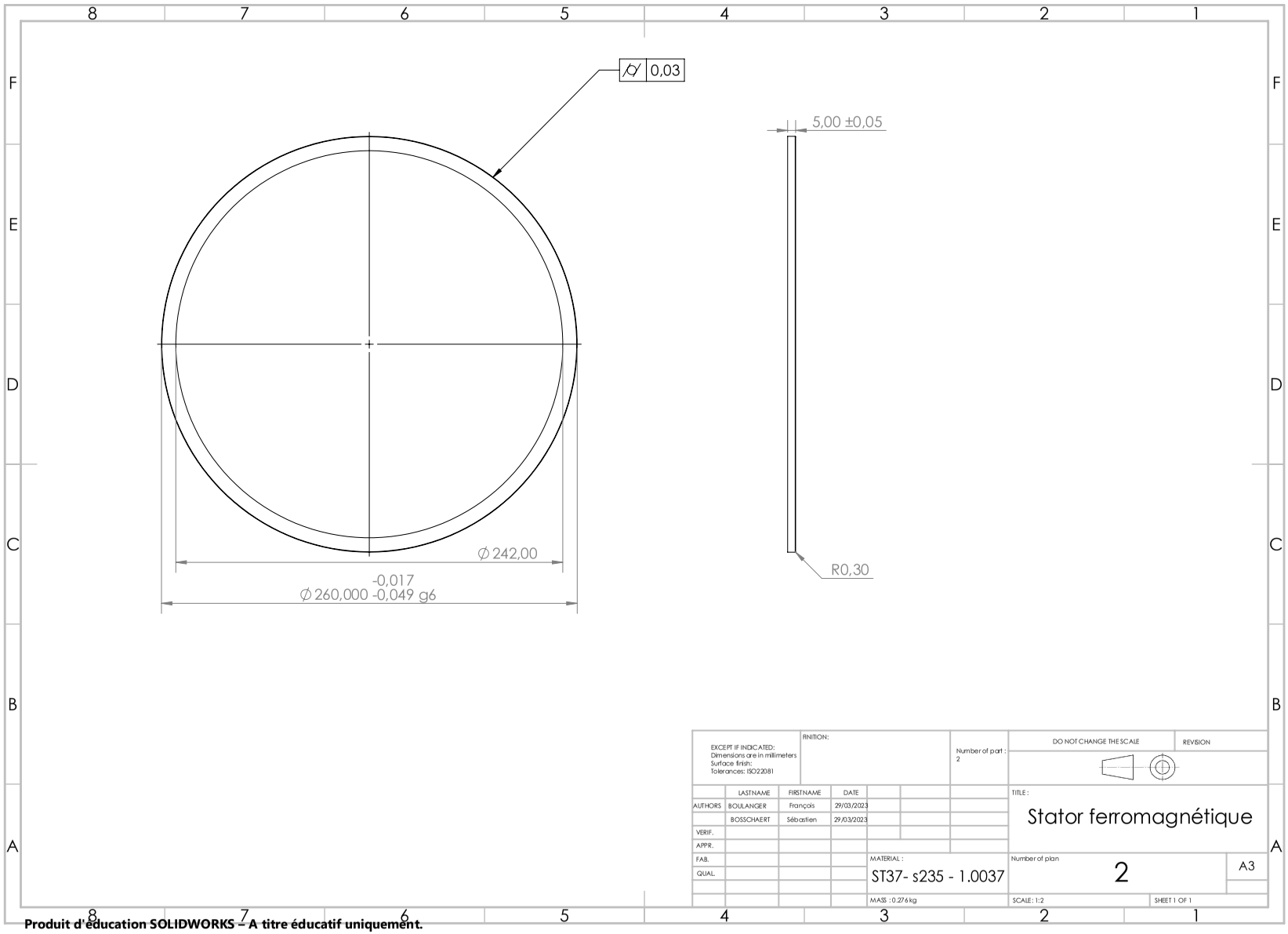

EXCEPT IF INDICATED: Dimensions are in millimeters Surface finish: Tolerances: ISO22081	FINITION:				Number of part : 2	DO NOT CHANGE THE SCALE / REVISION
	LASTNAME	FIRSTNAME	DATE			TITLE : Stator ferromagnétique
AUTHORS	BOULANGER	François	29/03/2023			
	BOSSCHAERT	Sébastien	29/03/2023			
VERIF.						
APPR.						
FAB.				MATERIAL : ST37- s235 - 1.0037		Number of plan 2 / A3
QUAL.						
				MASS : 0.276 kg		SCALE: 1:2 / SHEET 1 OF 1

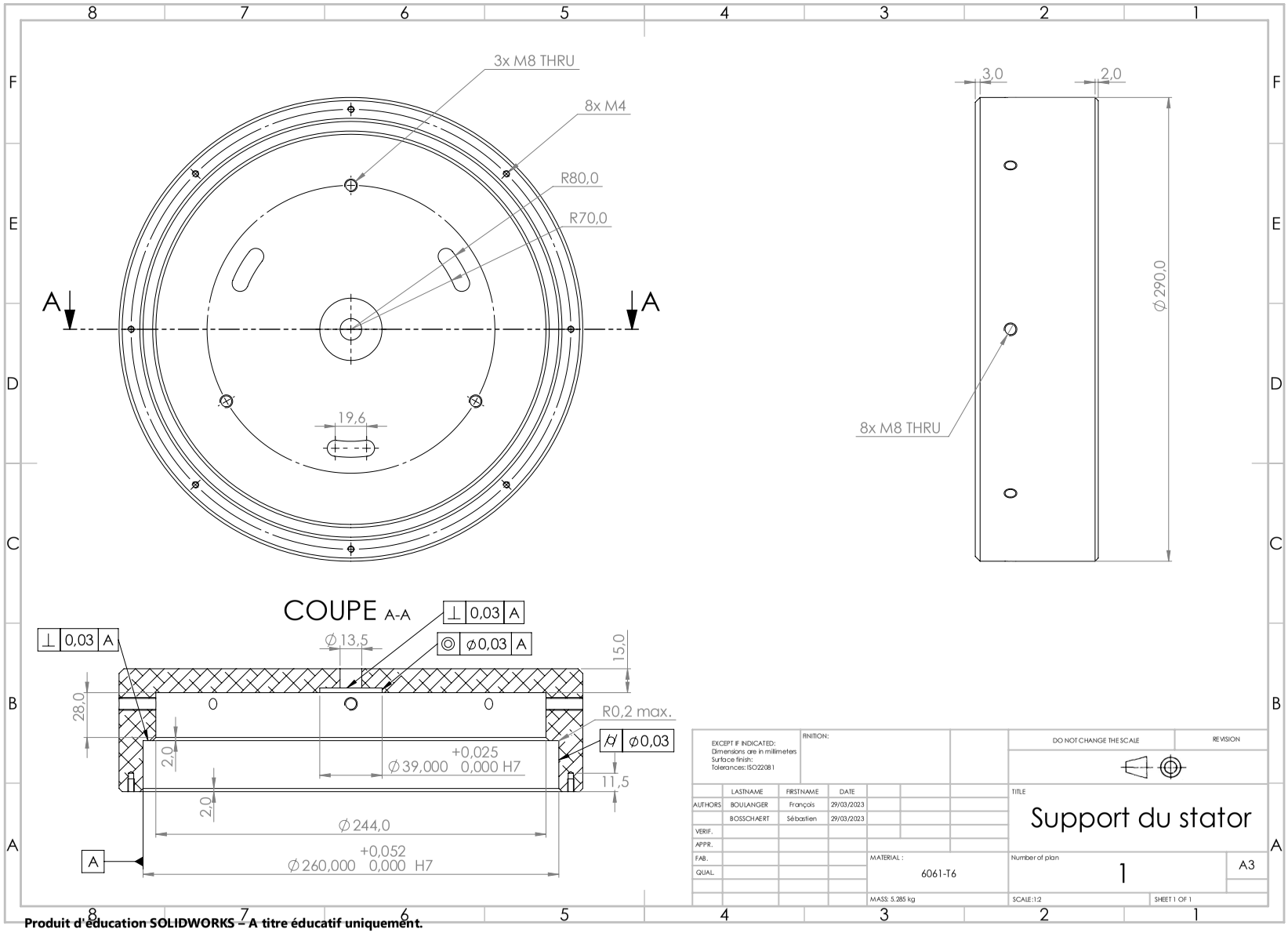

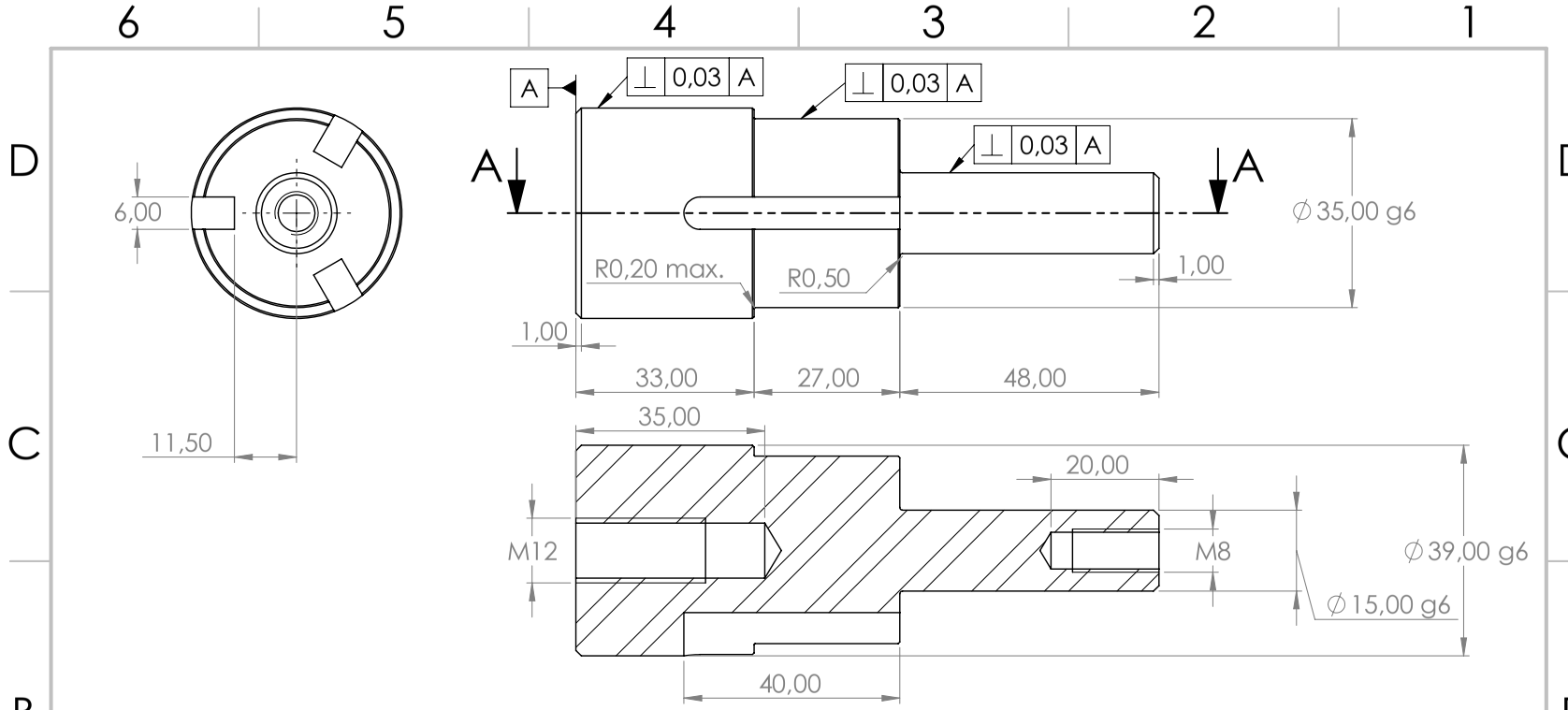

COUPE A-A

EXCEPT IF INDICATED : Dimensions are in millimeters Surface finish : Chamfers are 0.1 Tolerances: ISO22081		FINITION:				NE PAS CHANGER L'ECHELLE	REVISION
	NOM	PRENOM	DATE			TITRE:	
AUTEUR	BOULANGER	François	30/03/23			Arbre	
	BOSSCHAERT	Sébastien	30/03/23				
VERIF.							
APPR.							
FAB.				MATERIAU: AISI Acier inoxydable type 316L		No. DE PLAN 1	A4
QUAL.							
				MASSE: 525.46g		ECHELLE:1:1	FEUILLE 1 SUR 1

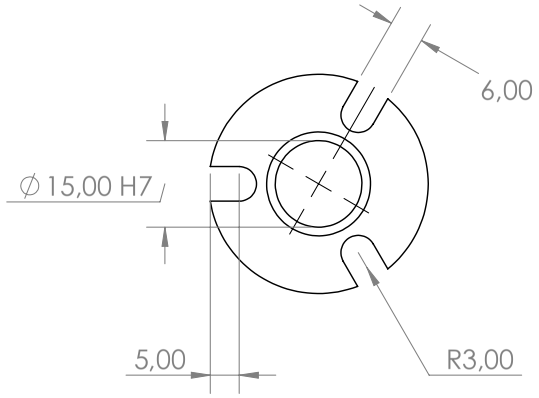

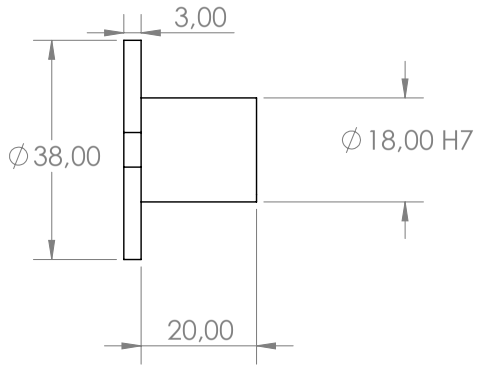

EXCEPT IF INDICATED : Dimensions are in millimeters Surface finish : Tolerances: ISO22081	FINITION:					NE PAS CHANGER L'ECHELLE	REVISION
	NOM	PRENOM	DATE			TITRE:	
AUTEUR	BOULANGER	François	30/03/23			Entretoise sous moteur	
	BOSSCHAERT	Sébastien	30/03/23				
VERIF.							
APPR.							
FAB.				MATERIAU:		No. DE PLAN	A4
QUAL.				6061-T6		3	
				MASSE: 10.86g		ECHELLE:1:1	FEUILLE 1 SUR 1

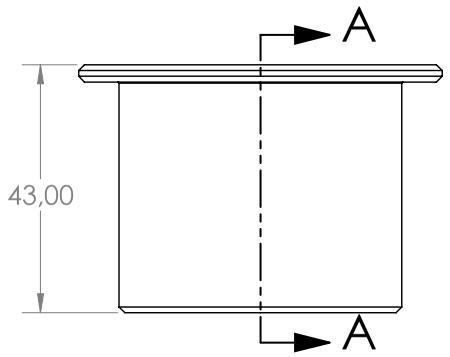

COUPE A-A

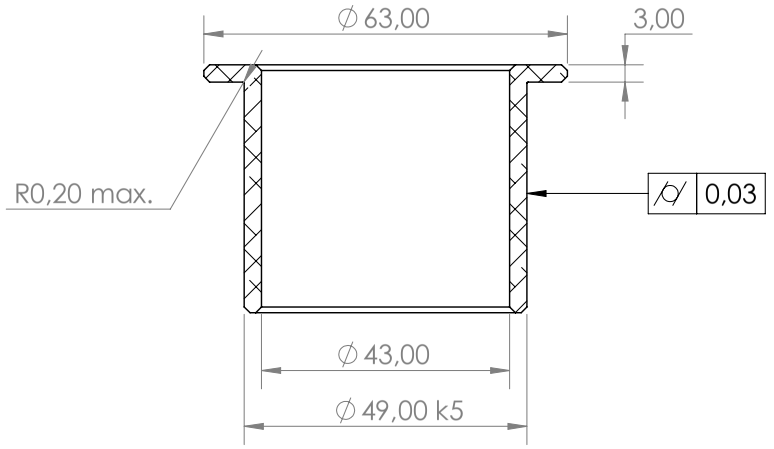

EXCEPT IF INDICATED : Dimensions are in millimeters Surface finish : Chamfers are 1 Tolerances: ISO22081		FINITION:				NE PAS CHANGER L'ECHELLE / REVISION
	NOM	PRENOM	DATE			TITRE: Cage d'écureuil
AUTEUR	BOULANGER	François	30/03/23			
AUTEUR	BOSSCHAERT	Sébastien	30/03/23			
VERIF.						
APPR.						
FAB.				MATERIAU: 6061-T6		No. DE PLAN 2 / A4
QUAL.						
				MASSE: 59.21g		ECHELLE:1:1 / FEUILLE 1 SUR 1

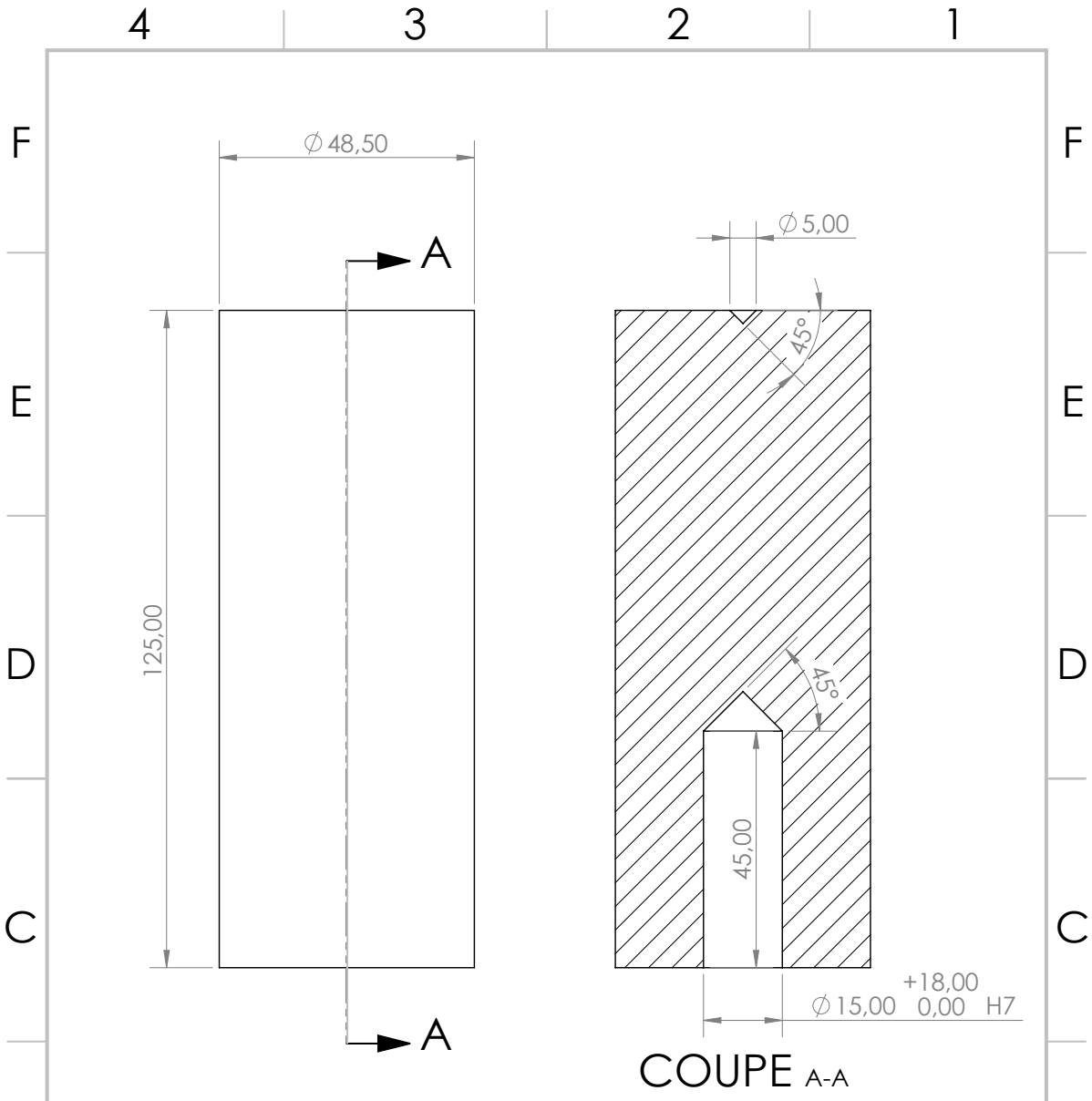

SAUF INDICATION CONTRAIRE: LES COTES SONT EN MILLIMETRES ETAT DE SURFACE: TOLERANCES: ISO22081		FINITION:			CASSER LES ANGLES VIFS		NE PAS CHANGER L'ECHELLE	REVISION
	NOM	PRENOM	DATE				TITRE:	
AUTEUR	BOSSCHAERT	SEBASTIEN	10/05/23				Pose_rotor	
VERIF.								
APPR.								
FAB.								
QUAL.				MATERIAU: Acier			No. DE PLAN 1	A4
				MASSE:			ECHELLE:1:1	FEUILLE 1 SUR 1

UNIVERSITÉ CATHOLIQUE DE LOUVAIN
École polytechnique de Louvain
Rue Archimède, 1 bte L6.11.01, 1348 Louvain-la-Neuve, Belgique | **www.uclouvain.be/epl**